NASA/TM–2012-104606 / Vol 28

Technical Report Series on Global Modeling and Data Assimilation, Volume 28

Max J. Suarez, Editor

The GEOS-5 Atmospheric General Circulation Model: Mean Climate and Development from MERRA to Fortuna

Andrea Molod, Lawrence Takacs, Max Suarez, Julio Bacmeister, In-Sun Song, and Andrew Eichmann

National Aeronautics and
Space Administration

Goddard Space Flight Center
Greenbelt, Maryland 20771

April 2012

NASA STI Program ... in Profile

Since its founding, NASA has been dedicated to the advancement of aeronautics and space science. The NASA scientific and technical information (STI) program plays a key part in helping NASA maintain this important role.

The NASA STI program operates under the auspices of the Agency Chief Information Officer. It collects, organizes, provides for archiving, and disseminates NASA's STI. The NASA STI program provides access to the NASA Aeronautics and Space Database and its public interface, the NASA Technical Report Server, thus providing one of the largest collections of aeronautical and space science STI in the world. Results are published in both non-NASA channels and by NASA in the NASA STI Report Series, which includes the following report types:

- TECHNICAL PUBLICATION. Reports of completed research or a major significant phase of research that present the results of NASA Programs and include extensive data or theoretical analysis. Includes compilations of significant scientific and technical data and information deemed to be of continuing reference value. NASA counterpart of peer-reviewed formal professional papers but has less stringent limitations on manuscript length and extent of graphic presentations.
- TECHNICAL MEMORANDUM. Scientific and technical findings that are preliminary or of specialized interest, e.g., quick release reports, working papers, and bibliographies that contain minimal annotation. Does not contain extensive analysis.
- CONTRACTOR REPORT. Scientific and technical findings by NASA-sponsored contractors and grantees.
- CONFERENCE PUBLICATION. Collected papers from scientific and technical conferences, symposia, seminars, or other meetings sponsored or co-sponsored by NASA.
- SPECIAL PUBLICATION. Scientific, technical, or historical information from NASA programs, projects, and missions, often concerned with subjects having substantial public interest.
- TECHNICAL TRANSLATION. English-language translations of foreign scientific and technical material pertinent to NASA's mission.

Specialized services also include organizing and publishing research results, distributing specialized research announcements and feeds, providing help desk and personal search support, and enabling data exchange services. For more information about the NASA STI program, see the following:

- Access the NASA STI program home page at http://www.sti.nasa.gov
- E-mail your question via the Internet to help@sti.nasa.gov
- Fax your question to the NASA STI Help Desk at 443-757-5803
- Phone the NASA STI Help Desk at 443-757-5802
- Write to:

  NASA STI Help Desk
  NASA Center for AeroSpace Information
  7115 Standard Drive
  Hanover, MD 21076-1320

NASA/TM–2012-104606 / Vol 28

Technical Report Series on Global Modeling and Data Assimilation, Volume 27

Max J. Suarez, Editor

The GEOS-5 Atmospheric General Circulation Model: Mean Climate and Development from MERRA to Fortuna

Andrea Molod
University of Maryland College Park, College Park, MD

Lawrence Takacs
Science Systems and Applications, Inc., Lanham, MD

Max Suarez
NASA Goddard Space Flight Center, Greenbelt, MD

Julio Bacmeister
National Center for Atmospheric Research, Boulder, CO

In-Sun Song
Next Generation Model Development Center, Seoul, South Korea

Andrew Eichmann
Science Systems and Applications, Inc., Lanham, MD

National Aeronautics and
Space Administration

Goddard Space Flight Center
Greenbelt, Maryland 20771

April 2012

Level of Review: This material has been technically reviewed by technical management

Available from:
NASA Center for AeroSpace Information
7115 Standard Drive
Hanover, MD 21076-1320

National Technical Information Service
5285 Port Royal Road
Springfield, VA 22161 Price Code: A17

Abstract

This report is a documentation of the Fortuna version of the GEOS-5 Atmospheric General Circulation Model (AGCM). The GEOS-5 AGCM is currently in use in the NASA Goddard Modeling and Assimilation Office (GMAO) for simulations at a wide range of resolutions, in atmosphere only, coupled ocean-atmosphere, and data assimilation modes. The focus here is on the development subsequent to the version that was used as part of NASA's Modern-Era Retrospective Analysis for Research and Applications (MERRA). We present here the results of a series of 30-year atmosphere-only simulations at different resolutions, with focus on the behavior of the 1° resolution simulation. The details of the changes in parameterizations subsequent to the MERRA model version are outlined, and results of a series of 30-year atmosphere-only climate simulations at 2° resolution are shown to demonstrate changes in simulated climate associated with specific changes in parameterizations. The GEOS-5 AGCM presented here is the model used for the GMAO's atmosphere-only and coupled CMIP-5 simulations.

The seasonal mean climate of the 1° simulation is evaluated against multi-year climatologies computed from available satellite-based and reanalysis fields. The seasonal mean climate of the Fortuna version of the GEOS-5 AGCM represents a substantial improvement over the simulated climate of the MERRA version. The Fortuna simulation generally agrees well with the observational estimates. The improvements in simulated climate are primarily associated with the increased re-evaporation of frozen precipitation and cloud ice, resulting in a wetter atmosphere. The largest differences between the Fortuna GEOS-5 AGCM and observations are in the cloud cover and cloud effects, and indicate a GEOS-5 AGCM climate with excessive cloud cover in the extratropics and tropical clouds which are too low in altitude. Other biases include a cold tropical tropopause, and an eastward shift in the boreal summer tropical circulation pattern, both of which exist in many other AGCM simulations. Recommendations are included to address these remaining errors in mean simulated climate, which involve improvements in the parameterization of clouds and convection.

Contents

List of Tables

List of Figures

1 Introduction

The Fortuna version of the GEOS-5 AGCM represents the new generation AGCM developed by the Global Modeling and Assimilation Office (GMAO) to replace the model version that was used as part of MERRA (Modern-Era Retrospective Analysis for Research and Applications, Rienecker, et al., 2011). The focus of the development of the MERRA version of the GEOS-5 AGCM was on the behavior of the components of the hydrological cycle in MERRA itself. The focus of the development of the Fortuna version was on the behavior in atmosphere-only and in coupled atmosphere ocean simulations. Results of atmosphere-only and coupled climate simulations with the new version exhibit major improvements over the MERRA version. Towards this end, adjustments were made to several of the parameterizations of physical processes, with the most important impact from the changes to the moist processes and to the turbulence parameterization. The major adjustments to the moist processes included the increase of the re-evaporation of grid scale precipitation, the reformulation of the critical relative humidity criterion for phase changes of in-cloud and precipitating liquid and ice, and the implemention of a resolution-dependant stochastic trigger for cumulus convection. The adjustments to the turbulence parameterization included changes in the behavior of the scheme in the presence of large wind shear.

The major features of atmosphere-only climate simulations as compared to available observationally based estimates are presented here. A single Atmospheric Model Intercomparison Project (AMIP)-style 30-year simulation at 1°x1.25°x72 levels is used here to describe the mean climate of the Fortuna version of the GEOS-5 AGCM. In addition, results from a series of AMIP-style sensitivity experiments (at 2°x2.5°x72 levels) exploring the changes in parameterizations between the MERRA and Fortuna models are presented to demonstrate the importance of the various changes. Although the development focused on AMIP-style and coupled climate runs, the resulting model has also performed well in data assimilation and numerical weather prediction applications. As a result, this version of the GEOS-5 AGCM is used in the GMAO's real-time atmospheric analysis and forecast system, unifying the climate and weather models.

2 Model Description - Transition from MERRA to Fortuna

The generation of the GEOS-5 Atmospheric General Circulation Model (GCM) that was used as part of NASA's Modern-Era Retrospective Analysis for Research and Applications (MERRA) is described in Rienecker, et al. (2008). A brief summary of the model's physical parameterizations is provided here along with a more detailed description of the differences between the MERRA generation model and the current Fortuna generation. The GEOS-5 AGCM physics includes parameterization schemes for atmospheric convection, large scale precipitation and cloud cover, longwave and shortwave radiation, turbulence, gravity wave drag, and a land surface model.

Convection is parameterized using the Relaxed Arakawa-Schubert scheme (Moorthi and Suarez, 1992) and includes a scheme for the generation and re-evaporation of falling rain (Bacmeister et al., 2006). RAS is a mass flux scheme with an updraft only detraining plume cloud model and a quasi-equilibrium closure. The prognostic cloud cover and cloud water and ice scheme is from Bacmeister et al. (2006). The scheme includes large scale condensation, evaporation, autoconversion and accretion of cloud water and ice, sedimentation of cloud ice and re-evaporation of falling precipitation. The longwave radiative processes are described by Chou and Suarez (1994), and include absorption due to cloud water, water vapor, carbon dioxide, ozone, N_2O and methane. The shortwave is from Chou (1990) and Chou (1992), and includes absorption by water vapor, ozone, carbon dioxide, oxygen, cloud water, and aerosols and includes scattering by clouds water and aerosols. The turbulence parameterization is based on the Lock (2000) scheme, acting together with the Richardson-number based scheme of Louis and Geleyn (1982). The Lock scheme includes a representation of non-local mixing (driven by both surface fluxes and cloud-top processes) in unstable layers, either coupled to or decoupled from the surface, and an explicit entrainment parameterization. The original scheme was extended in GEOS-5 to include moist heating and entrainment in the unstable surface parcel calculations. The Monin-Obukhov surface layer parameterization is described in Helfand and Schubert (1995), and includes the effects of a viscous sublayer for heat and moisture transport over all surfaces except land. The ocean roughness is determined by a blend of the algorithms of Large and Pond (1981) and Kondo (1975), modified in the mid-range wind regime according to Garfinkel et al. (2011) and in the high wind regime according to Molod et al. (2012). The gravity wave parameterization computes the momentum and heat deposition into the grid-scale flow due to orographic (McFarlane, 1987) and nonorographic (after Garcia and Boville, 1994) gravity wave breaking. The Land Surface Model from Koster et. al (2000) is a catchment-based scheme which treats subgrid scale heterogeneity in surface moisture

statistically. The applied subgrid scale distributions are related to the topography, allowing it to exert a major control over much of the subgrid variability. The catchment model is coupled to the multi-layer snow model of Stieglitz et al. (2001).

The collection of parameterizations in the Fortuna and MERRA AGCMs are identical with the exception of the parameterization of the surface layer. The Fortuna AGCM employs the scheme of Helfand and Schubert (1995), while the MERRA AGCM employed the scheme of Louis (1979). The changes from the MERRA AGCM to Fortuna that are relevant to the results presented here are largely in the details of the moist scheme, including the cloud-radiative interactions, the turbulence scheme, and the gravity wave drag scheme. A comprehensive list of the changes for each scheme is presented below, listed for each scheme in order of the impact on the simulations.

2.1 Moist Processes

The parameterizations for moist processes did not undergo a fundamental change in any of the algorithms they contain between the MERRA AGCM and Fortuna versions of GEOS-5. Rather, the changes were related to the parameters which control the relative strengths of the various sub-processes, and to aspects of the scheme which are specified *a priori*.

- Increase of re-evaporation of convective and grid-scale frozen precipitation
- Reformulate critical relative humidity for grid scale condensation/sublimation
- Rework of pressure and temperature dependant autoconversion and effective radius of cloud drops
- Change in the adjustment of cloud fractions for radiation effects, reducing fractions
- Implement autoconverision of all warm fog
- Include stochastic RAS trigger, more restrictive as horizontal resolution increases
- Cloud base for convection set at PBL depth
- RAS time scale dependence on turbulent eddy diffusion coefficients removed

The Fortuna scheme for the re-evaporation of precipitation and suspended cloud water and ice contains a series of new parameter settings which result in a substantial increase over the MERRA model in the re-evaporation of snow and ice. The main impact came from allowing the snow re-evaporation process to proceed all the way to the critical relative humidity used by the large scale condensation algorithm, and from reducing the assumed mean diameter of snow particles, thereby increasing the residence time in any grid box and therefore the re-evaporation rate. The impact of the changes in parameter settings on the water vapor source due to re-evaporation for the December-January-February average is shown in figure 1. The largest increase in the Fortuna AGCM is aloft, near 500 mb, where the increase is up to 0.7 g kg^{-1} day^{-1}. The impact on the model's humidity is described in section 4.

The algorithm for large scale condensation, as described in Bacmeister et al. (2006), assumes that the probability distribution function (PDF) of total water is "top-hat" shaped. The width of the PDF is associated with the grid box "critical relative humidity" (RHcrit) at which condensation takes place. The vertical profile as well as the magnitude of RHcrit was changed between the MERRA and Fortuna AGCMs, and now includes an AIRS-based profile and a dependence on model horizontal resolution after Molod (2012). Typical RHcrit profiles from the MERRA and Fortuna AGCM are shown in figure 2, and indicate generally lower values in the Fortuna formulation except in the boundary layer, where turbulent mixing is sufficient to homogenize the total water distribution.

The changes related to autoconversion, effective radius and cloud fractions seen by radiation were designed to improve the cloud forcing. In general, the changes increased autoconversion and particle effective radii for low-level, warm clouds, thereby reducing the radiative impact, and had the reverse effect on low-level cold clouds. The implementation of the stochastic RAS trigger is resolution dependant, and has its main impact on limiting deep convection at higher resolution (half degree or higher). The remaining changes had a smaller impact on the Fortuna climate simulations.

2.2 Turbulence

The fundamental change that took place in the evolution from the MERRA to the Fortuna AGCM turbulence parameterization is in the balance between the turbulent diffusion from the local and non-local schemes. The change was designed in part to improve the simulated diffusion just above

the surface layer, and to incorporate the effects of wind shear on atmospheric turbulence.

- Remove restrictions on maximum allowed eddy diffusion coefficients from Louis scheme
- Reformulate turbulent length scale in Louis scheme (make it smaller in general)
- Reduce effect of Lock scheme in the presence of wind shear
- Scale back cloud top entrainment at top of shallow Lock plumes
- Increase turbulence due to small scale variations in topography

The first two items took place in tandem, and together constitute an enhanced diffusion from the Richardson-number based Louis scheme. The estimate of the turbulent length scale for the Louis scheme was reformulated in the Fortuna AGCM, still based on Blackadar (1962) but now written as a function of the boundary layer height as estimated from the combined Lock and Louis schemes. In addition, the Lock scheme "surface plumes" are more inhibited in the presence of strong wind shear in the current Fortuna version than in the MERRA version. The scaled back cloud top entrainment and the increase of orographic drag had little impact on the mean climate and were implemented based on improved atmosphere-ocean coupled simulations, and on improved short term forecasts, respectively.

2.3 Surface Layer

The parameterization of the surface layer in the Fortuna AGCM uses Monin-Obhukov (MO) similarity theory and is based on the surface layer scheme of Helfand and Schubert (1995). The scheme was implemented to replace the paramerization of Louis (1979), to maintain a closer consistency between the local stability and the surface layer fluxes.

- Replace Louis surface layer with Helfand and Schubert Monin-Obukhov formulation
- Remove viscous sublayer over land surfaces
- Change equation that relates ocean roughness to surface stress for middle and high wind regimes

The implementation of the MO scheme included the use of the MO stability functions, the replacement of the algorithm for the viscous sublayer (the laminar layer that can act to impede the flux of heat and moisture), and the replacement of the functional relationship between ocean surface wind and wind stress. The effect of the laminar sublayer in the MO scheme is implemented by augmenting the non-dimensional gradients of moisture and humidity rather than by modifying the heat and moisture roughness lengths. In addition, the stable surface layer stability function in the Helfand scheme differs from the functional dependance of fluxes on Richardson number in the Louis scheme, and results in an increased turbulent heat exchange (of both signs) under stable conditions. Figure 3 shows a scatter diagram of the sensible heat flux as a function of surface bulk Richardson number under conditions where the monthly mean air temperature exceeds the monthly mean skin temperature. The black points are from a simulation with the Helfand surface layer, and the red are from a simulation using the Louis scheme. The larger values of sensible heat flux in the Helfand simulation are apparent, and even more apparent when the monthly mean sensible heat flux is downward.

The laminar sublayer in the new scheme was removed over land surfaces, due in part to the ambiguity of defining a viscous sublayer between the vegetation canopy and the atmospheric surface layer, and due also to the inclusion of some of the viscous sublayer effects as part of the land surface model.

The functional relationship between the wind stress and the ocean surface roughness for medium surface wind speeds from the MERRA AGCM (green) and the Fortuna AGCM (black) is shown in figure 4a, where the increase based on Garfinkel et al. (2011) is apparent. The decrease of roughness at strong tropical cyclone strength winds from the MERRA AGCM (green) to the Fortuna AGCM (black) is shown in figure 4b, based on Molod et al. (2012).

2.4 Gravity Wave Drag

- Changed profile of background drag (increased in tropics)
- Added intermittency of drag

The latitudinal profile of background nonorographic drag in Fortuna was modified to include a source related to tropical precipitation in addition to the local maxima related to storm track

precipitation. The use of this structure is justified based on the physical argument that major sources for nonorographic gravity waves (e.g., convective and frontal systems, see Richter et al. 2010) often accompany precipitation. The background nonorographic drag profile is shown in figure 5, where the MERRA AGCM tropical profile is shown with the dashed line, and the Fortuna AGCM profile is shown with the solid line.

The intermittency factor used in the standard Lindzen-type method is a factor used to reduce the strength of the gravity wave drag computed from linear theory. In the MERRA AGCM the factor is 0.125 for both orographically and nonorographically excited gravity waves. It is increased for orographic waves gradually as a function of latitude in the Fortuna AGCM, reaching a value of 0.3125 south of approximately 40°S. This behavior is based on observational evidence of strong gravity waves from isolated small mountains in the Antarctic peninsula (Alexander and Teitelbaum 2007) and the South Georgia islands (Alexander et al. 2009).

2.5 Land Surface Model

A small set of parameter changes in the land surface model was implemented, designed to compensate for an error in the simulated climate in both the MERRA and Fortuna versions of the GEOS-5 AGCM.

- Reduced fraction of grid box wetted by rainfall, and capacity of interception reservoir

The change in parameters was implemented to prevent the immediate evaporation of almost all the incident rainfall, particularly from the canopy interception reservoir. By reducing both the capacity of the interception reservoir and the fraction of surface precipitation incident on it, the precipitation is used to wet the soil. The results of this change are described in detail in section 4.

3 Climate Simulation Results

3.1 Experiment Configuration

The 30 year GEOS-5 AGCM simulation to be used as a basis of comparison with observations was initialized with January 10, 1979 conditions. The horizontal grid is a lat-lon grid with global resolution of 1° x 1.25°. The vertical grid is an eta coordinate grid with 72 levels, spaced to increase the resolution near the surface and near the tropopause. The simulation was forced with observed sea surface temperatures (Reynolds, 2002).

3.2 Mean Circulation

The seasonal variation of GEOS-5 AGCM mean state is presented and compared to the MERRA reanalysis. The comparisons will generally entail examination of December-January-February (DJF) and June-July-August (JJA) means from reanalysis and from GEOS-5 AGCM simulations. The examination of the mean seasonal state includes the zonal mean and seasonal mean zonal and meridional wind fields, mass streamfunction, temperature and relative humidity. The velocity potential at 200 hPa is shown as in indicator of the divergence aloft associated with diabatic heating, and the eddy height at 300 hPa is shown to assess the stationary wave pattern. Additional comparisons are made to the European Center Interim (EC-I) reanalysis (Dee et al., 2011) for quantities that show relatively lower correlations between MERRA and EC-I reanalyses (Rienecker et al., 2011), presumably due to the greater influence of the underlying AGCM. The meridional wind field, particularly in the tropics, and the humidity field show much lower MERRA to EC-I correlations than the zonal wind or temperature, and so the comparison of AGCM and MERRA meridional wind and humidity fields will also be augmented with comparisons against EC-I reanalysis.

3.2.1 Zonal Wind and Temperature

The zonal mean zonal wind fields for each season are shown in figures 6 and 7. In each figure, the top panel shows the model result, the middle panel shows the MERRA validation, and the bottom panel shows the difference. The MERRA zonal wind field is well constrained by observations (Rienecker et al. 2008), and differences between GEOS-5 AGCM and MERRA fields are attributed

mainly to GEOS-5 AGCM errors. The pattern of the GEOS-5 AGCM fields matches well with MERRA fields in all seasons in the troposphere. The subtropical jet is stronger in GEOS-5 AGCM by up to 4 m sec^{-1} in the winter hemisphere in both seasons, and weaker by up to 4 m sec^{-1} in the summer hemisphere with a slight poleward displacement. The surface winds are also generally weaker in GEOS-5 AGCM by up to 2 m sec^{-1} in both JJA and DJF with the exception of the southern hemisphere polar region in DJF, where the winds are stronger in the AGCM by up to 2 m sec^{-1}. The consequences of the strong surface winds on the surface fluxes and wind stress will be discussed in section 3.5. The stratospheric jets are weaker in the GEOS-5 AGCM simulation than in MERRA in the winter hemisphere by up to 4 m sec^{-1} in both DJF and JJA.

The zonal mean temperature fields for DJF and JJA are shown in figures 8 and 9. In general the temperatures in the troposphere are within 1K of MERRA temperatures, as seen in figures 8c and 9c. The exceptions include up to a 3K warm bias in the AGCM in the northern hemisphere extratropical continents in JJA (geographical distribution not shown). GEOS-5 AGCM tropopause temperatures are also colder than MERRA in both seasons by up to 2K in the tropics and 5K in the southern hemisphere high latitudes in DJF. The cold tropical tropopause is typical of many AGCMs (Solomon, et al., 2007), and is consistent with strong subtropical jets based on the thermal wind relationship. The GEOS-5 temperatures are warmer than MERRA in the high latitude stratosphere in wintertime by up to 7K in JJA, which is consistent with the weak stratospheric jets discussed above.

3.2.2 Meridional Wind and Mass Streamfunction

Figures 10 and 11 show the comparisons among the meridional wind fields from the GEOS-5 AGCM and each of the two reanalyses. There is good general agreement between GEOS-5 AGCM and either reanalysis estimate, in terms of magnitude and location of wind maxima in both seasons. In DJF the poleward v-wind in the extratropics is weaker in the GEOS-5 AGCM by up to 0.5 m sec^{-1} as compared to either reanalysis, as shown in figures 10d and 10e. The model-reanalysis difference in the diverging v-wind aloft in the tropics is comparable in magnitude to the difference between the MERRA and EC-I reanalysis shown in figure 10f. This makes the characterization of model error there difficult, but the comparison with EC-I (figure 10e) suggests that the region of diverging v-wind extends further down in the atmosphere in EC-I than in the GEOS-5 AGCM simulation. In JJA in general the GEOS-5 AGCM v-wind pattern aloft (11a) shows a closer resemblance to the

pattern seen in MERRA (11b) than to the pattern seen in EC-I (11c) . As compared to the EC-I estimate, the GEOS-5 AGCM v-wind aloft is stronger by up to 1.2 m sec^{-1}, and does not extend as far down into the atmosphere. The Hadley cell strength is revealed by the mass streamfunction, shown in figure 12. The general agreement between GEOS-5 AGCM and both reanalyses in DJF, along with the stronger GEOS-5 AGCM mass streamfunction in JJA relative to EC-I, is consistent with the discussion of the meridional wind.

3.2.3 Surface Wind Speed

The surface wind speed in the GEOS-5 AGCM is influenced by the winds aloft and by the description of the wind stress at the land or ocean surface. Comparisons between the GEOS-5 AGCM simulated surface wind speed over the oceans and the satellite estimates from Goddard Satellite-based Surface Turbulent Fluxes (GSSTF) are shown in figures 13 and 14. In general, the surface winds are underestimated in the GEOS-5 AGCM in tropical and subtropical regions, and overestimated at higher latitudes. The comparison with GSSTF is consistent with the evaluation against MERRA described in section 3.2.1 over mostly ocean covered regions. The overestimate of surface winds in the northern hemisphere extratropical oceans was not apparant in the zonal means shown above.

3.2.4 Eddy Height

The northern hemisphere wintertime stationary wave pattern of GEOS-5 AGCM is evaluated with the DJF eddy geopotential height field at 300 hPa, shown in comparison to the MERRA field in figure 15. The dominant feature is the Pacific-North-America (PNA) pattern. The location and magnitude of the Pacific trough and ridge are well captured by GEOS-5 AGCM, although the intensity of both trough and ridge are weaker than the MERRA eddy heights by up to 50 m.

3.2.5 Velocity Potential

The 200 hPa velocity potential (χ) field is shown in figures 16 and 17. The gradients of χ represent the divergent part of the flow and reflect the response to diabatic heating aloft due primarily to convection and radiative cloud forcing. The DJF velocity potential pattern in MERRA (figure 16b) is dominated by the outflow associated with the Australian monsoon, and is well captured

by GEOS-5 AGCM. The AGCM χ field (figure 16a), however, has a second region of outflow over South America which is not present in the MERRA (or in the EC-I reanalysis field, not shown). The JJA velocity potential pattern (figure 17) in both the GEOS-5 AGCM and MERRA is dominated by the outflow associated with the Asian monsoon and the Pacific warm pool. The GEOS-5 AGCM χ field, however, is shifted approximately 10° of longitude to the east, and represents an error in the tropical climate during JJA that is present in other AGCMs (eg., Neale et al, 2010). This eastward shift is also shown in sections 3.3.2 and 3.4 to be manifest in many other aspects of the AGCM simulated climate.

3.2.6 Humidity

The specific and relative humidity (RH) fields from GEOS-5 AGCM, MERRA and EC-I are shown in figures 18, 19, 20 and 21. The differences in specific humidity between the two reanalyses (figures 18f and 19f), particularly in the tropics near the surface, are comparable in magnitude to the differences between the AGCM and either reanalysis, which makes an assessment of the model error in that region difficult. The general trend is for high GEOS-5 AGCM specific humidities as compared to either reanalysis throughout most of the atmosphere in both JJA and DJF. The humidities are higher in GEOS-5 AGCM by up to 1 g kg^{-1} in the tropics near 500 mb, and in the extratropics in both hemispheres near 850 mb. The tropical near surface humidity in the GEOS-5 AGCM is slightly wet as compared to MERRA (figures 18d and 19d) and dry as compared to EC-I (figures 18e and 19e). The relative humidity differences between the reanalyses and the AGCM are, in general, consistent with specific humidity differences, and so are governed primarily by water content rather than by temperature. The RH is low as compared to either reanalysis near the tropical tropopause (figures 20d,e and 21d,e). This dry bias exists despite a cold bias in the tropopause temperatures (shown in section 3.2.1), implying an upper tropospheric humidity that is dry.

3.3 Moisture Budget

The vertically integrated atmospheric moisture budget is given by:

$$\frac{\partial W}{\partial t} = -\frac{1}{g}\int_{p=bot}^{p=top} \nabla \cdot \pi \mathbf{V} q d\sigma + E - P \tag{1}$$

where W is the total precipitable water, π is the surface pressure, q is the specific humidity, E is the evaporation and P is the precipitation. The first term on the right hand side represents the divergence of the moisture transport, E is the source term, and P is the sink term.

In the simulation the long term (monthly or seasonal time scales or longer) vertically integrated moisture convergence almost balances the sources and sinks, and the small residual gives rise to the seasonal cycle. A careful examination, then, of the sources and sinks individually and together, along with the mean W, provides a summary of the climate of the atmospheric hydrological cycle.

3.3.1 Evaporation

The evaporation over the oceans is assumed to depend chiefly on the surface wind magnitude, the air-sea moisture and temperature gradients and the surface roughness. Larger gradients will enhance the evaporation, as will stronger surface winds (up to a point) or enhanced roughness. Because of the similarity in technique used to estimate evaporation by the AGCM and the GSSTF algorithm (see Appendix A), any differences between the AGCM and the GSSTF verification are primarily due to differences in estimates of the near surface gradients of humidity or winds and surface roughness. The oceanic zonal mean (figure 22) evaporation in the AGCM and GSSTF observational data has a maximum over the subtropical oceans, where precipitation is low and the air above the surface is relatively dry due to atmospheric subsidence. There is a local minimum in evaporation at the equator, due to weaker local winds and cooler sea surface temperatures associated with the regions of oceanic upwelling. The winter hemispheres have a higher evaporation rate associated with higher surface winds in winter. The AGCM simulated evaporation corresponds well to the latitudinal and seasonal changes seen in the GSSTF data, but overestimates the magnitude by up to 20 W m^{-2}, in the subtropics, corresponding to approximately 0.75 mm day^{-1}. The GSSTF estimates at high latitudes are limited by the sampling and quality of the satellite retreivals at those latitudes.

The spatial pattern of GEOS-5 AGCM and GSSTF evaporation fields are shown in figures 23 and 24. In general GEOS-5 AGCM evaporation values are higher than the GSSTF estimates by up

to 40 W m^{-2} in the tropics, and lower than GSSTF by up to 30 W m^{-2} at higher latitudes. The underestimate of the evaporation is larger in the winter hemisphere in both DJF and JJA, as indicated by the larger difference in the northern hemisphere in figure 23c and in the southern hemisphere in figure 24c. These errors in the AGCM evaporation are not consistent with the errors in the surface winds (shown in section 3.2.3 to be underestimated in the tropics and overestimated elsewhere), but are consistent with the errors in the near surface humidity (shown in section 3.2.6 to be dry in the tropics near the surface and wet elsewhere) and so in the near surface humidity gradient.

3.3.2 Precipitation

Precipitation is a sink term for atmospheric moisture, and the ability to simulate it has far reaching implications for atmospheric temperature and humidity profiles as well as cloud-radiative interactions. Precipitation is highly variable, both in nature and in a GCM, and is also difficult to measure accurately, particularly over oceans. General comparisons between the AGCM and observations of large scale features, trends and seasonal variations provide a reasonable sense of the ability to simulate convection and atmospheric supersaturation-related rainfall. The observational precipitation chosen for this comparison is from the GPCP estimates of Huffman, mainly because the extensive raw data coverage over land (appendix A) and the blending of several different types of data over oceans.

Zonal mean plots of GEOS-5 AGCM and GPCP precipitation from DJF and JJA are presented in figure 25. All show a maximum in the Intertropical Convergence Zone (ITCZ) and the seasonal shift from a split ITCZ straddling the equator in DJF to a stronger ITCZ in the northern hemisphere in JJA. The tropical values correspond well, except for a stronger ITCZ in the GEOS-5 AGCM simulation north of the equator in DJF. GEOS-5 AGCM and GPCP also all show a minimum of precipitation over the subtropics, where atmospheric subsidence suppresses convection. The magnitudes of GEOS-5 AGCM and GPCP observations correspond relatively well here, although here the GEOS-5 AGCM overestimates the precipitation in JJA by approximately 1.5 mm day^{-1}. GEOS-5 AGCM and GPCP also show a secondary smaller maximum over the extratropics, where the excursions of the polar front initiate precipitation. GEOS-5 AGCM zonal mean precipitation in the extratropics matches the GPCP estimate in both JJA and DJF, with the exception of a poleward shift of the frontal precipitation in the northern hemisphere in JJA.

The lat-lon maps of precipitation, figures 26 and 27, show some pattern differences between the AGCM and GPCP even at latitudes where the zonal means agree. In DJF the difference pattern (figure 26c) shows that the GEOS-5 AGCM precipitation is excessive over the Andes, exhibits a northward shift of the ITCZ precipitation over the western Pacific and Indian ocean regions, and is excessive over southern Africa. In JJA in the tropics, where the zonal means showed good agreement, the AGCM pattern exhibits a shift to the east in longitude of about 10°. This shift was seen in the velocity potential pattern shown in section 3.2.5. The GEOS-5 AGCM overestimate the precipitation over high terrain is manifest over the Tibetan plateau in JJA.

3.3.3 Net Sources and Sinks

Evaporation minus Precipitation (E-P) is the atmospheric measure of the total net source of moisture from the continents and oceans. The verification data for E-P is available over oceans from the COADS data set. There are some discrepancies between the COADS precipitation estimates and the GPCP fields used for comparison above, and between the evaporation estimates and the latent heat flux from GSSTF, but the differences are chiefly in magnitude and not in pattern. Discrepancies between COADS and GSSTF estimates of evaporation are largely in high latitude regions. The oceanic zonal-mean plots of E-P from GEOS-5 AGCM and COADS, figure 28, both show positive maxima over the subtropical oceans, especially in the winter hemisphere, reflecting the role of evaporation over the subtropical oceans as the major global source of atmospheric water vapor. The negative minima in the GEOS-5 AGCM and COADS over the equator and in the extratropics reflect the major sink regions of the ITCZ and frontal storm tracks, respectively, where precipitation is highest. Differences between zonal mean GEOS-5 AGCM and COADS E-P are largely found over high latitude regions, where the discrepancies between COADS and GSSTF estimates of evaporation make assessment of model errors difficult.

3.3.4 Equilibrium Total Precipitable Water

The total precipitable water (W) field represents the balance between the net sources and sinks which is achieved by the moisture transport. The 5-year mean DJF and JJA W fields from GEOS-5 AGCM and from SRB are shown in figures 29 and 30 and are relatively zonal, with a maximum in the tropics and a decrease poleward, corresponding to the atmosphere's temperature-related ability to hold water. The major departures from zonality are near the western coasts of the continents,

where W is sensitive to topography and to cold ocean currents in regions of oceanic upwelling. The general agreement between GEOS-5 AGCM and SRB is good, in that GEOS-5 AGCM captures the general behavior and major departures from zonality and the seasonal shift of the maximum W with the ITCZ. The difference plots (bottom panel for each season) show that W in GEOS-5 AGCM is generally wetter than the SRB in both DJF and JJA. The wet bias in the AGCM is in the tropical regions in DJF, and is generally less than 1 g cm^{-2}. In JJA the wet bias is present in the northern hemisphere extratropics as well as the tropics, and is as large as 1.5 g cm^{-2}. The wet bias is related to the re-evaporation of rainfall simulated by the AGCM, and is discussed in section 4.

3.4 Top of Atmosphere Energy Balance

The net radiation flux at the top of the atmosphere (TOA) is the balance between the net incoming solar and outgoing terrestrial radiation, and can be expressed:

$$F_{net} = F_{sw^{\downarrow}} - F_{sw^{\uparrow}} + F_{lw^{\downarrow}} - F_{lw^{\uparrow}} \tag{2}$$

where F_{sw} terms are the upward and downward shortwave fluxes, F_{lw} terms are the longwave fluxes, and $F_{lw^{\downarrow}} = 0$.

The net radiation at any location depends largely on the orientation of the earth with respect to the sun, on the surface reflectivity, on the amount and height of the clouds, and on the surface temperature.

3.4.1 Total Atmospheric Radiation

The earth is assumed to be in approximate radiative balance, meaning that the globally averaged temperature is nearly constant during the year. The global net radiation at the top of the atmosphere, therefore, which represents the balance between the net incoming solar and net outgoing terrestrial radiation, is close to zero. In the GEOS-5 AGCM simulation the balance is held to within approximately 1 W m^{-2}. The horizontal distribution of the different components of

the radiation budget have important implications for the atmospheric general circulation patterns. The net cooling due to longwave radiation and the net warming due to shortwave radiation will be examined separately and together to provide the detailed description of the total atmospheric radiation budget.

The distribution of the net shortwave radiation at the top of the atmosphere depends chiefly on the earth's distance from the sun and orientation, on the surface albedo and on the cloud amount and optical properties. The distribution and amount of water vapor and ozone, the primary atmospheric shortwave absorbers, also affects the net shortwave radiation. As can be seen from the zonal mean plots of the net shortwave radiation at the top of the atmosphere, figure 31, the general character of the latitudinal distribution is determined by the incident shortwave, with a maximum in the summer subtropics and a minimum at the winter pole. This general behavior is certainly captured by the GEOS-5 AGCM, although in both DJF and JJA we see that the summer maximum is shifted slightly poleward relative to the CERES climatology. In addition, the tropical net shortwave is underestimated in the GEOS-5 AGCM by up to 15 W m^{-2}. The lat-lon maps of GEOS-5 AGCM-CERES outgoing shortwave differences, seen in the bottom panel of figures 33 and 32, show that in DJF the poleward shift is present at all longitudes, while in JJA there is a large overestimate of net shortwave radiation over cold ocean regions near the west coast of the North and South American continents. This will be shown in section 3.4.2 to be related to the absence of low level cloud cover in those regions.

The outgoing longwave (OLR) component of the net radiation at the top of the atmosphere depends chiefly on the surface temperature and cloud height and amount. Higher OLR values are associated with warmer surface temperatures, low cloud heights or clear skies, that is, with warmer radiating temperatures. The zonal mean plots of OLR from CERES and from the GEOS-5 AGCM, figure 34, show a smaller seasonal and latitudinal variation than the net shortwave radiation. The OLR maxima are in the subtropics, where the cloud cover is low and the surface emissions escape to space, with a local minimum near the equator, corresponding to cold radiating temperatures at cloud tops, and smaller minima. The GEOS-5 AGCM zonal mean OLR matches quite well with CERES everywhere except for the summertime extratropics, where the AGCM OLR exceeds CERES values by up to 20 W m^{-2}. The separate examination of the cloudy components in section 3.4.2 will help distinguish between errors in the outgoing longwave due to errors in cloud amount and errors due to surface temperature or atmospheric constitution. These will show that the overestimate of OLR in GEOS-5 AGCM is almost entirely due an underestimate of cloud forcing. The spatial pattern of

the OLR and the comparison with CERES is shown in figures 35 and 36. From the bottom panels of these figures we can see clearly that the overestimate of OLR in the GEOS-5 AGCM summertime extratropics is present at almost all longitudes, and that the close correspondence between AGCM and CERES zonal means in the tropics is the balance of positive and negative differences of up to 40 W m^{-2} locally. The northward shift of the ITCZ in the AGCM in DJF and the eastward shift in JJA that were shown in the precipitation field in section 3.3.2 are also apparant in the OLR difference fields.

The distribution of the net TOA radiation, in particular the latitudinal gradients, is associated with the net driving energy for the atmospheric and oceanic general circulations. The zonal mean cross sections, figure 37, show a pattern that follows the net shortwave, which is a positive maximum in the summertime subtropics, decreasing towards the summer pole and towards the winter hemisphere, crossing zero in the winter subtropics, descending to a negative minimum at the dark winter polar latitudes. The strongest north-south gradients, which imply the strongest north-south heat transports, are in the winter hemisphere. The figure shows that GEOS-5 AGCM matches the general distribution of the net radiation quite well. The errors in the shortwave and the errors in the longwave compensate and the resulting net radiation matches the CERES estimate.

3.4.2 Cloud Amount and Radiative Contribution

The net TOA radiation can be decomposed into a part due to the presence of clouds and a part due to the presence of all other atmospheric absorbers and emitters. The *Cloud Radiative Effect* (CRE) is defined (c.f., Charlock and Ramanathan, 1985):

$$CRE = F^{net} - F^{net}_{clearsky} \tag{3}$$

The general effect of clouds in the shortwave portion of the spectrum, where the suspended liquid water is highly reflective, is to reduce the net shortwave available to the atmosphere by reflecting incident radiation back to space. The amount of cooling due to clouds in the shortwave band increases with increasing cloud amount and cloud optical thickness. The change in radiative flux associated with this cooling is seen in the zonal mean shortwave CRE, figure 38. GEOS-5 AGCM and CERES both show a local maximum cooling near the equator and another in the summer

hemisphere extratropics which is largest in the southern hemisphere summer. The GEOS-5 AGCM matches the CERES summer extratropical shortwave CRE in the southern hemisphere in both DJF and JJA, and is lower than CERES in the northern hemisphere extratropics by up to 15 W m^{-2} in JJA. The GEOS-5 AGCM also overestimates the tropical shortwave CRE relative to CERES by up to the same amount. These CRE errors account for most of the error seen in the net TOA shortwave radiation of figure 31. The lat-lon plots of shortwave CRE and GEOS-5 AGCM-CERES differences, figures 39c, and 40c, indicate that the zonal mean CRE patterns are largely present at all longitudes. The excessive TOA shortwave seen off the coasts of the North and South American continents in figure 33c appears here in figure 40c and is attributed to an underestimate of shortwave cloud forcing there.

The effect of clouds in the longwave portion of the spectrum, where water drops absorb and re-emit radiation effectively, is to reduce the emissions to space by radiating at relatively low temperatures. The amount of this net warming increases with increasing cloud amount and cloud height. The cloud optical thickness is of secondary importance for the longwave cloud forcing (LWCRE) because even the thinnest clouds are effective emitters of longwave radiation. The net warming effect can be seen in the zonal mean LWCRE, figure 41, where the CRE is positive at all latitudes. The zonal mean longwave CRE has a maximum in the tropics, associated with the ITCZ, and another maximum in the extratropics which is approximately the same in summer and winter. These basic features are captured by GEOS-5 AGCM, but the AGCM underestimates the zonal mean longwave CRE at all latitudes in all seasons, by up to 15 W m^{-2} in the extratropics. This underestimate of TOA LWCRE in the AGCM is larger than the error in the OLR itself, which suggests the presence of a compensating error in the clear sky TOA outgoing longwave radiation. The compensating error in the AGCM longwave radiative fluxes is attributable to the wet bias seen in section 3.2.6, which is consistent with an overestimate of clear sky outgoing longwave radiation. The pattern of the GEOS-5 AGCM-CERES longwave CRE (bottom panel of figures 42 and 43) shows that the underestimate of LWCRE in the AGCM is present at almost all locations, except for the central equatorial Pacific in JJA where the eastward shift of the ITCZ precipitation is manifest, and is slightly larger over continental than over ocean regions.

Since the SWCRE is dominated by cloud amount and thickness, and LWCRE by cloud amount and height, discrepancies between LWCRE and SWCRE errors point to errors in cloud height or thickness, while similarities point to errors in cloud amount. Since the shortwave CRE in GEOS-5 AGCM matches well with CERES or is slightly overestimated in the tropics, and the longwave

CRE is underestimated by 30 W m^{-2} or more locally, our inference is that the OLR error is due to the cloud top pressure and not to the cloud amount. In particular, the cloud tops are too low in the atmosphere in regions of deep convection. Further evidence towards distinguishing between errors in cloud amount, height, and thickness can be gained by examining the cloud fractions.

The total cloud fraction and its global distribution is an indicator of both the radiative effects of clouds and the latent heat released during their formation. The zonal mean cloud fractions from SRB and from the GEOS-5 AGCM, fig 44, show local maxima near the ITCZ and extratropical rain bands, higher by about 0.1 in the southern hemisphere, and local minima in the subtropical subsidence regions. The GEOS-5 AGCM captures these general features, but underestimates total cloud cover by up to a fractional difference of 0.2 poleward of about 30 degrees N and S. The lat-lon plots of the cloud fraction, figures 45 and 46, show that the extratropical underestimate is present everywhere, and that the apparant closer match in the tropics represents compensating areas of negative and positive difference between the AGCM and SRB.

3.5 Land and Ocean Surface

3.5.1 Surface Energy Balance

The net surface energy balance can be expressed by the following budget equation:

$$\frac{\partial T_s}{\partial t} = F_{sw^{\downarrow}} - F_{sw^{\uparrow}} + F_{lw^{\downarrow}} - F_{lw^{\uparrow}} - SH - LH - G \tag{4}$$

where F_{sw} terms are the upward and downward shortwave fluxes, F_{lw} terms are the longwave fluxes, SH is the sensible heat flux, LH is the latent heat flux, and G is the net ground heat storage over land. T_s is the temperature of a thin skin layer at the surface. During AGCM integration the sea surface temperature (SST) is basically specified from SST analyses, so the net surface heating over the oceans serves mainly as a bulk diagnostic indicator of the interaction at the ocean-atmosphere interface.

The net radiation at surface is given by the first 4 terms on the right hand side of equation 4. The zonal mean net surface heat flux is shown in figure 47. The errors in the seasonal means are consistent with the errors in the net radiation at the top of the atmosphere (see section 3.4.1). That is, the radiation is overestimated by the GEOS-5 AGCM in the summertime extratropics, at

the surface somewhat more than at the top of the atmosphere, by up to 30 W m^{-2} at 40°N in JJA. The spatial patterns of the surface net radiation, figures 48 and 49, show that the extratropical excess of net surface radiation is largely zonal, and that the closer match at other latitudes is the result of a general overestimate of surface net radiation in the AGCM over continents, particularly in summertime, and an underestimate over the oceans.

The remaining terms on the right hand side of equation 4 are the latent heat flux (which was shown in section 3.3.1) and the sensible heat flux, which is shown here in figures 50 and 51. The differences between the GEOS-5 AGCM and the GSSTF sensible heat flux shows higher values in the GEOS-5 AGCM everywhere in both seasons. The tropical differences are on the order of a few W m^{-2}, where the effect on the sensible heat flux due to an underestimated surface wind (see section 3.2.3) is offset by the effect due to a small cold bias in the atmosphere. The larger differences between the GEOS-5 AGCM and GSSTF are in the extratropics in both seasons, where the AGCM sensible heat flux is larger than the GSSTF by up to 20 W m^{-2}.

The net surface heat flux, then, which is the sum of all the terms on the right hand side of equation 4, is expected to largely follow the pattern of the net surface radiation, given the aproximate offset of errors in the sensible and latent heat fluxes. This expectation is borne out by examining the annual mean net surface heat flux, seen in figure 52, here evaluated relative to the WHOI dataset estimate. The annual mean net heating is the relevant field to examine the potential impact on the ocean. Figure 52c shows that the GEOS-5 AGCM underestimates the net heat flux at the surface relative to the WHOI estimate everywhere except in the northern hemisphere extratropical oceans near the western boundary currents. This error in the northern hemisphere subtropics is the result of an excessive net surface radiation there, balanced and more than compensated for by the excess evaporation (and sensible heating) over the Kuroshio and Gulf Stream currents that is seen in figures 50 and 23.

If the annual mean net surface heating is integrated zonally and from the north pole to any given latitude, one obtains the implied ocean heat transport at each latitude. Figure 53 shows the GEOS-5 AGCM implied ocean heat transport, along with observational estimates from Ganachaud and Wunsch (2000) and from Trenberth and Caron (2001). Although there is a large amount of uncertainty in the observational estimate, it seems clear that the GEOS-5 AGCM northern hemisphere peak in poleward transport is slightly too weak. This reflects the underestimate of net radiative flux at the surface associated with excessive shortwave cloud forcing discussed in

section 3.4.2. It is also apparent from the figure that the GEOS-5 AGCM implied transport in the extratropics of the southern hemisphere is too weak.

3.5.2 Land Surface Temperature

Over land, where an adequate global observational climatology for the net surface energy flux is not available, any errors in the net flux into the ground will result in errors in the predicted surface temperature. The GEOS-5 AGCM surface skin temperature over land is shown relative to the CRU TS observational estimate in figures 54 and 55. In general, the AGCM skin temperature over land is warm relative to the CRU TS in the summer hemisphere by up to 10K but generally near 6K, and cold in DJF in the winter hemisphere by up to 12K but generally near 6K. This is largely consistent with the net surface radiation discussed in section 3.5.1, with the exception of equatorial Africa and southeast Asia in DJF and southern hemisphere land areas in JJA. Over all these regions the net surface radiation is high, which should result in warm skin temperatures, but the skin temperatures match closely with CRU TS estimates. It is postulated that the sensible and latent heat fluxes in those regions are overestimated and therefore offset the net surface radiation error.

4 Attributing Simulation Changes to Differences Between MERRA and Fortuna Versions

Changes in the substance or in the fundamental behavior of several physical parameterization schemes since the MERRA version of the AGCM resulted in fundamental changes in simulated climate. Section 2 summarized those changes and here we present the results of a series of experiments designed to analyze the sensitivity to specific changes in parameterizations.

4.1 Experimental Design and Results

The experiments were all conducted at 2.° x 2.5° horizontal resolution, ran for 30 years, and the differences among 30-year climatologies will be examined here. The sequence was designed to start with the Fortuna AGCM and backtrack, one parameterization change at a time or small groups

of parameterization changes as a time, to a model which replicates the MERRA AGCM simulated climate. The experiments are listed in Table 2.

The control simulation uses the Fortuna version of the GEOS-5 AGCM that was used for for all the coupled and atmosphere-only simulations performed as part of the Coupled Model Intercomparison Project (CMIP-5) by the GMAO. The version of the Fortuna AGCM used in the control simulation is also the version currently in use by the GMAO as part of the operational data assimilation system used for mission support.

Experiment 1 reverts back to the original formulation for the relationship between ocean surface roughness and stress used in the Helfand and Schubert surface layer parameterization. In addition, it reverts to the older setting for the topographic drag. The net effect for simulations at 2.° x 2.5° resolution is expected to result in an increase in surface wind speeds in the mid-range of wind speeds, that is, in the 5 m s^{-1} to 25 m s^{-1} range. This change also is expected to result in a net decrease of wind speeds in higher wind regimes, but this impact is not apparent at coarse resolutions. Surface wind speeds from the Fortuna control and Experiment 1 are shown in figure 56. The change in the simulated surface winds is most apparent in the southern hemisphere, where GSSTF (56b) shows surface winds near 8 m s^{-1}, Experiment 1 (56d) shows surface winds near 12 m s^{-1} and the Fortuna control (56a) shows surface winds near 10 m s^{-1}. The difference from the GSSTF estimate (shown in 56c and 56f) shows a reduction from up to 4 m s^{-1} in Experiment 1 to a difference of up to 2 m s^{-1} in the Fortuna control, pointing out the improvement in AGCM simulated climate due to the change in roughess formulation.

Experiment 2 combines the impact of two changes in parameterizations that impact regions that are geographically removed from one another and can be examined independently in a single experiment. These are the changes in the gravity wave drag parameterization of background drag in the tropics, and the changes in the catchment model's characterization of two elements of the surface hydrology. Experiment 2 returns to the MERRA AGCM background drag, and is therefore expected to exhibit a stratospheric wind with no quasi-biennial oscillation (QBO) variability, and returns to the MERRA hydrological parameters, which is expected to result in a land surface with a very high fraction of total evapotranspiration due to canopy interception reservoir evaporation.

The impact of the change in background non-orographic wave drag on the AGCM simulation is shown by examining the tropical (latitude range 10S to 10N) spatial average of the zonal wind as a

function of height and time, figure 57. The patterns of large easterly and westerly winds that slant downwards in pressure as time proceeds indicate the downward propagation of the variations due to the QBO. The QBO pattern is seen in figure 57a and 57c, which are the results from Experiment 1 and MERRA reanalysis. Figure 57b, however, which reflects the results of Experiment 2 which uses the old background drag formulation (from figure 5), shows no QBO pattern of variability.

The impact of the change in the surface hydrology parameters that govern the distribution of evapotranspiration over land surfaces is shown by examining the relative contributions of evaporation from the canopy interception reservoir and transpiration from vegetation elements to the total evaporation. By reducing the fractional area of a grid box assumed to be wetted by a precipitation event, and reducing the capacity of the interception canopy to hold water, the Fortuna simulation was expected to produce more transpiration and less interception loss. Figures 58a and 58b show the large increase in the fraction of evaporation due to interception loss in experiment 2 (MERRA AGCM settings) relative to experiment 1 (Fortuna AGCM settings). The compensating decrease in the fraction of total evaporation due to transpiration that occured when the settings were reverted to the ones used in the MERRA AGCM is shown in the comparison of 58c (Fortuna) and 58d (MERRA AGCM). Reverting to the MERRA AGCM settings resulted, in general, in a net increase of the total evaporation over land, as is shown in the change between 59a and 59b. The net increase in total evaporation is attributeable to the increase in the evaporation from canopy interception reservoir, which is not resisted by vegetation and occurs at the potential evaporation rate. The important exception to this behavior occurs in the central United States, where experiment 1, with the Fortuna AGCM settings, shows the larger total evaporation.

Experiment 3 adds to experiment 2 the impact of the change in the surface layer parameterization. Since experiment 1 as compared to the control evaluated the impact of the changes to the surface layer parameterization over ocean surfaces, we will evaluate the impact of the change from the Louis to the Helfand scheme over land surfaces here. The two basic changes discussed in section 2 are the removal of the viscous sublayer over land in the Helfand scheme, and the change in the stable surface layer behavior. Figure 60 shows the sensible heat flux from experiments 2 and 3 along with the difference. Figure 60c shows that over most land surfaces the difference in sensible heat flux is negative, indicating less sensible heating when using the Louis scheme. This sign of the difference is consistent with the removal of the viscous sublayer over land surfaces in the Helfand scheme, which would remove some resistance to turbulent exchange that is present over unvegetated land surface in the Louis scheme. Figure 60c also shows regions where the sensible heat flux is greater in

the Louis scheme than in the Helfand scheme. These are regions where the surface layer is stable, and where the sensible heat itself is largely downward (that is, the air temperature is greater than the skin temperature). The change in stability functions between the Louis and Helfand scheme, which allows more turbulent exchange in the Helfand scheme, is consistent with the sign of the difference in sensible heat flux in regions where the heat flux is downward.

Experiment 4 adds to experiment 3 the impact of the changes in the atmospheric turbulence parameterization. These changes were specifically targeted for the impact in coupled atmosphere-ocean simulations. The impact of removing these changes inhibits the diffusion from the Louis and Geleyn scheme and increases the diffusion from the Lock scheme in the presence of strong wind shear. This direct impact of the change in the turbulence parameterization is an increase in the turbulent diffusion coefficient in the Fortuna AGCM simulation. Figure 61a, the zonal mean JJA averaged turbulent diffusion coefficient for heat (K_h) from experiment 3, shows larger values of K_h near the column maximum than seen in figure 61b. The vertical extent of the K_h values is also larger in 61a. The combined impact of reverting to the MERRA AGCM behavior of the turbulence scheme also resulted in a reduced east-west gradient of boundary layer depth across the tropical Pacific. Figure 62 shows the difference (experiment 3 minus experiment 4) of the planetary boundary layer (PBL) height, averaged over DJF. The figure shows small differences along the equatorial latitudes in the eastern Pacific (110W to 90W), and larger differences to the west. This added horizontal gradient of the PBL height in the Fortuna AGCM simulation was designed to contribute to an improved simulation of the oceanic pycnocline in the equatorial Pacific and the reduction of a cold bias in the eastern Pacific in coupled atmosphere-ocean simulations.

Experiment 5 adds to experiment 4 the impact of the change in the relative humidity threshold used in the prognostic cloud scheme for condensation, sublimation and evaporation of suspended water/ice and precipitation (RH_{crit}). Removing this change, which for much of the atmosphere means a larger RH_{crit}, should result in a simulation that is generally wetter because the atmosphere is being adjusted back to a higher relative humidity. The zonal mean relative humidity from experiments 4 and 5, along with the difference, is shown in figure 63. The difference, experiment 5 minus experiment 4, shows a clear increase in relative humidity in the MERRA AGCM due to the increase in RH_{crit}. Relative to available observational verification (shown in section 3.2.6), the Fortuna AGCM shows a general wet bias, which means that the experiment 4 relative humidity field is closer to the observed than experiment 5's RH field. In addition to having a substantial impact on atmospheric moisture levels, the change in RH_{crit} also had an impact on the distribution of cloud

cover. Figure 64 shows the zonal mean cloud cover from experiments 4 and 5, and an observational estimate of zonal mean cloud cover from AIRS. The MERRA AGCM experiment, experiment 5 (64a) shows increased cloud cover in the 300-600 mb range relative to the Fortuna experiment, in particular at high latitudes in both hemispheres. In this regard, the Fortuna experiment result more closely resembles the AIRS cloud cover estimate (64c). The increased cloud cover aloft in the MERRA AGCM experiment is also consistent with an increased RH_{crit} there, since the higher RH_{crit} results in an atmosphere which is wetter in the mean and has more cloud. The MERRA AGCM result also shows smaller cloud cover near the boundary layer at almost all latitudes. At high latitudes, the Fortuna boundary layer cloud more closely resembles the AIRS estimate, in the tropics the Fortuna boundary layer cloud is larger than AIRS, while the MERRA AGCM boundary layer cloud is smaller. The change in boundary layer cloud between the MERRA AGCM and Fortuna is not consistent with the RH_{crit} change there, but RH_{crit} is not consistently higher in Fortuna throughout the boundary layer, and it is also less of a determining factor for model mean relative humidity in the boundary layer.

Experiment 6 examines perhaps most crucial parameterization change, which is the increase in the amount of suspended and falling liquid and ice re-evaporation parameterized in the moist physics. The removal of this change is expected to result in a drier atmosphere, in particular aloft. This simulation is expected to resemble in large part the climatology of the AGCM used as part of MERRA. Figure 65 shows the direct impact of the change from the Fortuna AGCM to the MERRA AGCM re-evaporation, and, as expected, shows the drying related to the reduced re-evaporation in the MERRA AGCM. Figures 65a-c show the change in total precipitable water, and the difference (MERRA AGCM minus Fortuna, shown in 65c), is negative always everywhere. The vertical distribution of the moisture is shown in figures 65d-f, and the difference plot (65f) also shows an almost global reduction in atmospheric water vapor. The resulting mean circulation in boreal winter underwent a substantial change associated with this drying, and represents the most substantial impact on the simulated climate of all the elements of the MERRA AGCM to Fortuna AGCM transition. Figure 66 shows the subtantial impact that changing the moisture levels had on the 3-year averaged December-January-February total precipitation. Given the GPCP climatology as a reference, the Fortuna AGCM (experiment 5, figure 66d) exhibits an Intertropical Convergence Zone (ITCZ) structure that is properly placed in longitude, a South Pacific Convergence Zone (SPCZ) that properly slants from the western Pacific to the southeast, and more accurately simulated storm track maxima. The precipitation field represents improvements in all these areas related to the MERRA AGCM-like simulation (experiment 6) shown in figure 66a. The change in the tropical

precipitation field related to the additional drying in experiment 6 also resulted in substantial changes in the Pacific teleconnection patterns, specifically the Pacific-North-America (PNA) pattern in boreal winter. The eddy height field is an indicator of the strength of the PNA, and is shown in figure 67 in relation to the eddy height from MERRA reanalysis. The Fortuna AGCM simulated PNA pattern (figure 66d) has a stronger and more properly oriented ridge near the west coast of North America relative to the PNA as simulated by the MERRA AGCM (figure 66a). This change has implications for the poleward propagation of heat and momentum. The standard deviation of the difference from MERRA is also substantially reduced in experiment 5 (16.8 m) relative to experiment 6 (20.3 m). The direct impact of the change in re-evaporation was also evident in the boreal summer climatology. Figure 68 shows this both in the total precipitable water fields and in the specific humidity fields, which exhibit differences between experiments 5 and 6 that are of the order of the differences seen in boreal winter. The impact on the mean summertime circulation, however, was minimal, and the errors seen in the MERRA AGCM precipitation and wind fields are apparent in the Fortuna AGCM as well (shown in sections 3.3.2 and 3.2).

Experiment 7 is the last experiment in the series, incorporating the effect of all the fundamental changes between MERRA and Fortuna AGCM. The final parameterization change included in Experiment 7 is the removal of the intermittency in the gravity wave drag scheme. The intermittency factor was increased in Fortuna, and the removal of this change is therefore expected to decrease the orographically induced drag in the southern hemisphere, thereby depositing less momentum aloft and increasing the strength of the westerlies. The zero-wind contour in the southern hemisphere can be used as an indicator of the level and timing of the stratospheric jet breakup. Figure 69 shows the zero-wind contour from experiment 7, experiment 6, and MERRA. At the 2 degree horizontal resolution of the simulations described here, the zero wind line is higher in altitude and delayed in time relative to MERRA in both simulations, reflecting a delayed stratospheric jet breakup. The decreased intermittency factor in experiment 7, however, delays the jet breakup even more, showing the improvement in the Fortuna simulation relative to the MERRA AGCM simulation. At higher spatial resolution (not shown) the increase of intermittency factor in Fortuna is effective in producing a reasonable evolution of the polar vortex breakdown in the southern Hemisphere.

5 Synthesis and Discussion

A summary of the atmosphere-only climate simulations of the version of the GEOS-5 AGCM that was used as part of CMIP5 simulations has been presented here. In addition, the developments since the GEOS-5 AGCM version used as part of MERRA that lead to substantial improvements in simulated climate were characterized. Based on comparisons with available observational estimates of the climate, there are two central remaining areas for development: the cloud radiative interactions and the surface energy and momentum fluxes over the oceans.

The issues with the clouds and radiation were discussed in sections 3.4 and 3.4.2 and can be summarized as follows:

- In the tropics: There is too much cloud cover, too much shortwave cloud radiative forcing (defined in equation 3), and too little longwave cloud radiative forcing. We suspect from the similarity in error patterns of the shortwave cloud forcing and the cloud amount that the parameterization of optical depth is adequate, and that a reduction of cloud amount would reduce both types of error. The behavior in the longwave, however, with too much cloud cover and not enough cloud forcing, indicates that the cloud tops are too low in the model atmosphere. Higher cloud tops which radiate at lower temperatures would result in outgoing longwave radiation minima that are more consistent with observations.
- In the mid-latitudes: There is too little cloud cover and too little CRE both in the shortwave and in the longwave. We conclude that the cloud properties are adequately simulated, but the cloud amounts need adjusting/tuning.
- In the high-latitudes: There is too much cloud cover and too little CRE in the shortwave. From this it is concluded that the optical depths are too thin. An adjustment is needed in both the optical depths and cloud amounts.

The errors in GEOS-5 AGCM climate in the mid- and high latitudes can be partially addressed by adjusting several of the thresholds in the parameterization of cloud-radiative interactions. The tropical excess of outgoing longwave radiation at the top of the atmosphere in GEOS-5 AGCM simulations is attributed to cloud tops that are too low in the atmosphere. This is connected to the behavior of the cumulus parameterization and is more difficult to address than the errors in the cloud

amount and optical properties. There are other comparisons against observations that support the conclusion that the vertical extent of convection as simulated by the cumulus parameterization is not adequate. The detrainment of cloud water by the cumulus parameterization is a primary mechanism by which water vapor reaches the upper troposphere. Comparison of specific humidity in the upper troposphere against MERRA indicates that GEOS-5 AGCM is excessively dry. At 200 mb GEOS-5 AGCM values are half of what is estimated by the MERRA reanalysis, and at 150 and 100 mb GEOS-5 AGCM values are almost an order of magnitude too low. This excessively dry upper troposphere is also evident in the relative humidity field.

More fundamental improvements in the clouds and cloud radiative properties are possible in the context of the next generation AGCM. The inclusion of a 2-moment description of cloud microphysics along with an algorithm for the interaction between aerosol and cloud formation allows for a more accurate geographical distribution of cloud effects. In addition, the next generation AGCM will be run on an enhanced vertical grid, allowing for the possibility of an improved simulation of boundary layer clouds.

A Verification Data Sources

Many of the model derived quantities which are important to climate studies are quite difficult to measure, and observational data on the climate scale is scarce. Much of the observational data is also indirect, and neccesitates the use of additional parameterizations and algorithms to derive the actual fields used for verification. The uncertainties in these data, therefore, must be considered when comparing them with the AGCM. The combination of satellite and ground based observations chosen for verification here are considered as reliable standards by which to judge the AGCM climate.

Verification for the mean state variables, particularly temperature, zonal wind and related fields is provided by the climatology of the Modern-Era Retrospective Analysis for Research and Applications (MERRA, Rienecker et al., 2011). MERRA has two primary objectives: to place observations from NASAs Earth Observing System satellites into a climate context and to improve upon the hydrologic cycle represented in earlier generations of reanalyses. It covers 1979-present with ongoing reanalyses at 0.5° resolution with 72 vertical levels.

ERA-Interim (ECinterim, Dee et al., 2011) is used for a second estimate of model-dependant fields, including humidity, meridional wind and related fields at a resolution of approximately 0.7° and 61 levels. It is a reanalysis by the ECMWF currently produced from 1979 onwards using the ECMWF forecast model and is intended to bridge from the earlier ERA-40 reanalysis to a future project that will cover the 20th century.

Validating data for ocean surface values of evaporation, windstress, wind speed, and net heat flux are obtained from the Goddard Satellite-based Surface Turbulent Fluxes dataset (GSSTF version 2b, Shie et al. 2009), which covers 1987 through 2008 and was created for global energy and water cycle research. The dataset values are derived from a combination of surface wind, total precipitable water, and microwave brightness fields from the Special Sensor Microwave Imager (SSM/I) Version-6 satellite product, and sea surface skin temperature, 2-meter air temperature, and sea-level pressure from the NCEP/DOE Reanalysis-2. These fields are used as input to the GSSTF bulk flux model, which produces daily global fields on a 1°x1° grid.

The observational estimate for total precipitation is the Global Precipitation Climatology Project (GPCP) satellite-gauge precipitation product of Huffman et al. (1995). The precipitation estimate is a combination of microwave satellite data, infrared satellite data, rain gauge analyses, and numerical weather prediction models. The first step of the technique used to combine the various data sources is the development of a multi-satellite product using microwave and infrared at low latitudes, and microwave data alone at higher latitudes. The second step is the inclusion of the rain gauge analysis, weighting each field by its inverse relative error variance. Finally, ECMWF numerical model results are used to fill data voids in the combined satellite-gauge estimate. The bias estimated from this technique is 3.7 mm month^{-1}.

Data for verifying monthly mean land surface temperatures are obtained from the Climate Research Unit (CRU) TS 3.0 dataset (Mitchell and Jones 2005). The dataset produced at the Climate Research Unit at the University of East Anglia, and is intended to be used for study of regional climate variability. It is constructed from ground station records that have been corrected for inhomogenities using the GHCN method modified to handle incomplete station records and neigboring stations that only partly overlap in time. The results are interpolated to a 0.5° lat-lon grid with zero-anomaly "dummy" stations inserted into regions of no stations.

Verification data for top-of-atmosphere (TOA) radiative fluxes are from the Clouds and the Earth's

Radiant Energy System (CERES) Energy Balanced and Filled (EBAF) data set. These data were obtained from the NASA Langley Research Center Atmospheric Science Data Center (Wielicki, et al,1996). The EBAF product provides monthly mean TOA radiative fluxes constrained such that the 5-year averaged global net TOA flux is consistent with the best estimate of heat storage in the Earth-atmosphere system (0.9 W m^{-2}). CERES EBAF is primarily intended for studies that use Earth Radiation Budget (ERB) data for climate model evaluation, estimating the Earth's annual global mean energy budget, and in studies that infer meridional heat transports. The CERES EBAF dataset consists of monthly 1° by 1° regional, zonal, and global averages of TOA longwave (LW), shortwave (SW), and net (NET) fluxes under clear and all-sky conditions. It is derived from the Terra SRBAVG-GEO Edition2D-rev1 and SSF Edition2B-rev1 data products. Temporal coverage for the EBAF Terra Edition1A data set is from March 2000 through October 2005.

The Surface Radiation Budget (SRB) calculations of Pinker and Laszlo (1992) are used as verification for the surface shortwave fluxes and the cloud amount. The SRB algorithms use measurements from the ERBE and International Satellite Cloud Climatology Project (ISCCP) satellites and a radiative transfer scheme to produce surface shortwave fluxes. The radiative transfer algorithm accounts for absorption by ozone and water vapor, for scattering by molecules, aerosols and cloud drops, and allows for multiple reflections between the atmosphere and the surface. The cloud fraction is the ratio of the number of ISCCP cloudy sky pixels to the number of total sky pixels. The radiative fluxes derived from these methods were verified in select locations against land-based direct measurements and are considered accurate to within approximately 5 W m^{-2}.

The Comprehensive Ocean-Atmosphere Data Set (COADS) was used by da Silva et al (1995) to estimate the various terms of the surface energy budget, surface wind stresses, cloud cover, precipitation, and other surface fields over the tropical and extratropical oceans. Observations taken during 1945-1989 were corrected for systematic biases and subjected to a quality control, and the derived quantities were interpolated to a 1° by 1° grid, filling in data gaps using a sinusoidal interpolation. The wind stresses and surface fluxes were calculated using a similarity theory parameterization that calculates the transfer coefficients according to Large and Pond (1981 and 1982). The precipitation estimates were made using Tucker's (1961) regression formula based on "present weather" observations with the tropical correction of Dorman and Bourke (1978). Surface radiation estimates were made using empirical formulae to approximate cloud attenuation, surface albedo and atmospheric transmissivity.

The net surface heat flux over the ocean is verified with the OAFlux product by Woods Hole Oceanographic Institution (WHOI, Yu et al. 2008). This dataset is produced with a bulk flux model using for input a blend of satellite retrievals and atmopsheric reanalyses and results in a 1° gridded daily and monthly mean field.

B Acknowledgements

The GEOS-5 AGCM development in the Global Modeling and Assimilation Office is funded by NASAs Modeling, Analysis and Prediction (MAP) program under WBS 802678.02.17.01.211 and 802678.02.17.01.25. The authors gratefully acknowledge the support of David Considine, the MAP project manager. We appreciate the contribution of the many others in the GMAO who participated in various key ways to the development of the GEOS-5 AGCM. The analysis of GEOS-5 AGCM simulations at many spatial and temporal scales was performed by Siegfried Schubert, Yehui Chang and Myong-In Lee, and the analysis of the GCM performance in data assimilation and numerical weather prediction modes was performed by Stephen Bloom, Gary Partyka and Austin Conaty. The feedback from William Putman about the performance of the AGCM at very high horizontal resolution was critical in the ability to run the GEOS-5 AGCM seamlessly across a wide range of resolutions, and the analysis of the transport of tracers done by Lesley Ott aided in the understanding of model errors. In addition, the feedback to AGCM development from GMAO scientists involved in the development of the other component models of the GEOS-5 GCM, including Yury Vikhaelev, Bin Zhao, J. Eric Nielsen, Arlindo da Silva, Randal Koster, Rolf Reichle and Sarith Mahanama, was invaluable. In addition, the efforts of Peter Norris in the development and testing of the satellite simulator component of the GCM are appreciated. The authors also gratefully acknowledge the contributions to the AGCM infrastructure of Atanas Tryanov, which made the AGCM tractable and portable to different platforms, and the efforts of Dan Kokron to implement portability. Both of these contributions made the simulations possible. The simulations were performed at the the NASA Center for Climate Simulation (NCCS) at Goddard Space Flight Center and at the NASA Advanced Supercomputing (NAS) Division at Ames Research Center. The authors gratefully acknowledge the support of personnel at both of those computing centers.

Model Changes from MERRA to Fortuna

Module	Algorithm Change	Comments
Moist	Increased re-evaporation of precipitation	Fundamental change in model climate
	Modified autoconversion	Fundamental change in model climate
	Modified effective radius of cloud drops	Fundamental change cloud forcing
	Anvil fractions cut in half	Fundamental change cloud forcing
	Autoconvert warm fog	Important change in coupled simulations
	New critical RH with resolution dependance	Substantial change in simulated moisture
	Cloud base set at PBL depth	Remove clouds detraining below PBL height
	RAS time scale no longer depends on turbulence	
	Stochastic RAS with resolution dependance	Substantial impact at high resolution
Turb	Remove restrictions on diffusion from Louis	Increase near surface diffusion
	Reformulate turbulent length scale in Louis	
	Reduce Lock scheme when there is wind shear	Impact on marine PBL
	Reduce cloud top entrainment for Lock plumes	Impact on marine PBL
Surf	Implement Helfand and Schubert scheme	
	Remove viscous sublayer over land surfaces	Improve land temperatures
	Change ocean roughness for middle wind regimes	Reduce wind bias in S. Ocean
	Change ocean roughness high wind regimes	Increase tropical cyclone intensity
Land Surf	Changed parameters for evapotranspiration	Impact on ratio of surface to canopy evaporation
GW Drag	Changed profile of background drag	Substantial impact on QBO
	Added intermittency of drag	Impact on timing of winter jet breakup

Table 1: Changes in GCM Algorithms from MERRA to Fortuna

Sensitivity Experiments

Experiment	Description
Control	
Exp 1	Back off change in ocean roughness
Exp 2	Exp 1 + Back off gravity wave background drag and surface hydrology
Exp 3	Exp 2 + use old surface layer parameterization
Exp 4	Exp 3 + Back off increase of Richardson-number diffusion
Exp 5	Exp 4 + Back off decrease of critical RH aloft and decrease below
Exp 6	Exp 5 + Back off increase of all re-evaporation
Exp 7	Exp 6 + Back off gravity wave drag intermittency

Table 2: Experiments to attribute MERRA to Fortuna AGCM simulation changes to changes in parameterizations.

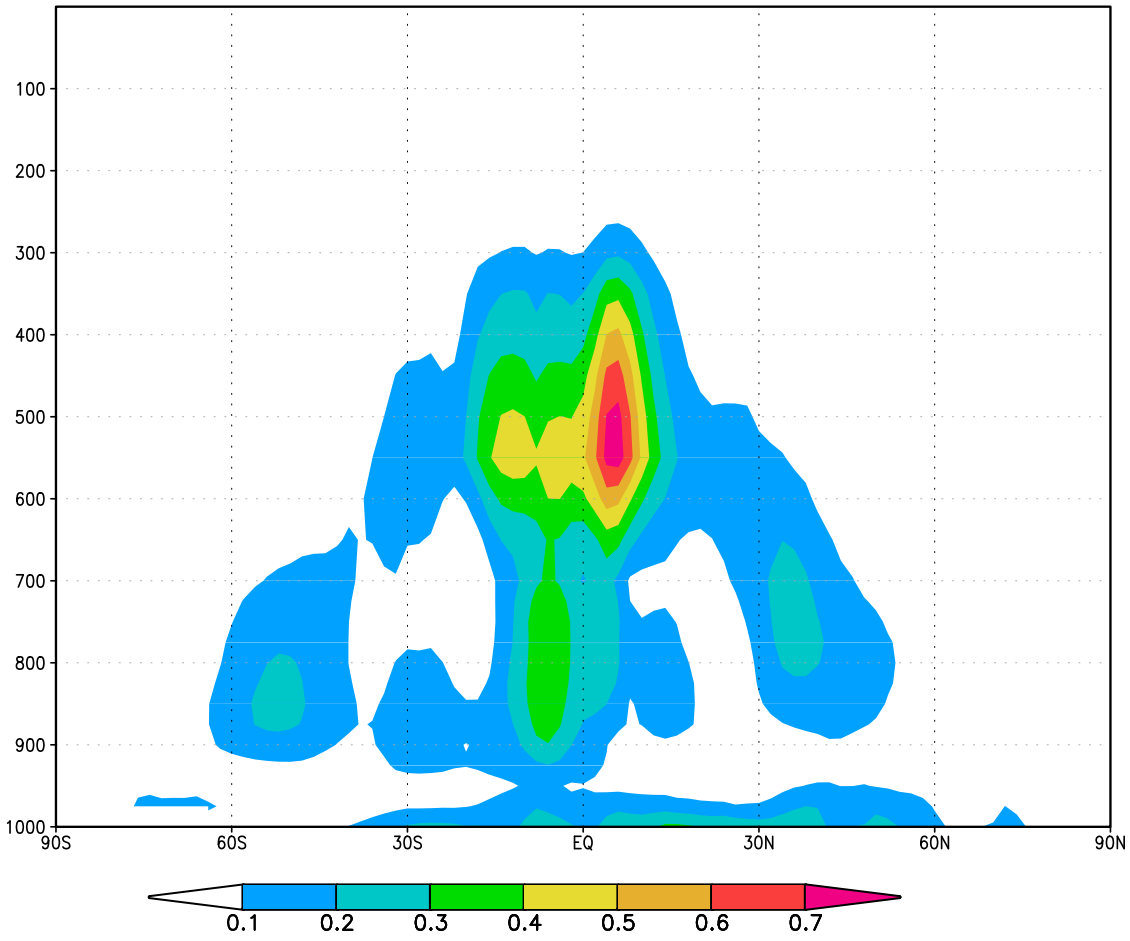

Figure 1: The difference (Fortuna AGCM minus MERRA AGCM) of zonal mean specific humidity source term due to all re-evaporation for December-January-February.

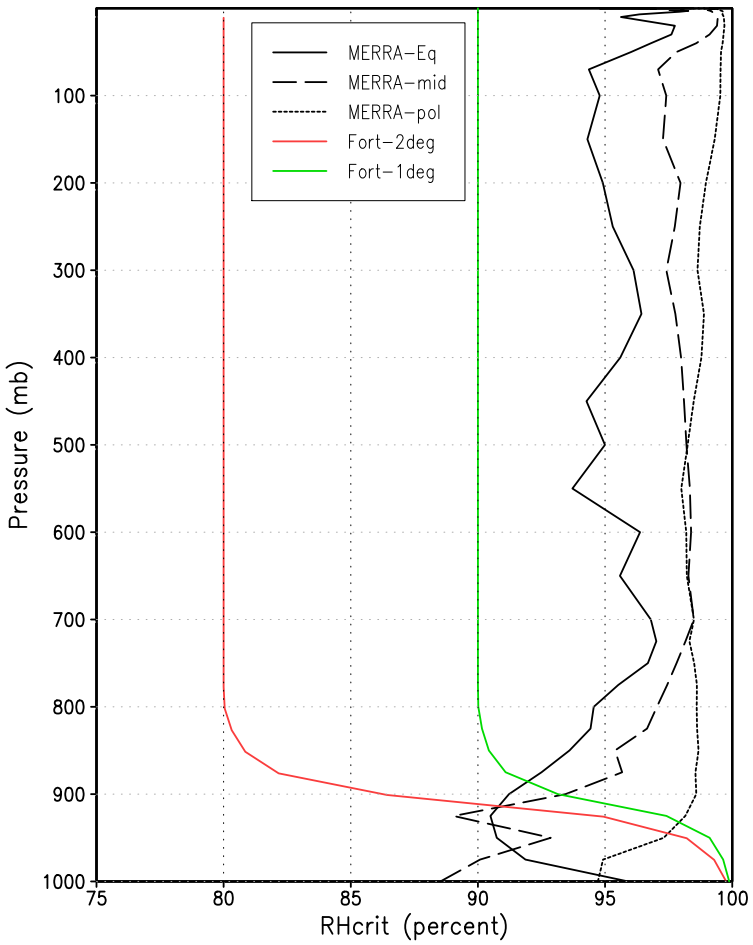

Figure 2: Critical relative humidity. Black from MERRA AGCM formulation at different latitudes, green from Fortuna AGCM formulation for 1° resolution, and red from Fortuna AGCM formulation for 2° resolution.

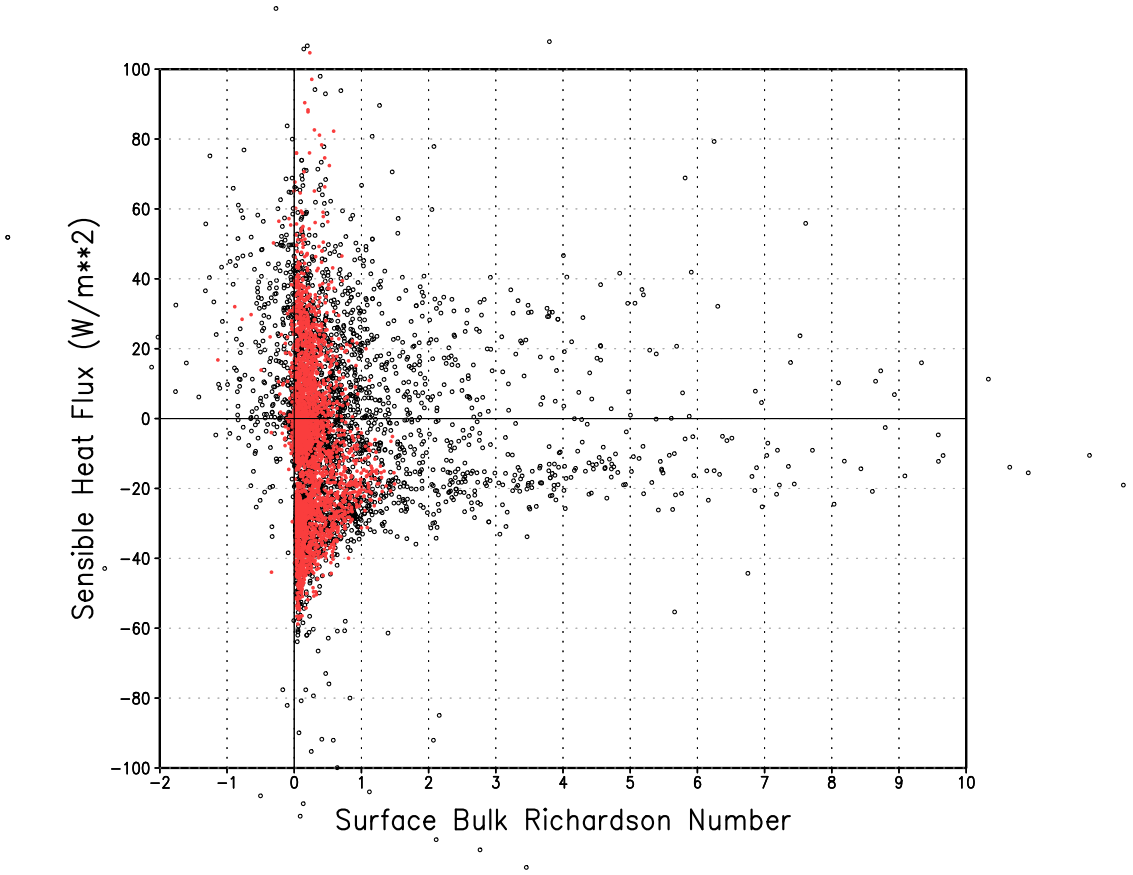

Figure 3: Surface bulk Richardson number as a function of sensible heat flux in W m^{-2} in a single July from experiment 3 (red) and experiment 2 (black).

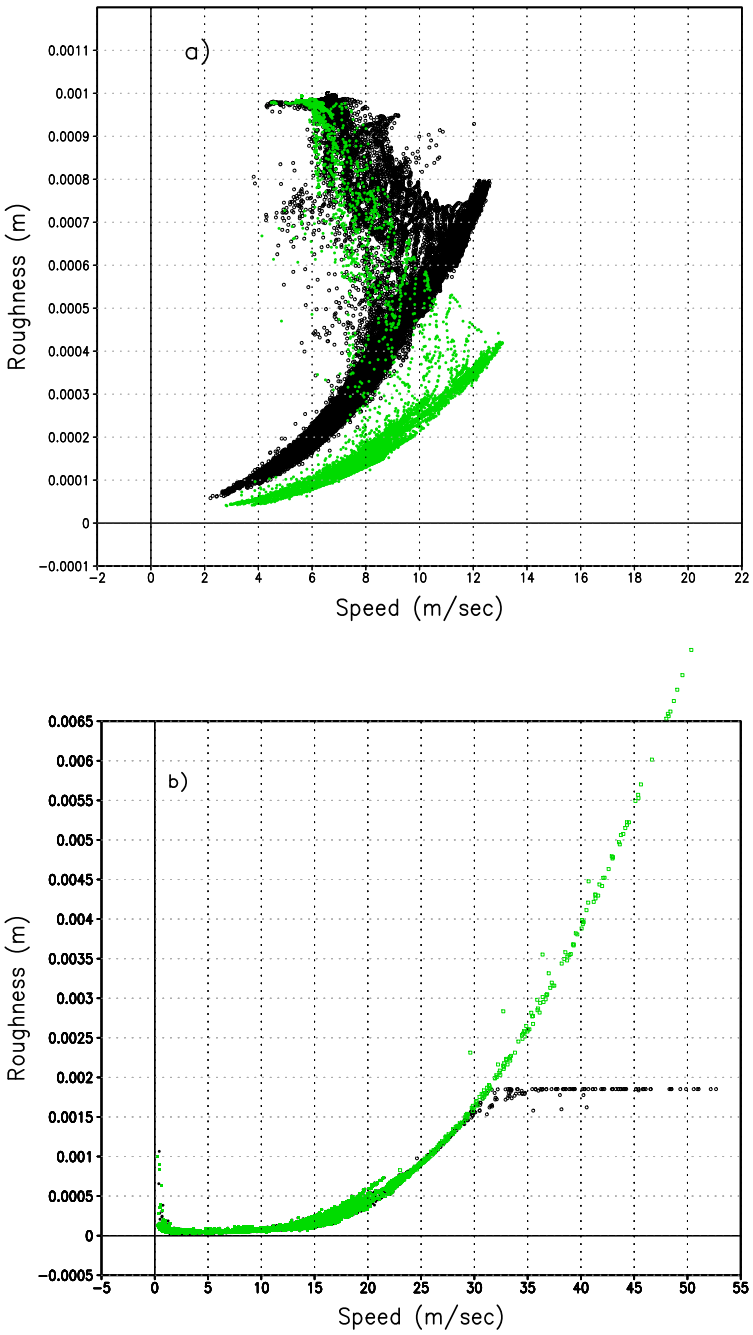

Figure 4: Scatter diagram of surface wind speed (m $\sec^{-1}$) versus ocean roughness (m) in the MERRA and Fortuna AGCMs. a) diagram focusing on medium range of wind speeds, Fortuna shown in black and MERRA in green, and b) diagram extending to high wind regimes, MERRA shown in green and Fortuna in black.

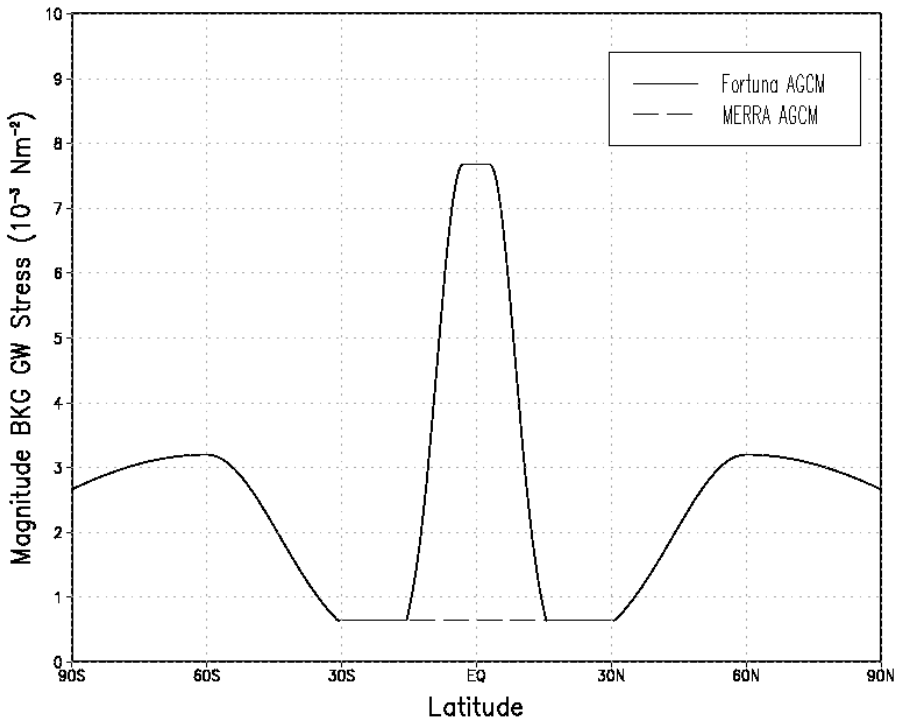

Figure 5: Background nonorographic drag from the MERRA and Fortuna AGCM simulations

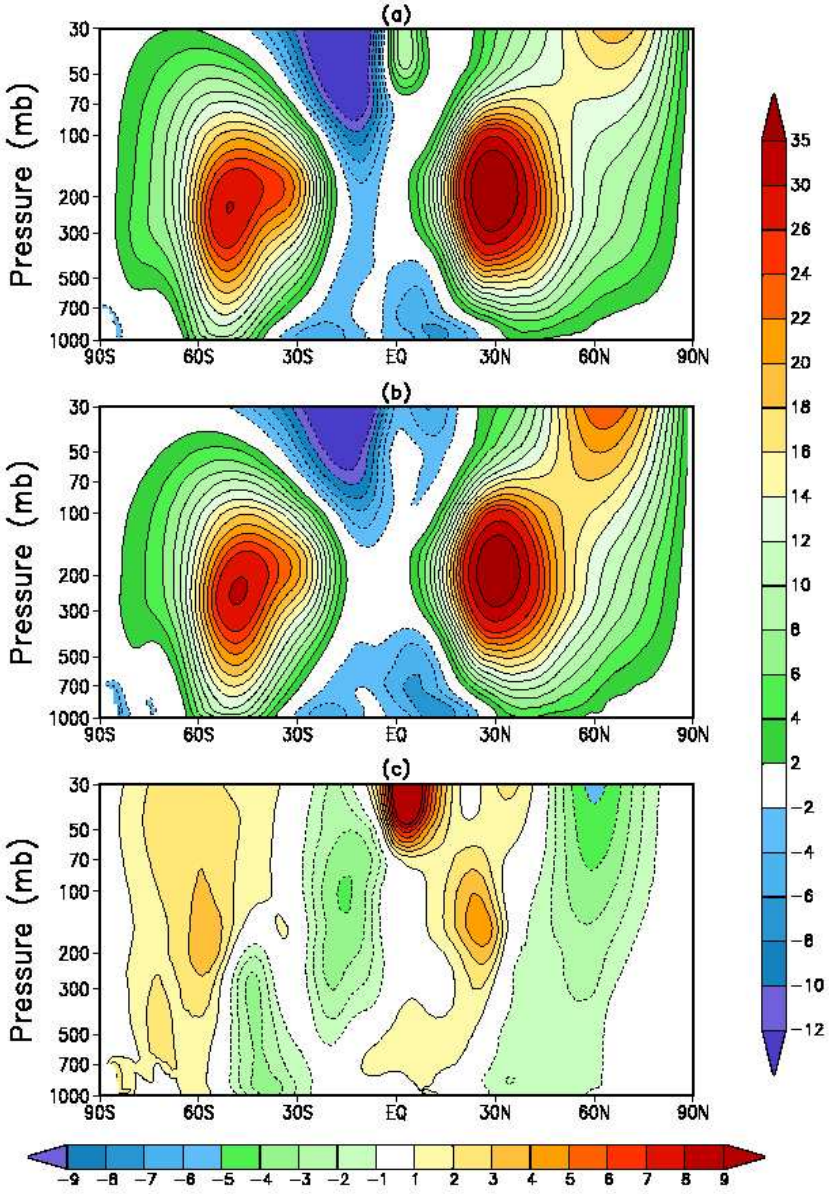

Figure 6: December-January-February Zonal Wind Climatology in m $\sec^{-1}$ from a) GEOS-5 AGCM b) MERRA and c) the difference, GEOS-5 - MERRA.

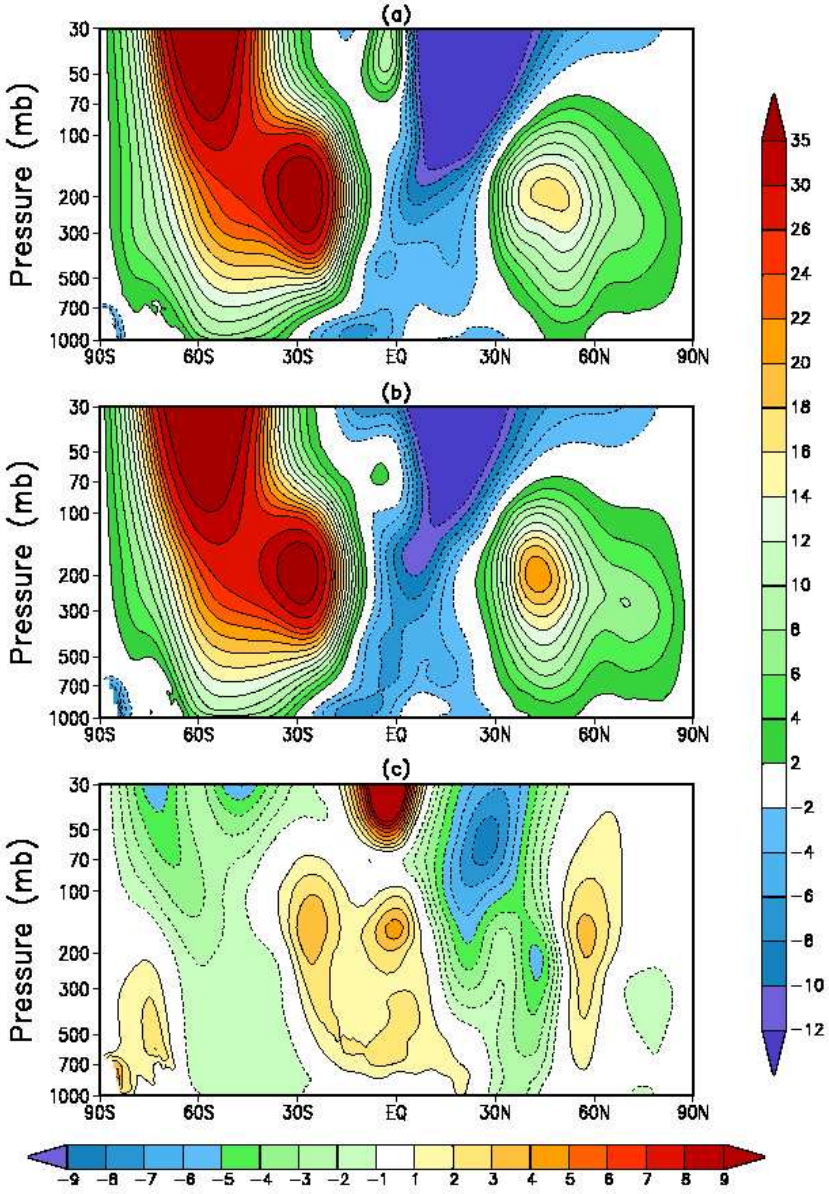

Figure 7: June-July-August zonal mean zonal wind in m $\sec^{-1}$ from a) GEOS-5 AGCM b) MERRA and c) the difference, GEOS-5 - MERRA.

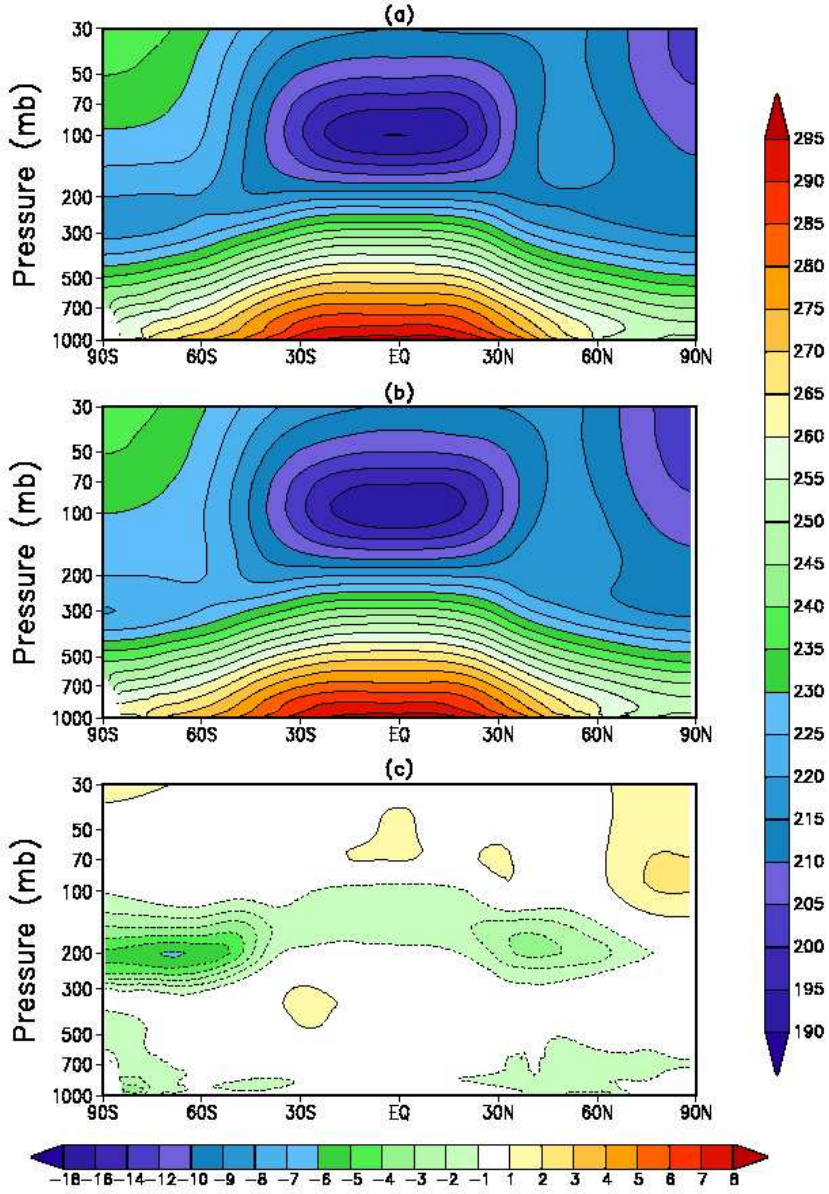

Figure 8: December-January-February Temperature Climatology in K from a) GEOS-5 AGCM b) MERRA and c) the difference, GEOS-5 - MERRA.

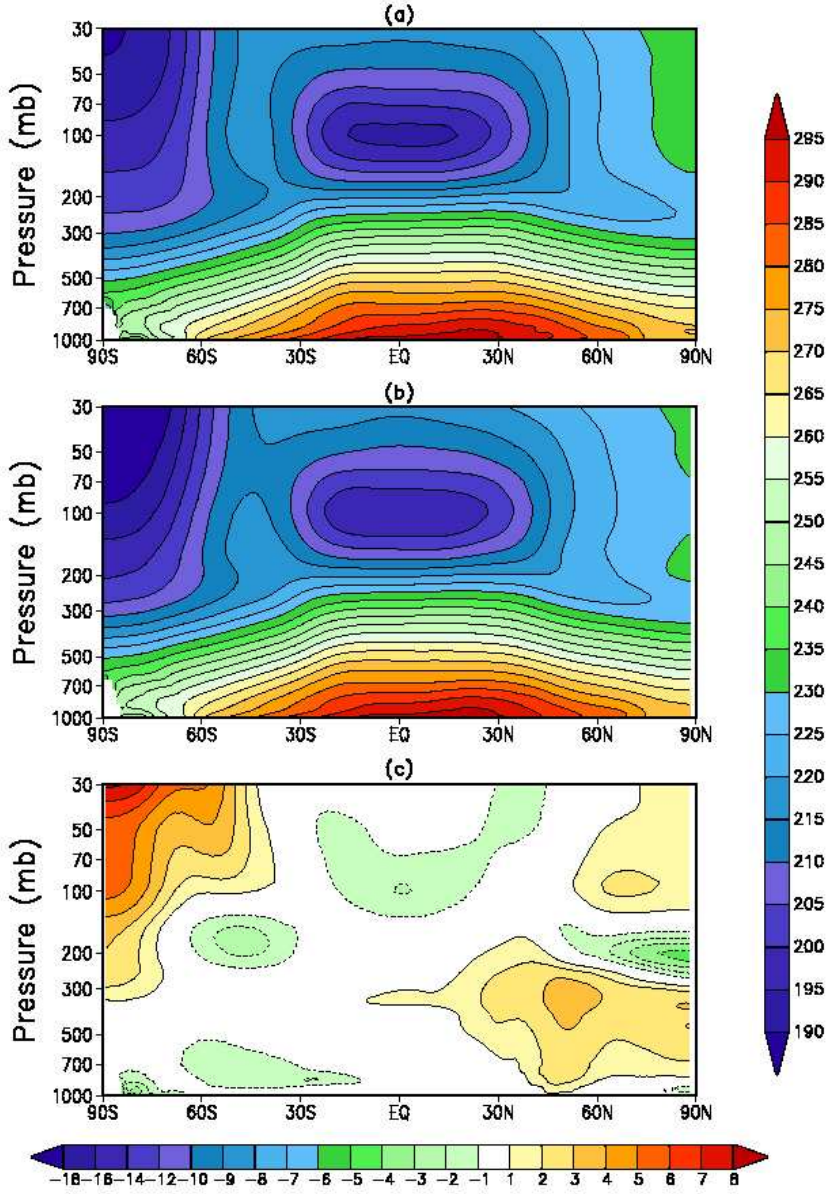

Figure 9: June-July-August Temperature Climatology in K from a) GEOS-5 AGCM b) MERRA and c) the difference, GEOS-5 - MERRA.

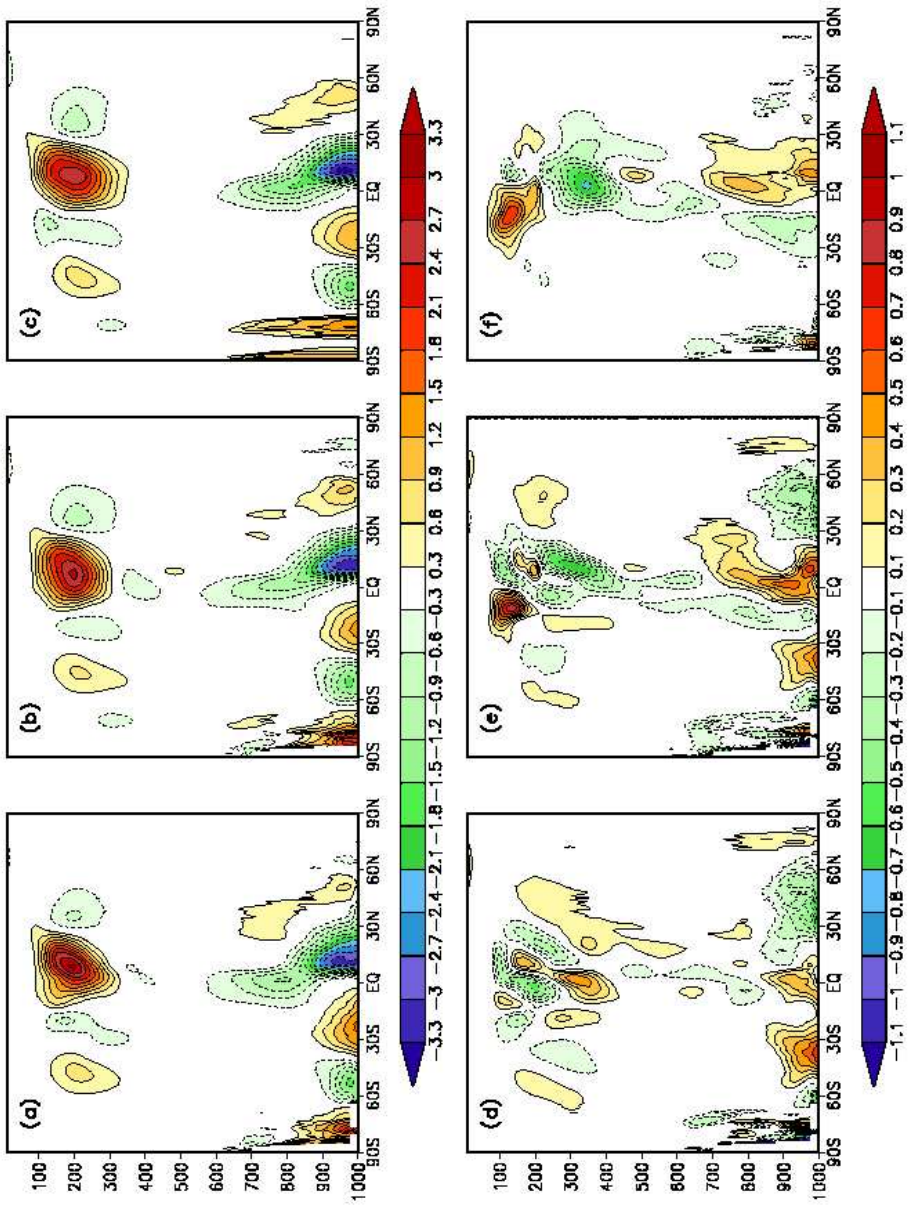

Figure 10: December-January-February Meridional Wind Climatology in m sec^{-2} a) from GEOS-5 AGCM, b) from MERRA Reanalysis, c) ECinterim reanalysis, d) GEOS-5 AGCM - MERRA, e) GEOS-5 AGCM - ECinterim, f) MERRA - ECinterim.

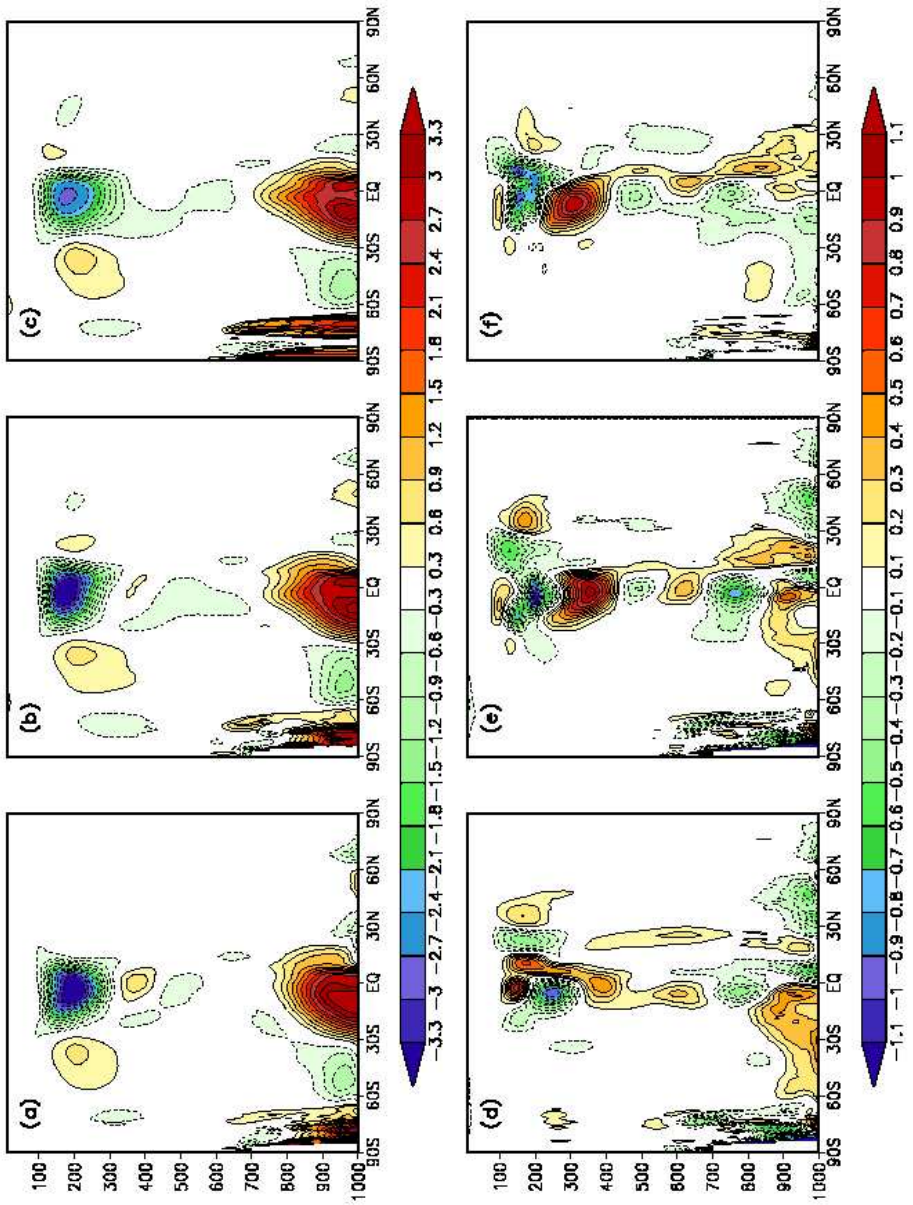

Figure 11: June-July-August Meridional Wind Climatology in m $\sec^{-2}$ a) from GEOS-5 AGCM, b) from MERRA Reanalysis, c) ECinterim reanalysis, d) GEOS-5 AGCM - MERRA, e) GEOS-5 AGCM - ECinterim, f) MERRA - ECinterim.

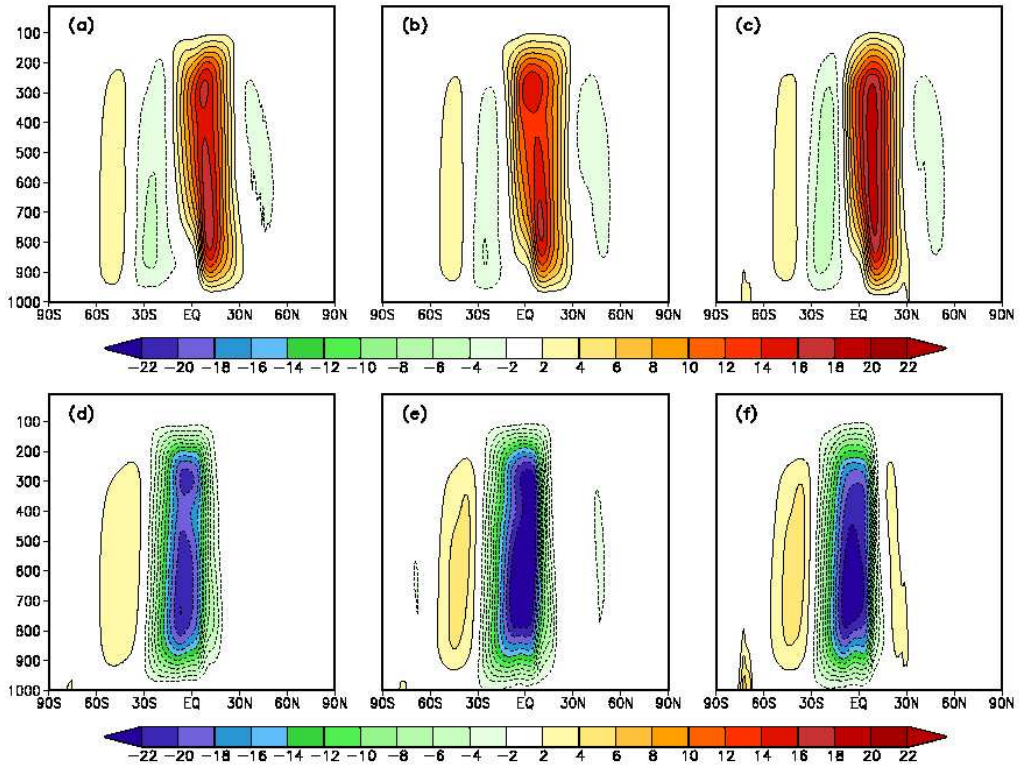

Figure 12: Meridional Mass Streamfunction in 10^8 kg $\sec^{-1}$ during December-January-February from a) GEOS-5 AGCM, b) MERRA, and c) EC-Interim, and during June-July-August from d) GEOS-5 AGCM, e) MERRA, and f) EC-Interim.

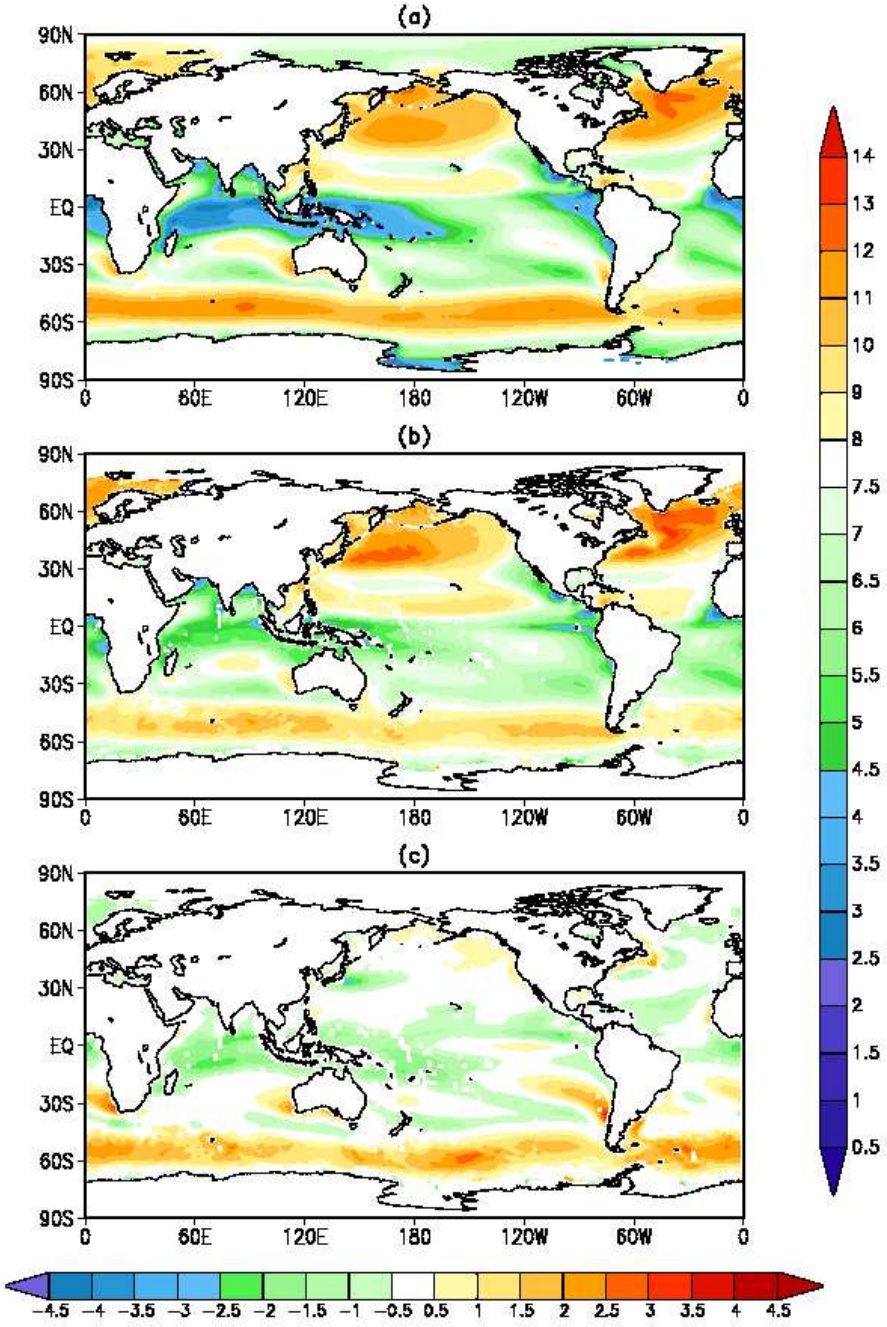

Figure 13: December-January-February Surface Wind Speed in m $\sec^{-1}$ from a) GEOS-5 AGCM b) GSSTF and c) the difference, GEOS-5 - GSSTF.

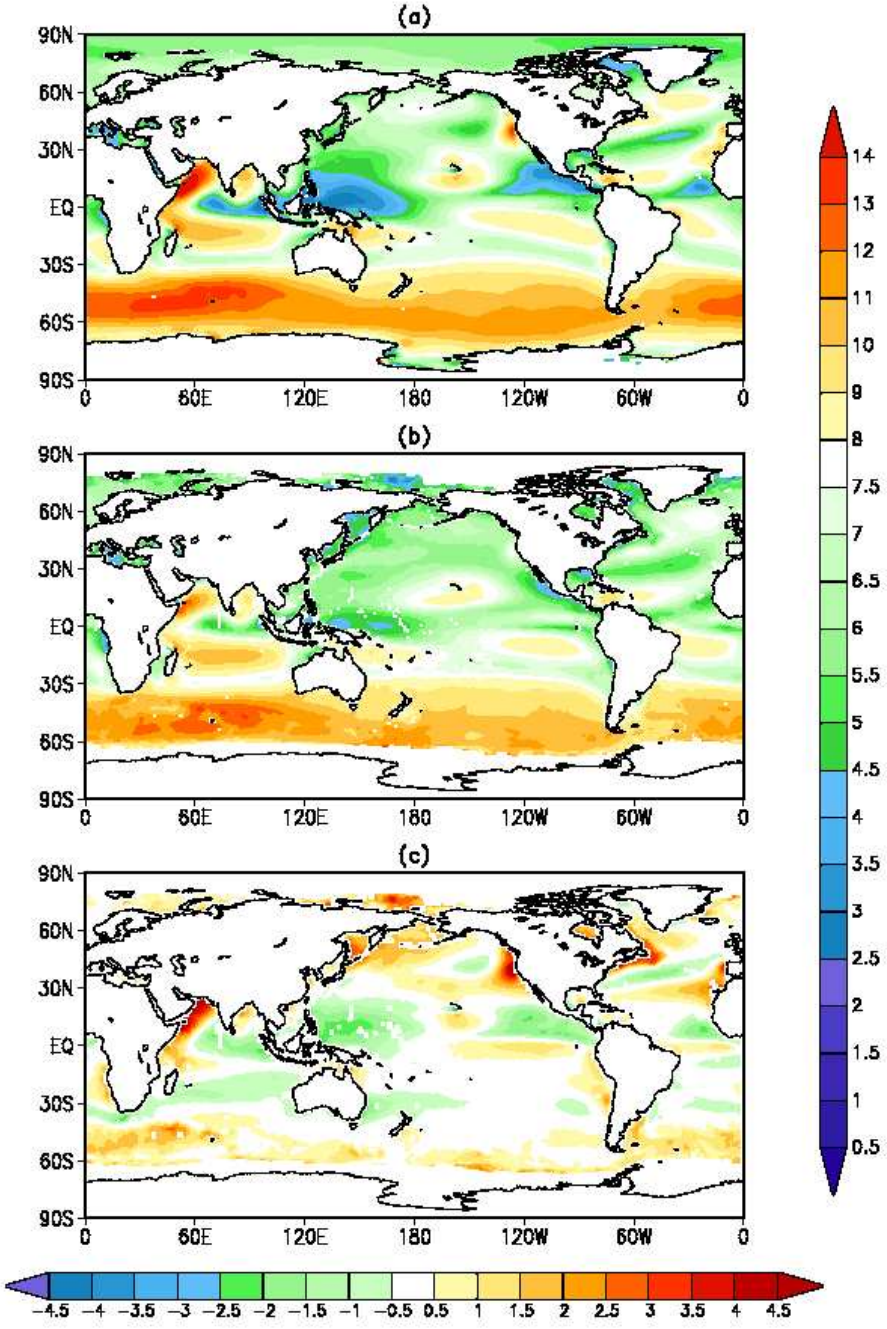

Figure 14: June-July-August Surface Wind Speed in m $\sec^{-1}$ from a) GEOS-5 AGCM b) GSSTF and c) the difference, GEOS-5 - GSSTF.

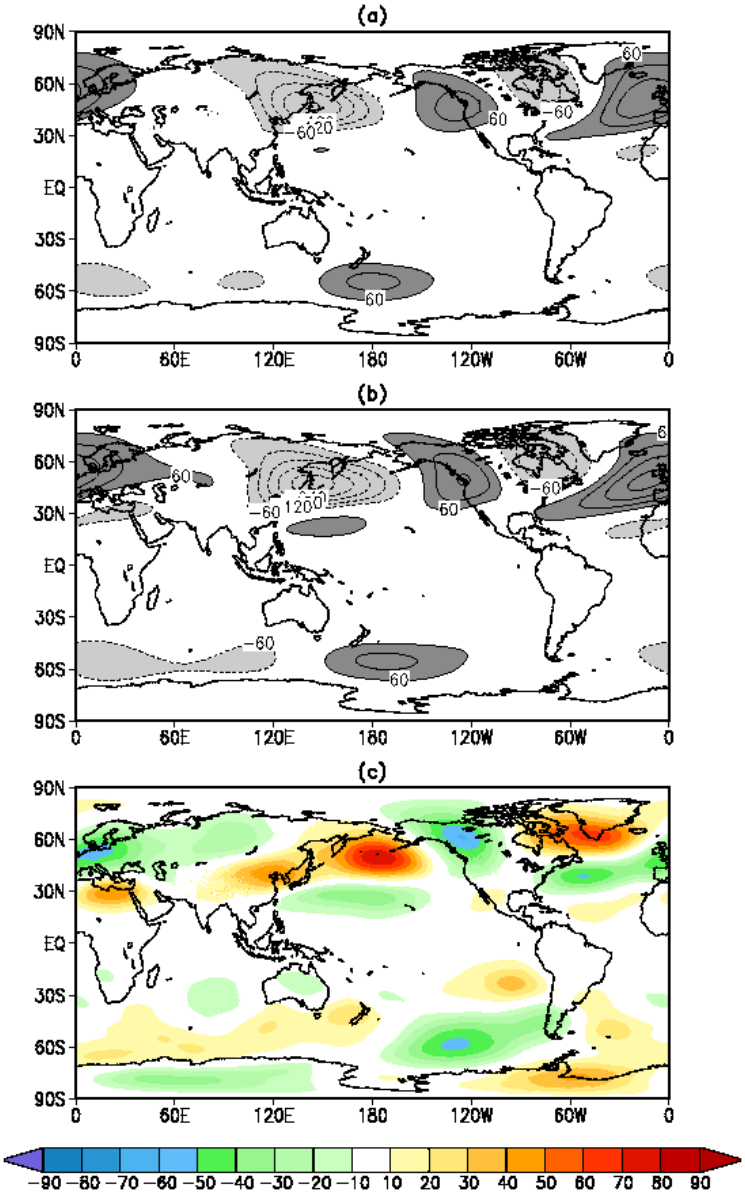

Figure 15: December-January-February 300 mb Eddy Height Climatology in m from a) GEOS-5 AGCM b) MERRA and c) the difference, GEOS-5 - MERRA.

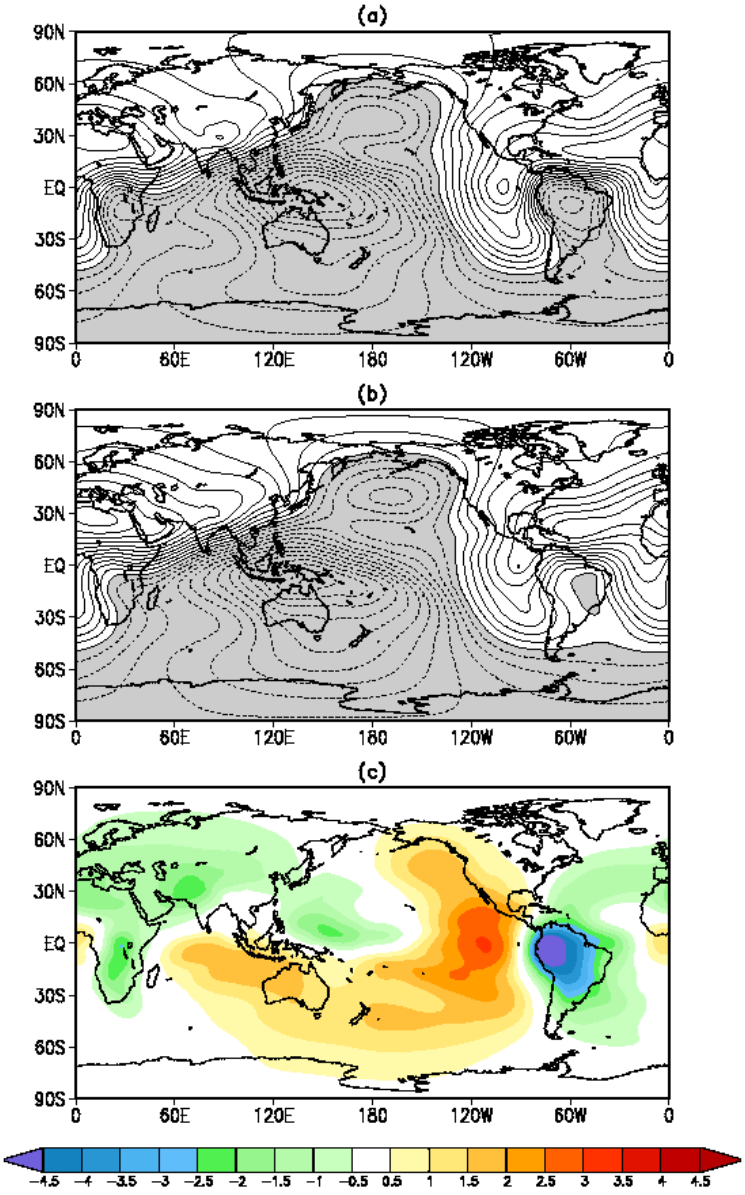

Figure 16: December-January-February 200 mb Velocity Potential Climatology in from a) GEOS-5 AGCM b) MERRA and c) the difference, GEOS-5 - MERRA.

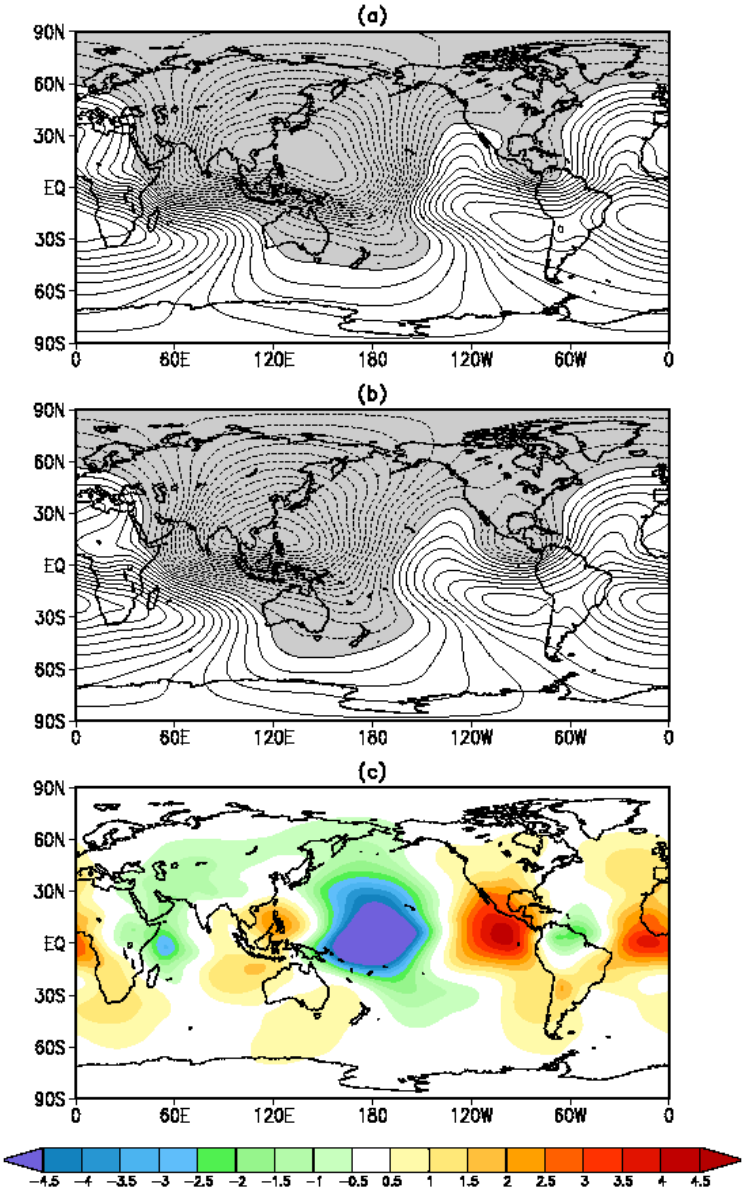

Figure 17: June-July-August 200 mb Velocity Potential Climatology in from a) GEOS-5 AGCM b) MERRA and c) the difference, GEOS-5 - MERRA.

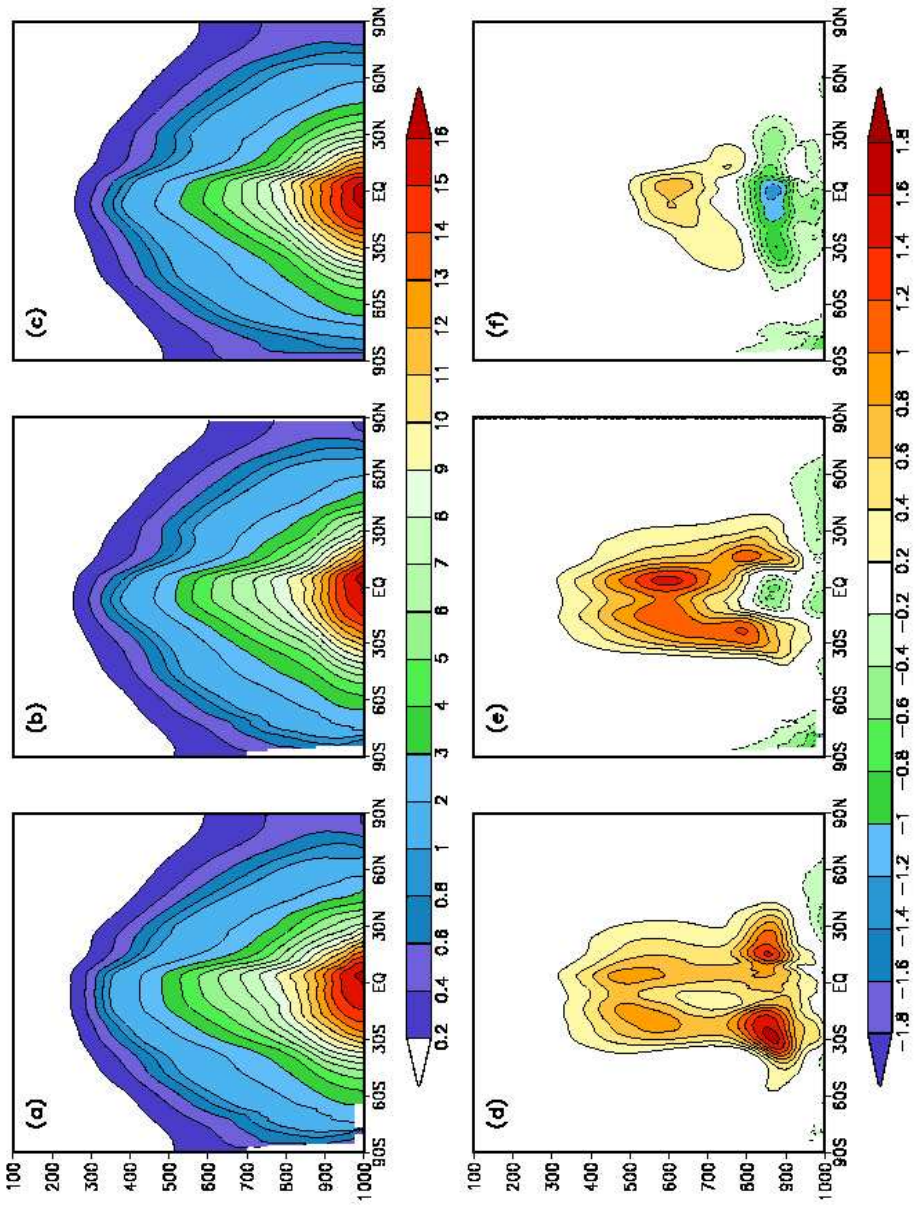

Figure 18: December-January-February Specific Humidity Climatology in g kg^{-1} a) from GEOS-5 AGCM, b) from MERRA Reanalysis, c) ECinterim reanalysis, d) GEOS-5 AGCM - MERRA, e) GEOS-5 AGCM - ECinterim, f) MERRA - ECinterim.

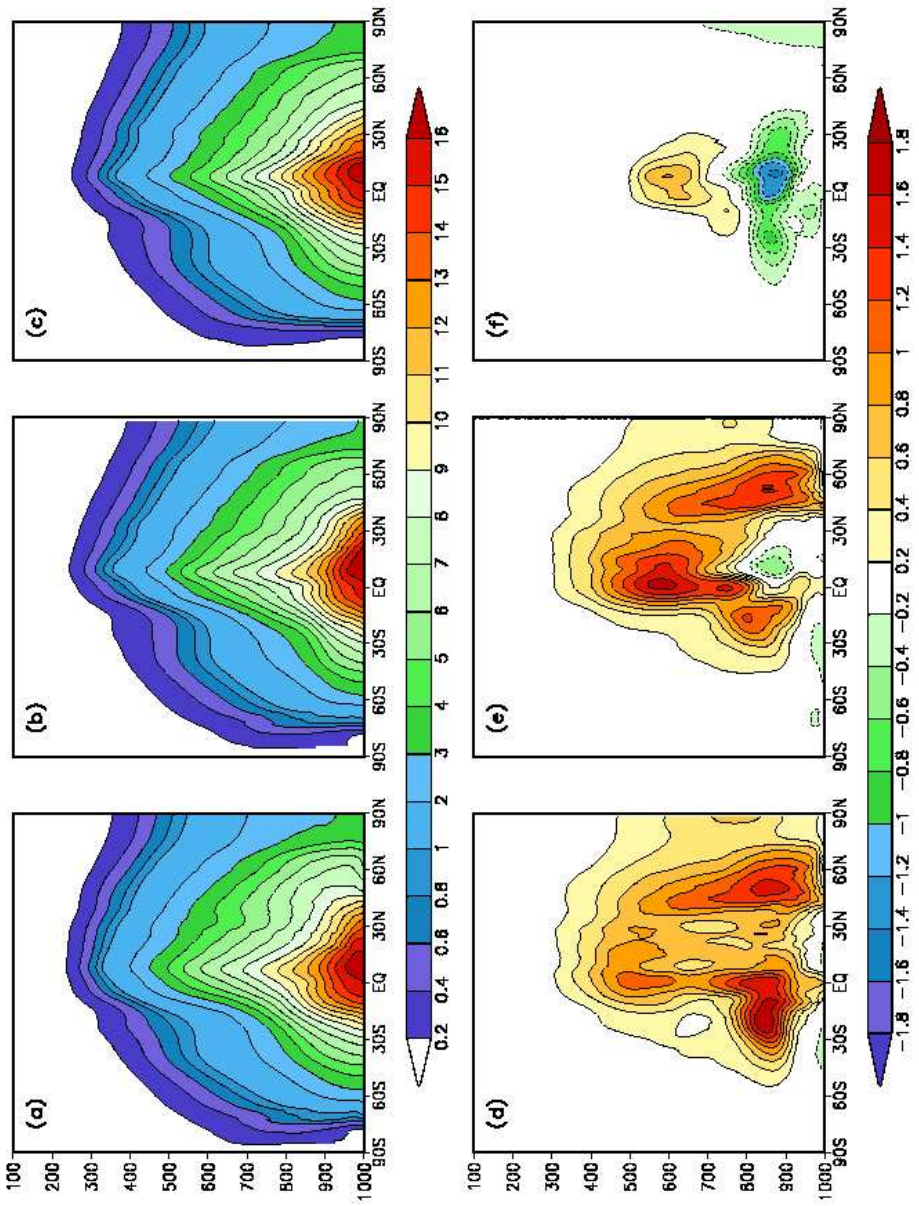

Figure 19: June-July-August Specific Humidity Climatology in g kg^{-1} a) from GEOS-5 AGCM, b) from MERRA Reanalysis, c) ECinterim reanalysis, d) GEOS-5 AGCM - MERRA, e) GEOS-5 AGCM - ECinterim, f) MERRA - ECinterim.

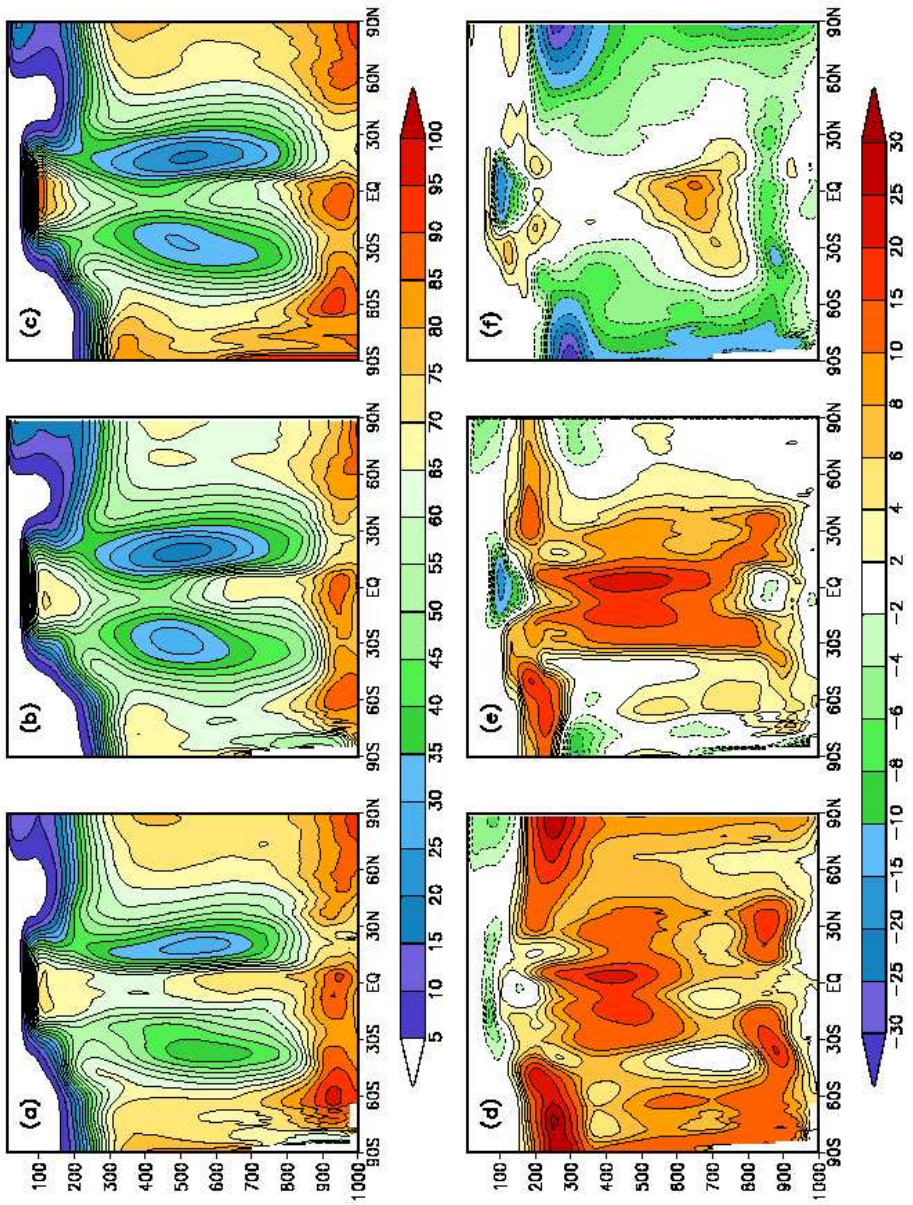

Figure 20: December-January-February Relative Humidity Climatology in percent a) from GEOS-5 AGCM, b) from MERRA Reanalysis, c) ECinterim reanalysis, d) GEOS-5 AGCM - MERRA, e) GEOS-5 AGCM - ECinterim, f) MERRA - ECinterim.

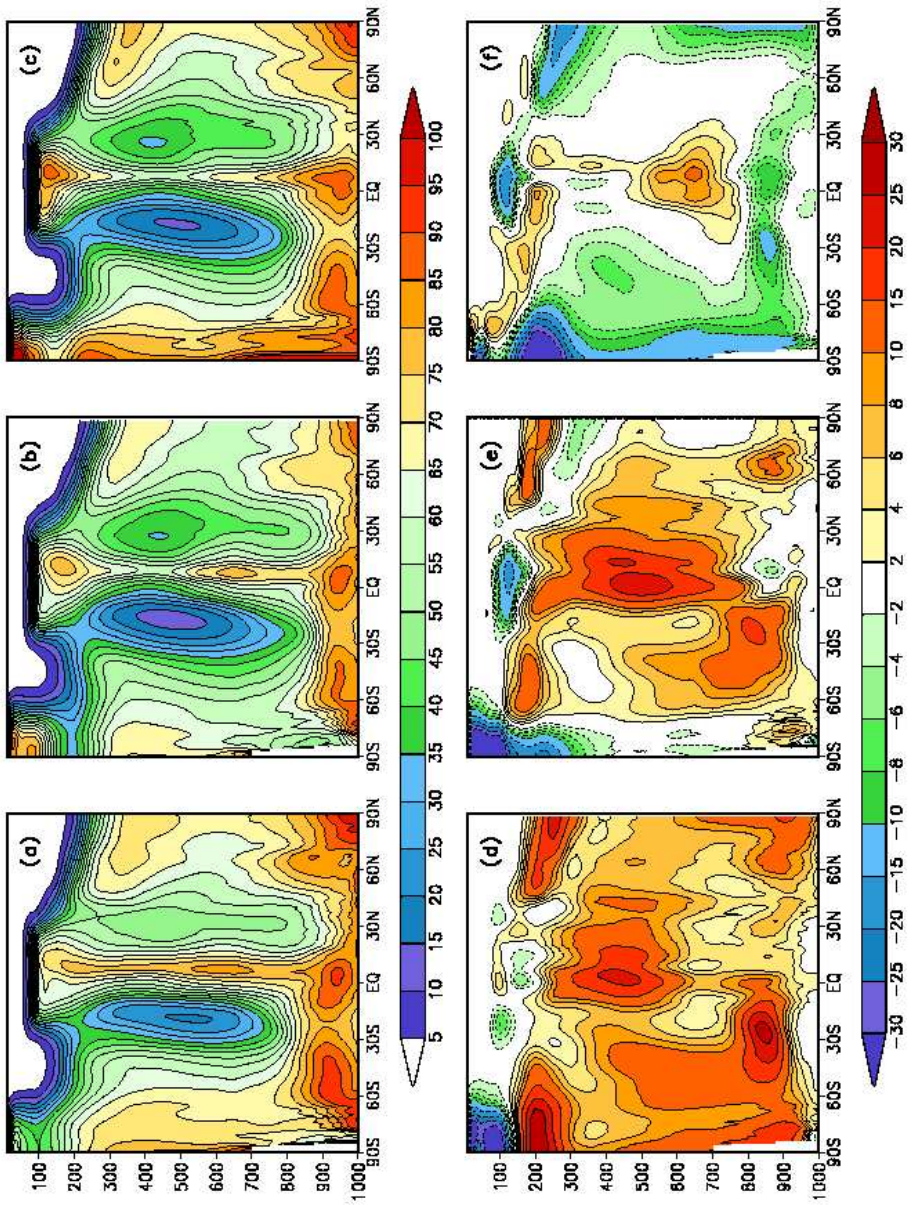

Figure 21: June-July-August Relative Humidity Climatology in percent a) from GEOS-5 AGCM, b) from MERRA Reanalysis, c) ECinterim reanalysis, d) GEOS-5 AGCM - MERRA, e) GEOS-5 AGCM - ECinterim, f) MERRA - ECinterim.

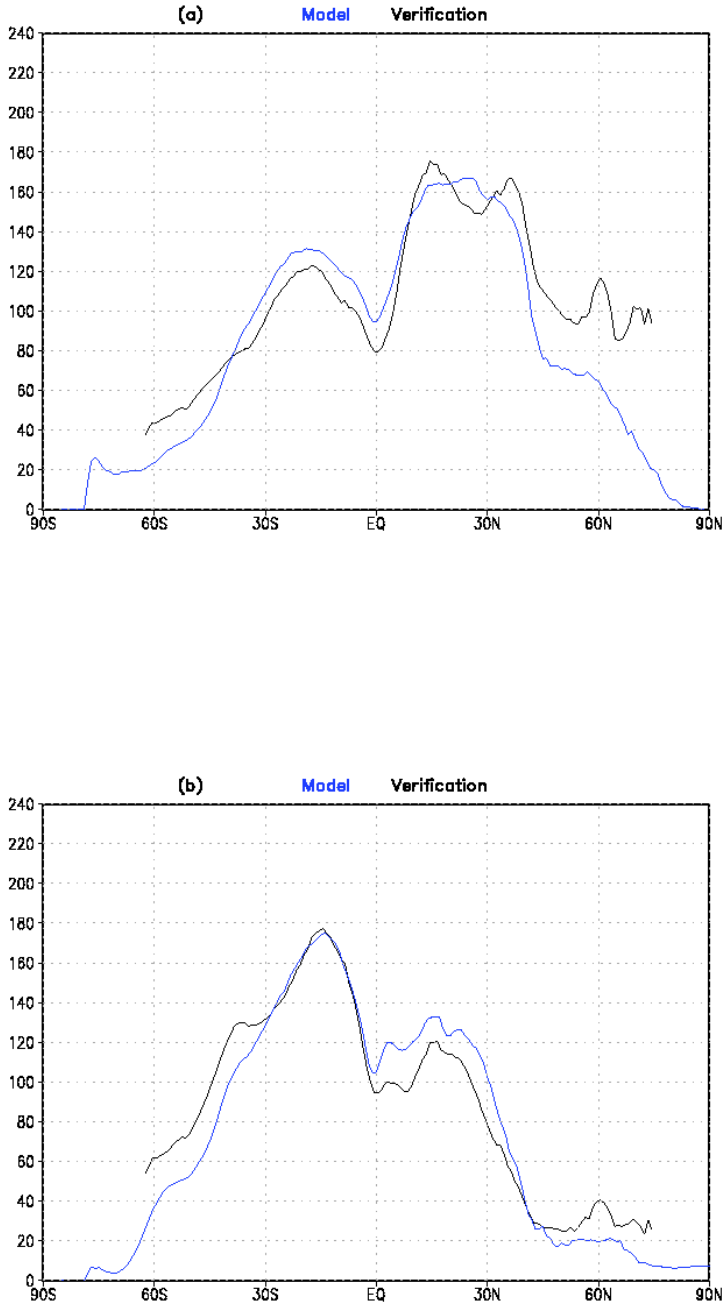

Figure 22: Oceans only zonal mean Latent Heat Flux W m^{-2} from GEOS-5 AGCM (blue) and GSSTF (black) during a) December-January-February and b) June-July-August.

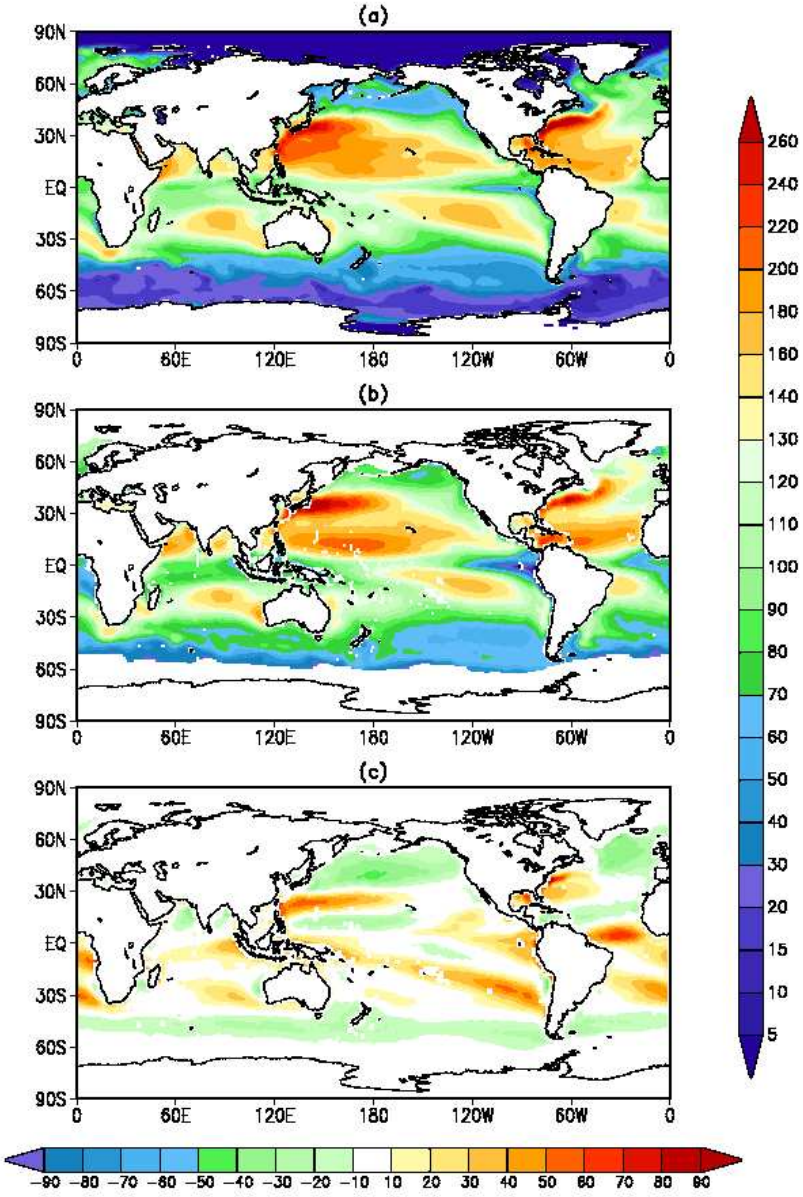

Figure 23: December-January-February Latent Heat Flux W m^{-2} from a) GEOS-5 AGCM b) GSSTF and c) the difference, GEOS-5 - GSSTF.

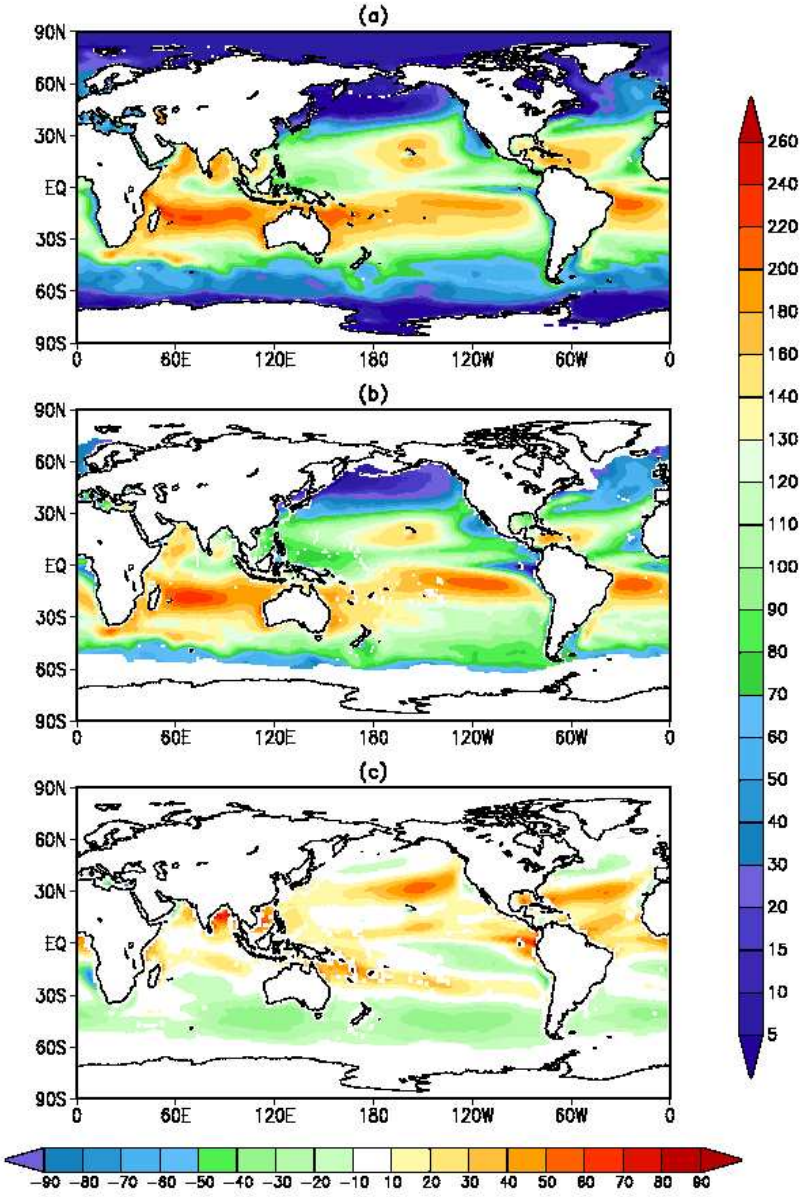

Figure 24: June-July-August Latent Heat Flux in W m^{-2} from a) GEOS-5 AGCM b) GSSTF and c) the difference, GEOS-5 - GSSTF.

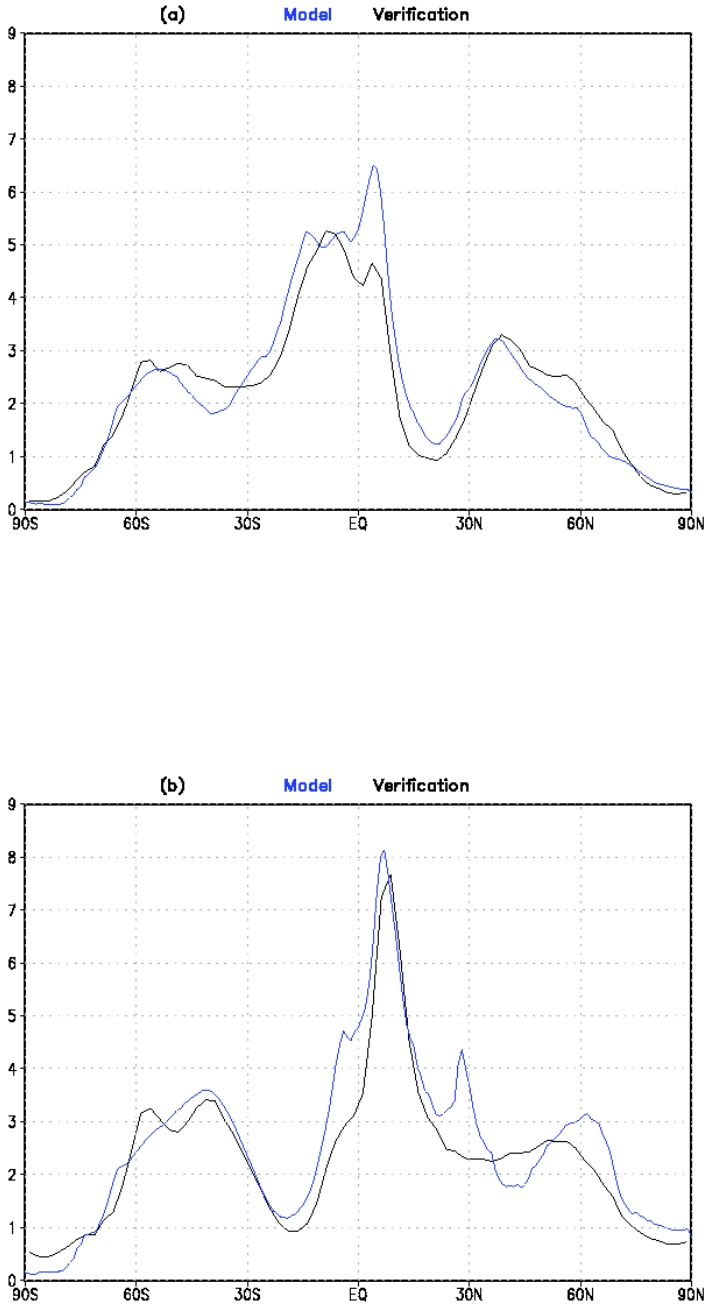

Figure 25: Zonal mean total precipitation in mm day^{-1} from GEOS-5 AGCM (blue) and GPCP (black) during a) December-January-February and b) June-July-August.

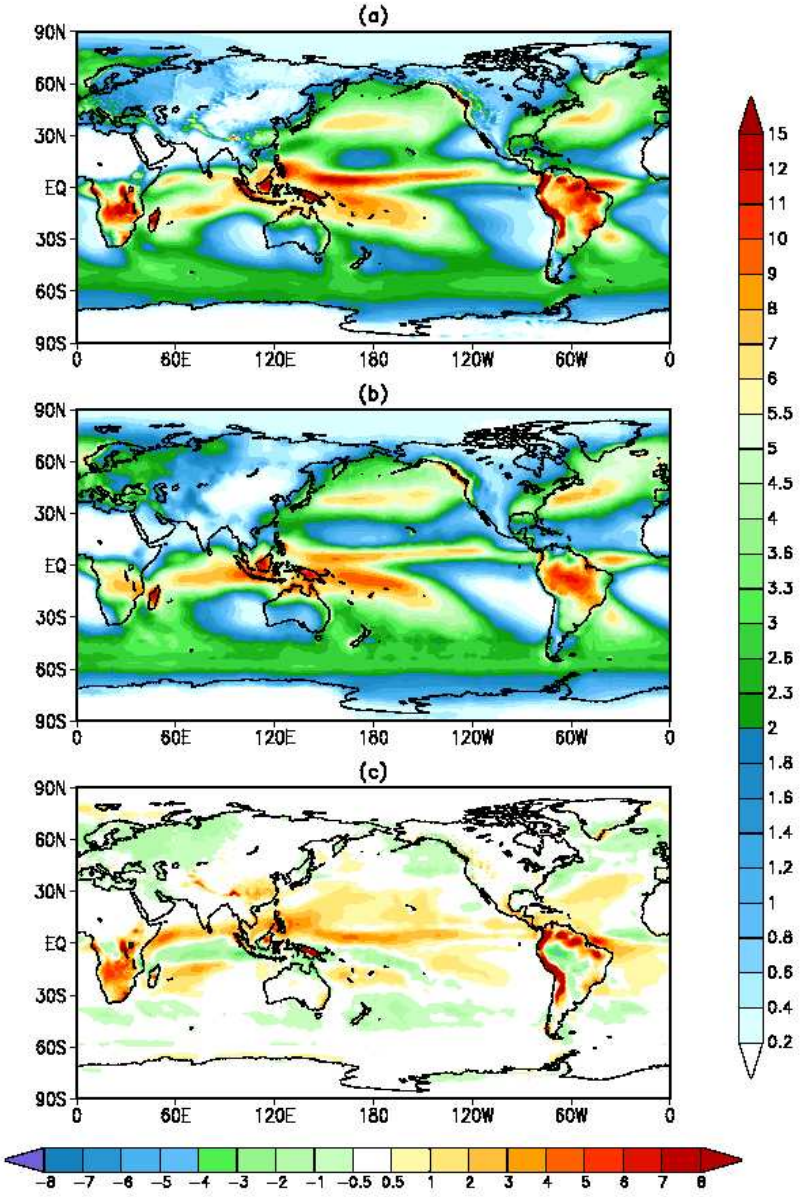

Figure 26: December-January-February Precipitation mm day^{-1} from a) GEOS-5 AGCM b) GPCP and c) the difference, GEOS-5 - GPCP.

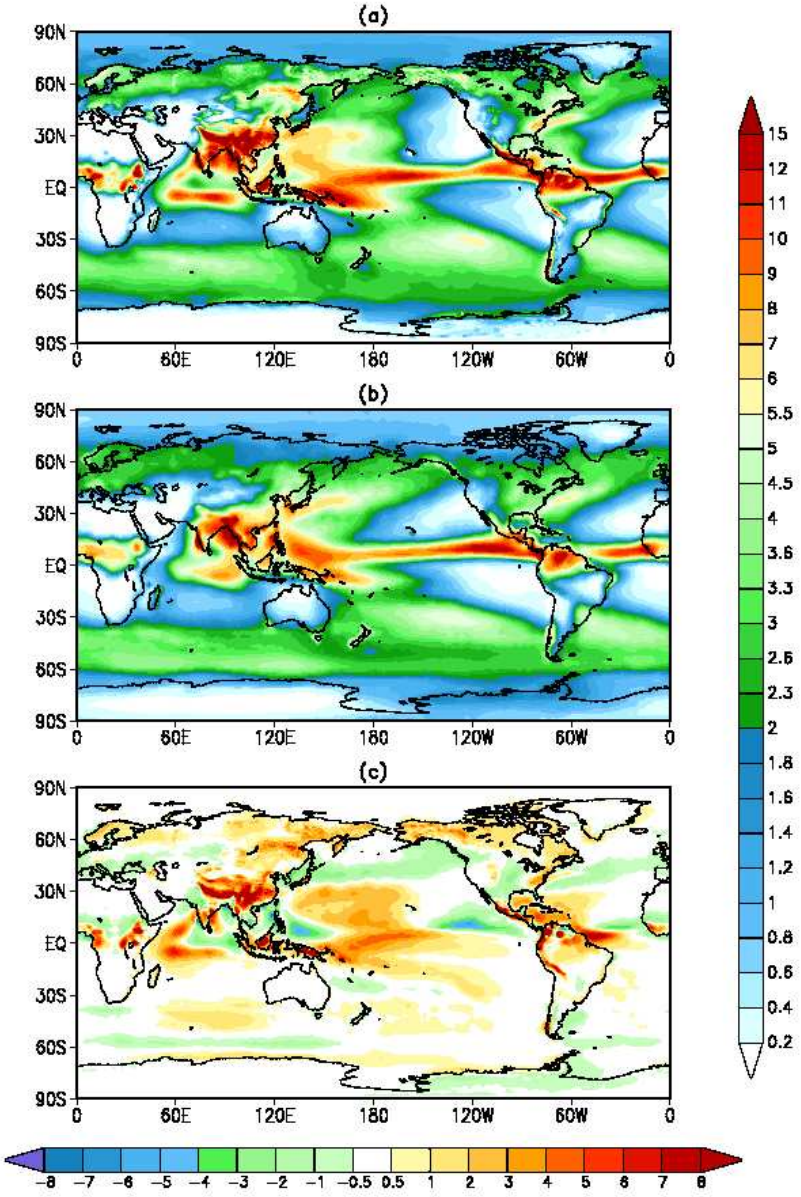

Figure 27: June-July-August Precipitation in mm day^{-1} from a) GEOS-5 AGCM b) GPCP and c) the difference, GEOS-5 - GPCP.

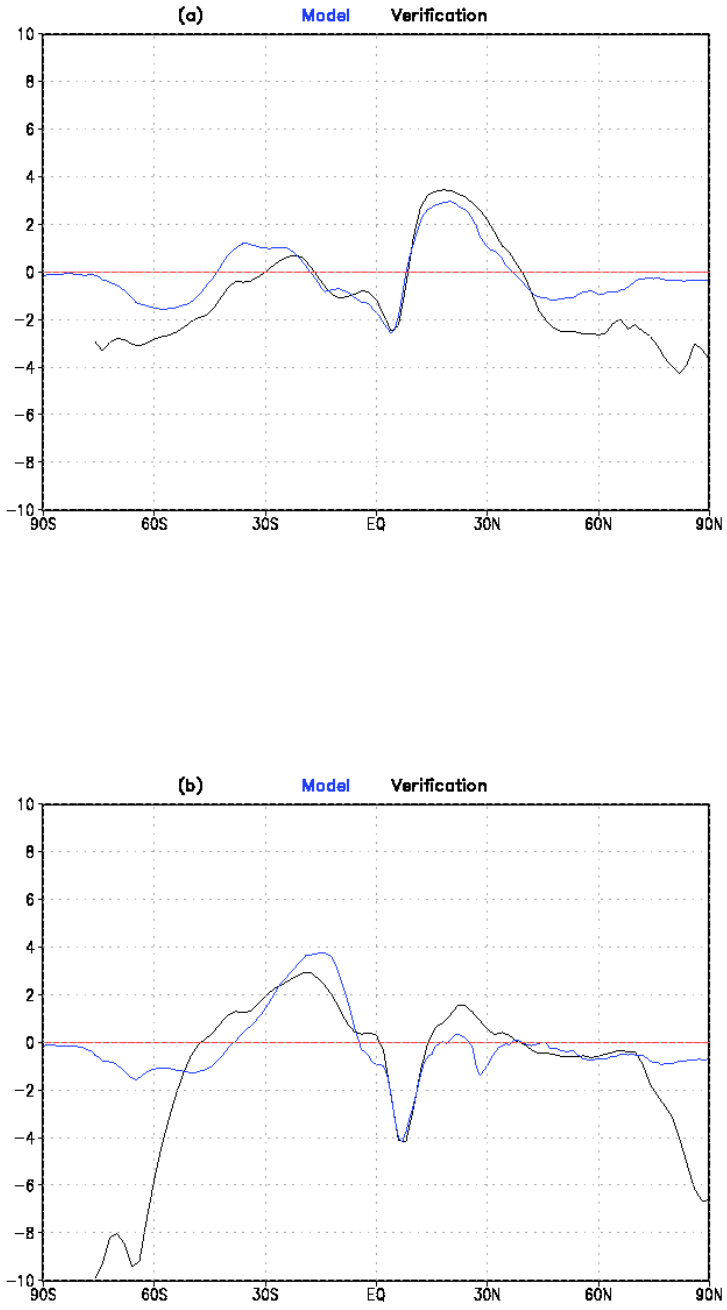

Figure 28: Oceans only zonal mean net humidity flux at the surface (Evaporation - Precipitation) mm day^{-1} from GEOS-5 AGCM (blue) and COADS (black) during a) December-January-February and b) June-July-August.

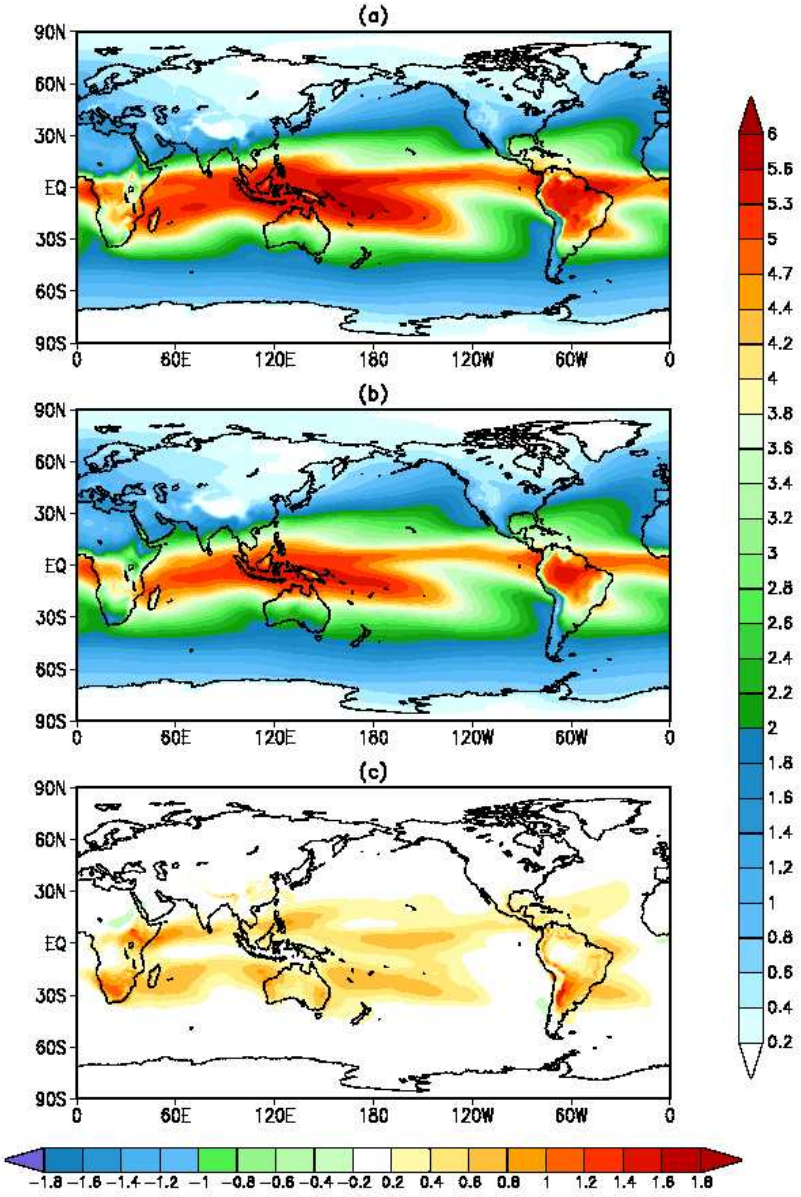

Figure 29: December-January-February Total Precipitable Water g cm^{-2} from a) GEOS-5 AGCM b) SRB and c) the difference, GEOS-5 - SRB.

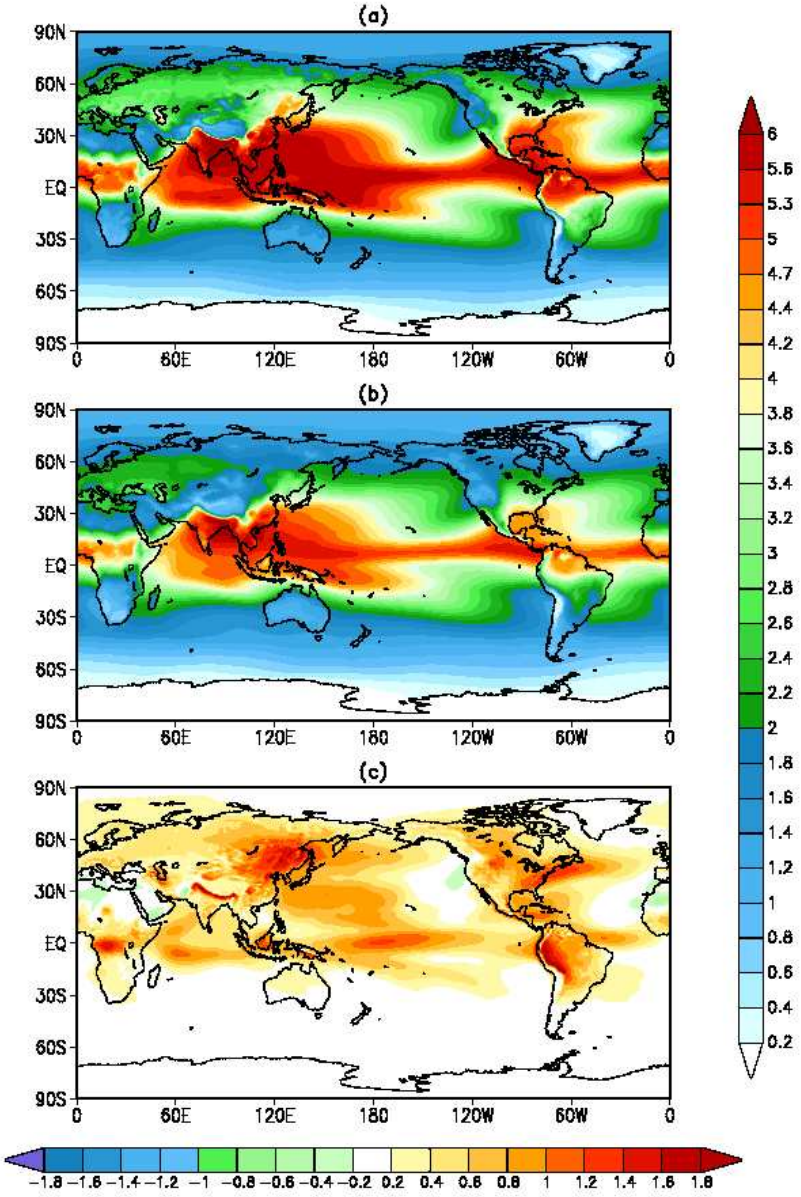

Figure 30: June-July-August Total Precipitable Water in g cm^{-2} from a) GEOS-5 AGCM b) SRB and c) the difference, GEOS-5 - SRB.

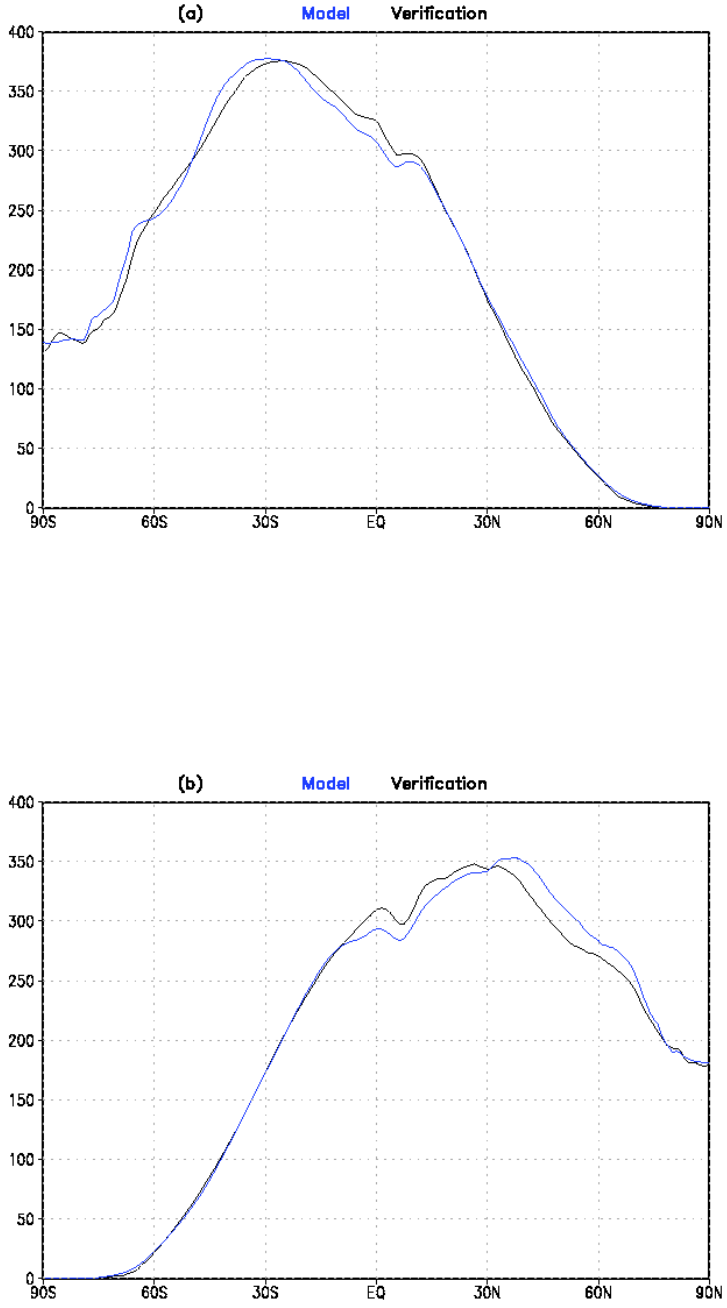

Figure 31: Zonal mean net shortwave radiation at the top of the atmosphere (incoming-outgoing) in W m^{-2} from GEOS-5 AGCM (blue) and CERES (black) during a) December-January-February and b) June-July-August.

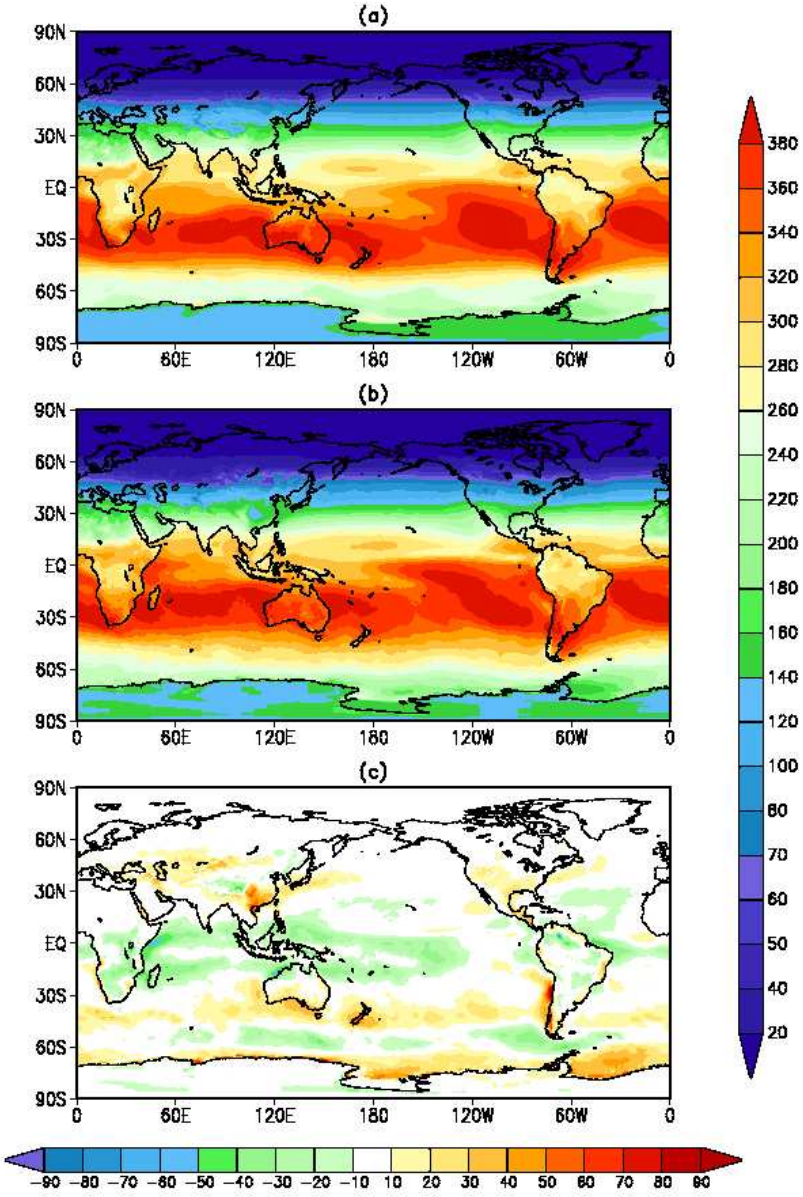

Figure 32: December-January-February net shortwave radiation at the top of the atmosphere in W m^{-2} from a) GEOS-5 AGCM b) CERES and c) the difference, GEOS-5 - CERES.

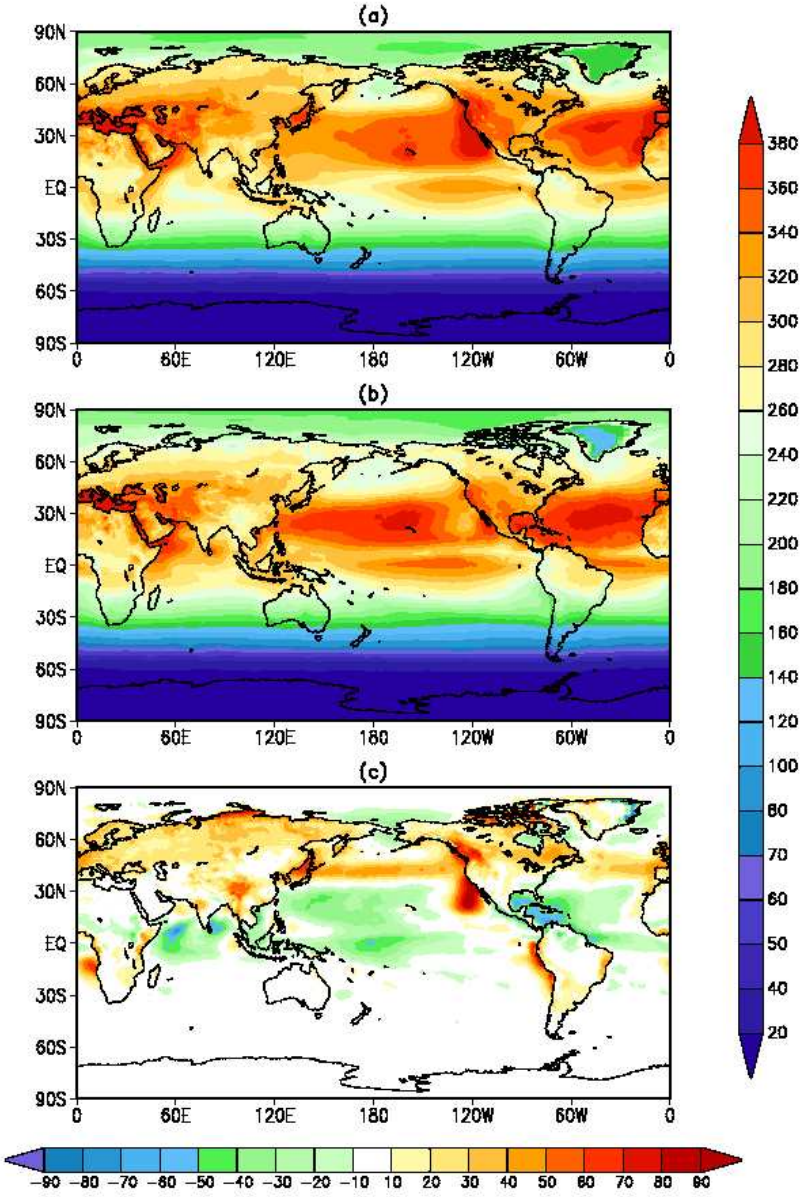

Figure 33: June-July-August net shortwave radiation at the top of the atmosphere in W m^{-2} from a) GEOS-5 AGCM b) CERES and c) the difference, GEOS-5 - CERES.

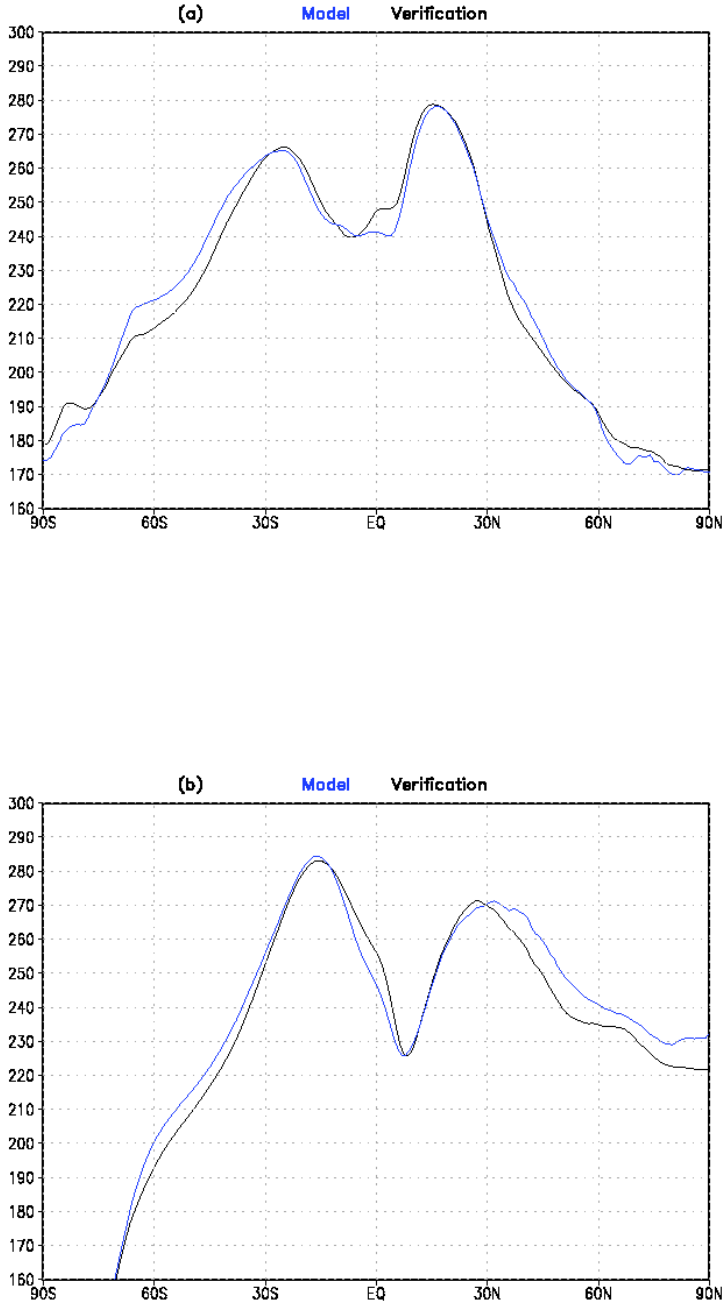

Figure 34: Zonal mean outgoing longwave radiation at the top of the atmosphere in W m^{-2} from GEOS-5 AGCM (blue) and CERES (black) during a) December-January-February and b) June-July-August.

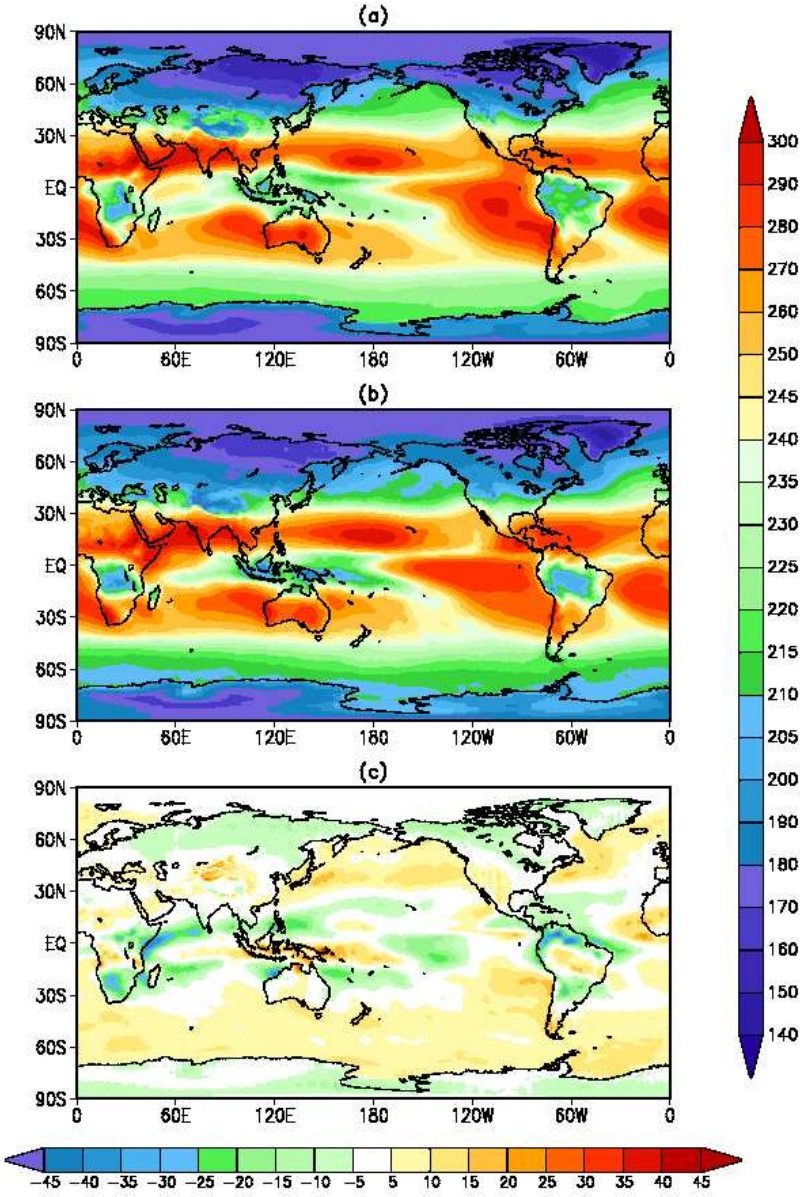

Figure 35: December-January-February outgoing longwave radiation at the top of the atmosphere in W m^{-2} from a) GEOS-5 AGCM b) CERES and c) the difference, GEOS-5 - CERES.

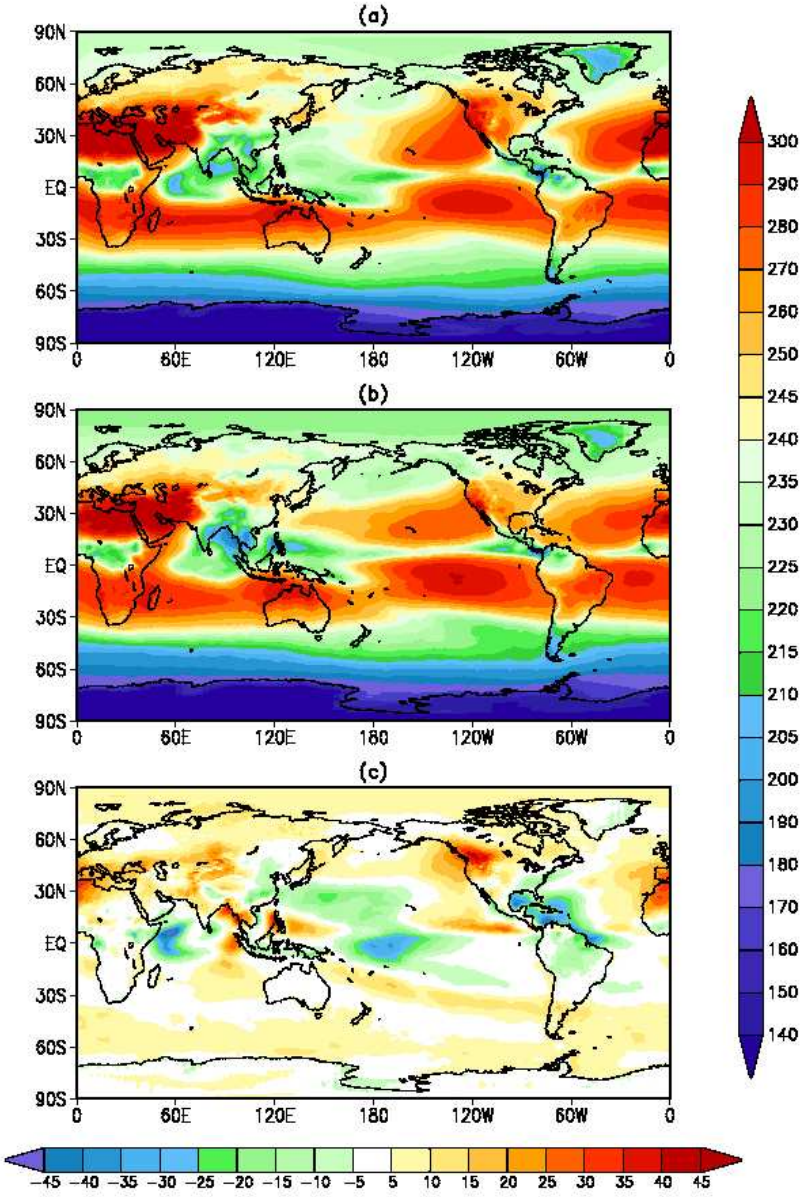

Figure 36: June-July-August outgoing longwave radiation at the top of the atmosphere in W m^{-2} from a) GEOS-5 AGCM b) CERES and c) the difference, GEOS-5 - CERES.

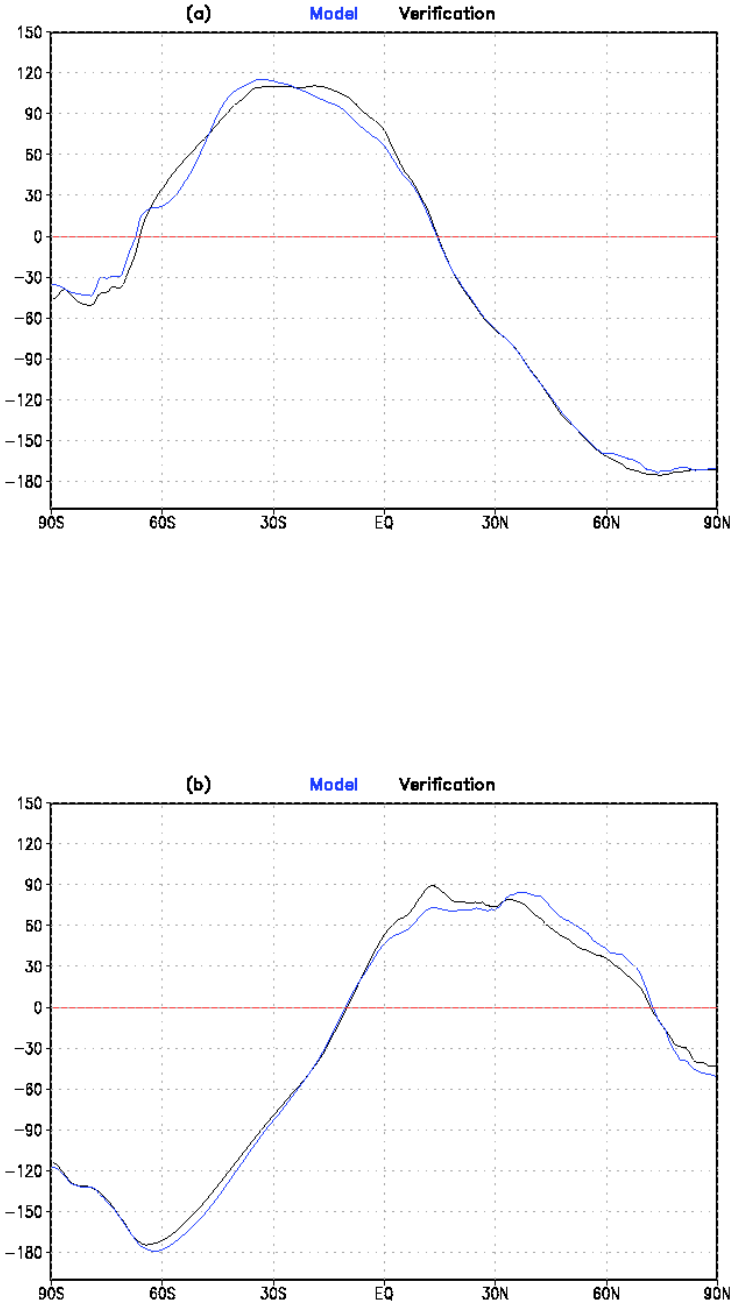

Figure 37: Zonal mean net radiation at the top of the atmosphere (incoming-outgoing) in W m^{-2} from GEOS-5 AGCM (blue) and CERES (black). during a) December-January-February and b) June-July-August.

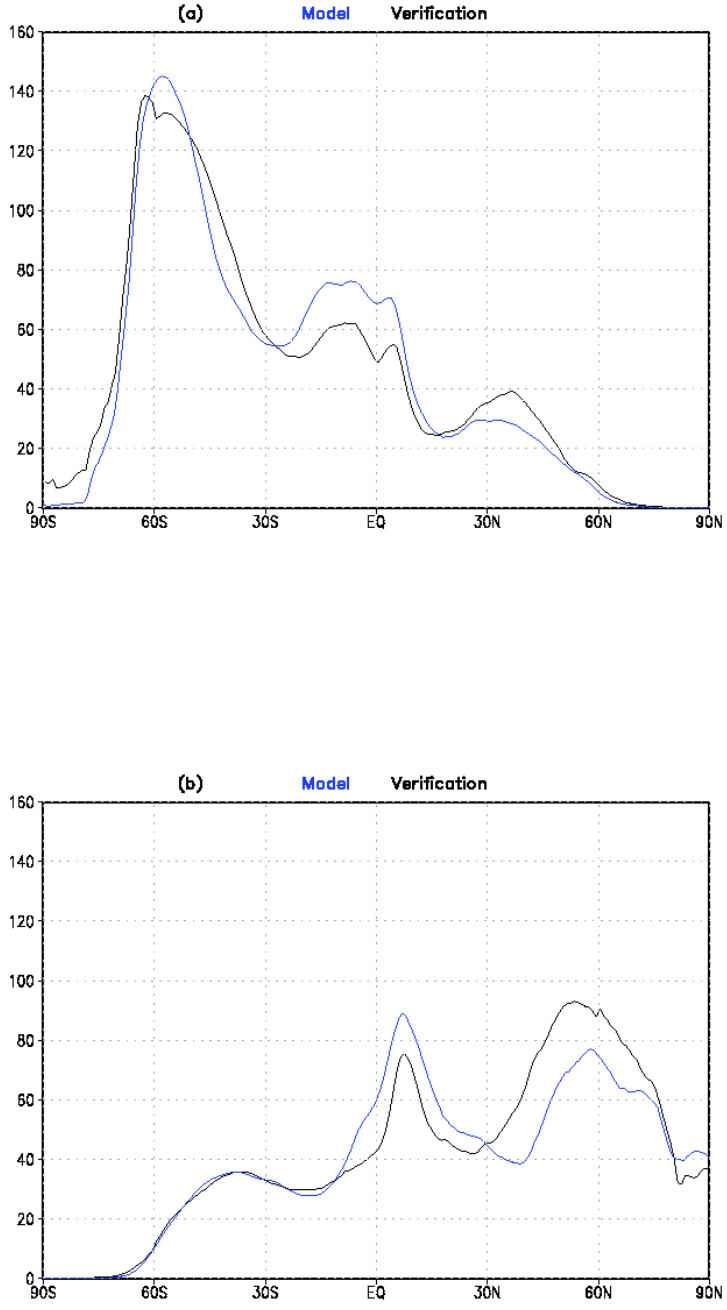

Figure 38: Zonal mean shortwave cloud radiative effect (outgoing shortwave - clear sky outgoing shortwave) at the top of the atmosphere in W m^{-2} from GEOS-5 AGCM (blue) and CERES (black) during a) December-January-February and b) June-July-August.

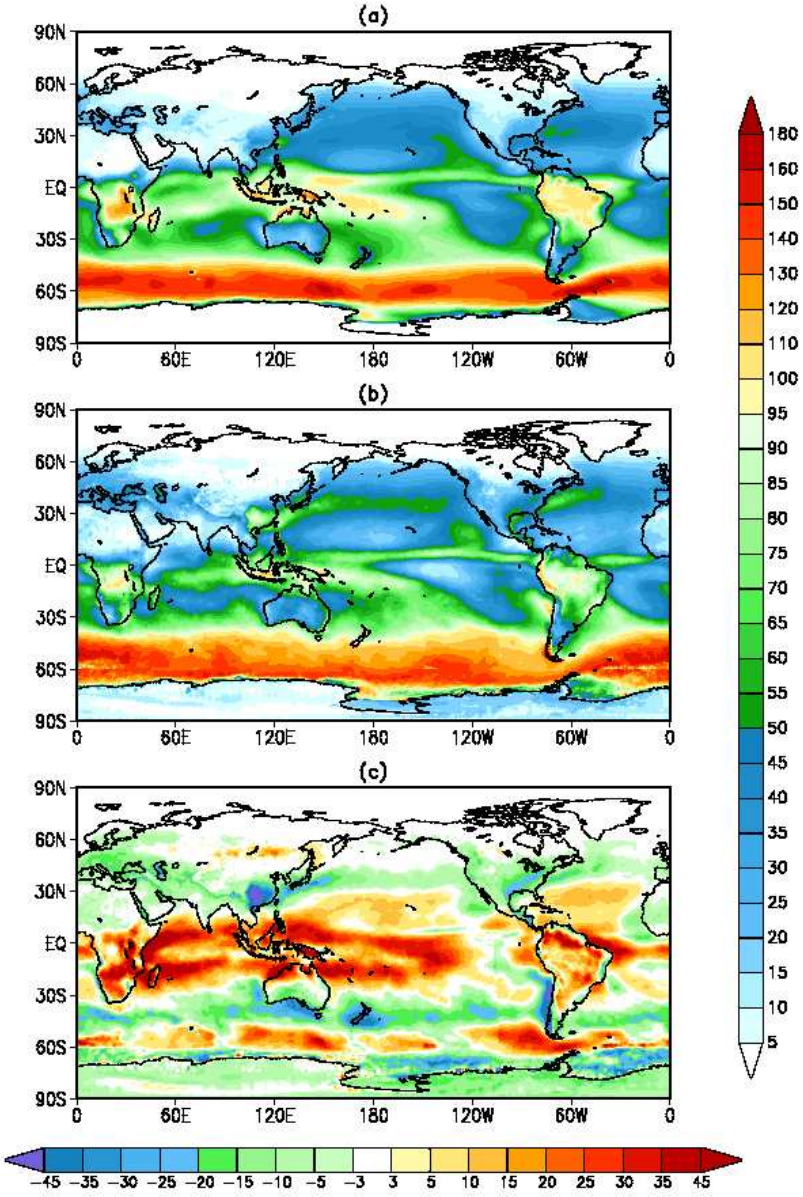

Figure 39: December-January-February shortwave cloud radiative effect (outgoing shortwave - clear sky outgoing shortwave) at the top of the atmosphere in W m^{-2} from a) GEOS-5 AGCM b) CERES and c) the difference, GEOS-5 - CERES.

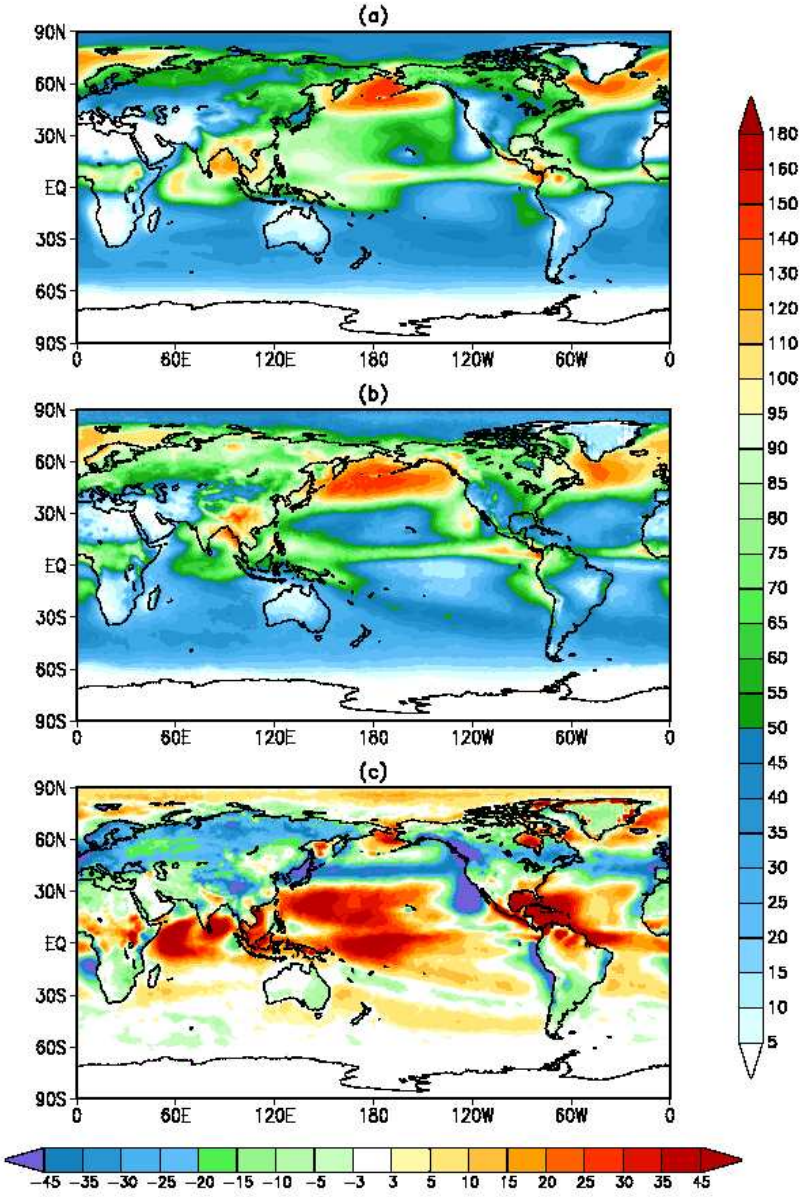

Figure 40: June-July-August shortwave shortwave cloud radiative effect (outgoing shortwave - clear sky outgoing shortwave) at the top of the atmosphere in W m^{-2} from a) GEOS-5 AGCM b) CERES and c) the difference, GEOS-5 - CERES.

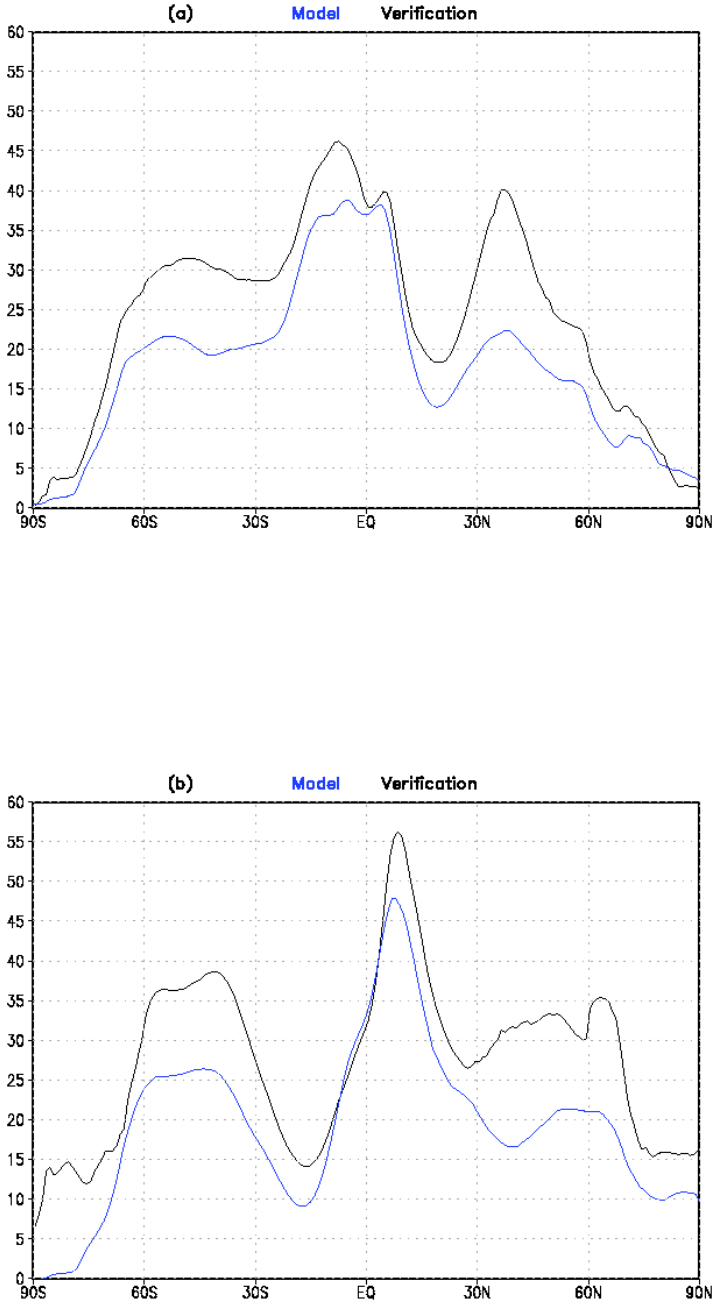

Figure 41: Zonal mean longwave cloud radiative effect (clear sky outgoing longwave - outgoing longwave) at the top of the atmosphere in W m^{-2} from GEOS-5 AGCM (blue) and CERES (black) during a) December-January-February and b) June-July-August.

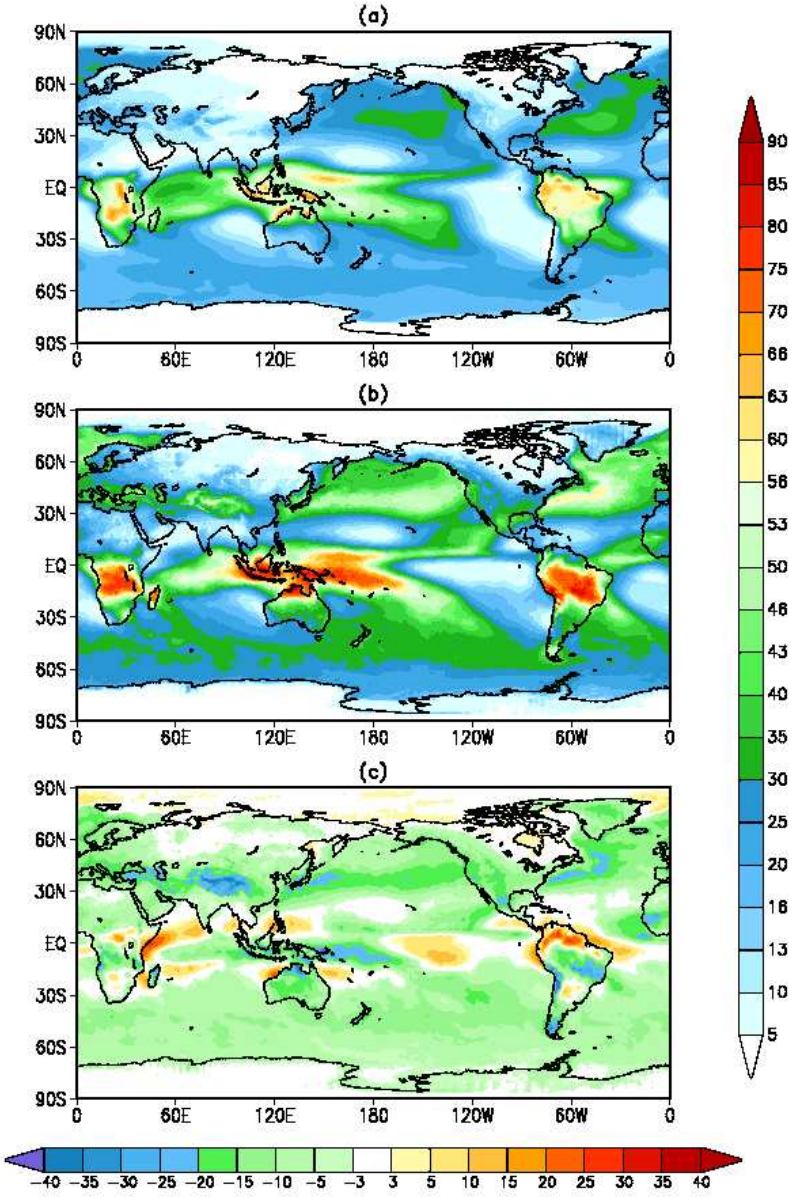

Figure 42: December-January-February longwave cloud radiative effect (clear sky outgoing longwave - outgoing longwave) at the top of the atmosphere in W m^{-2} from a) GEOS-5 AGCM b) CERES and c) the difference, GEOS-5 - CERES.

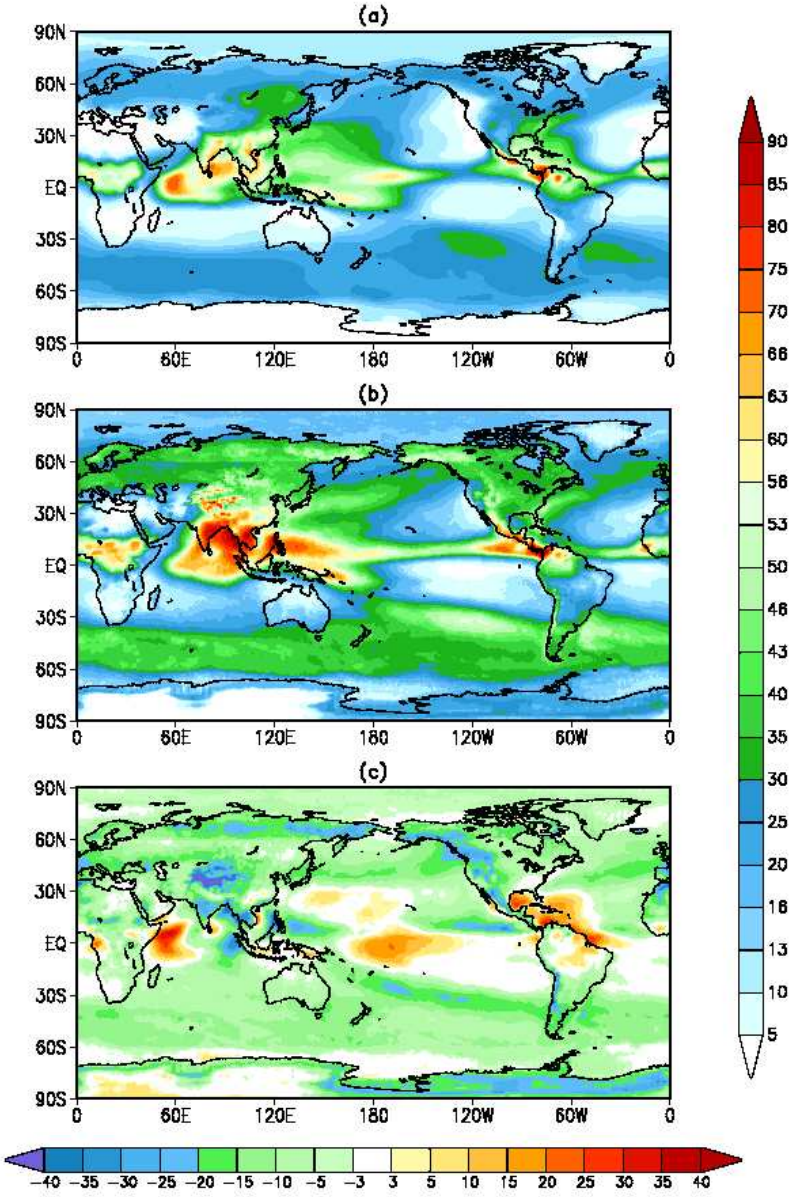

Figure 43: June-July-August longwave longwave cloud radiative effect (clear sky outgoing longwave - outgoing longwave) at the top of the atmosphere in W m^{-2} from a) GEOS-5 AGCM b) CERES and c) the difference, GEOS-5 - CERES.

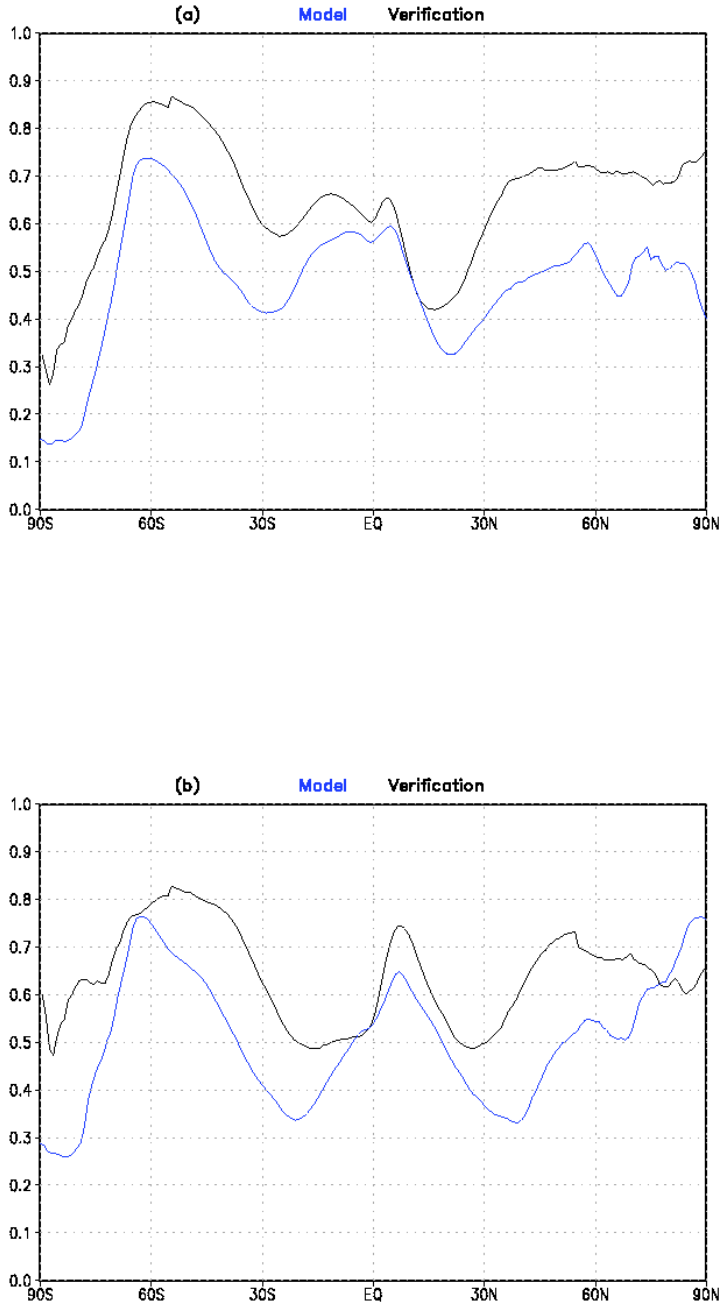

Figure 44: Zonal mean total cloud fraction from GEOS-5 AGCM (blue) and SRB (black) during a) December-January-February and b) June-July-August.

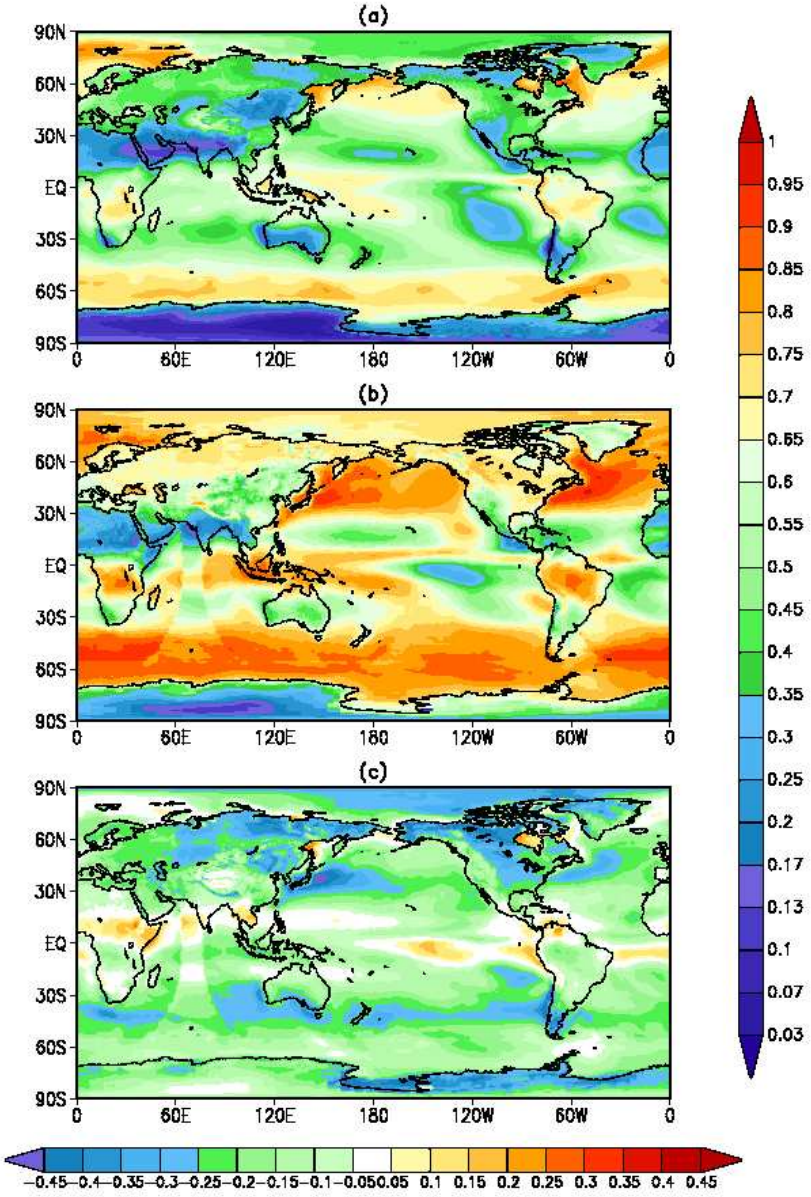

Figure 45: December-January-February total cloud fraction from a) GEOS-5 AGCM b) SRB and c) the difference, GEOS-5 - SRB.

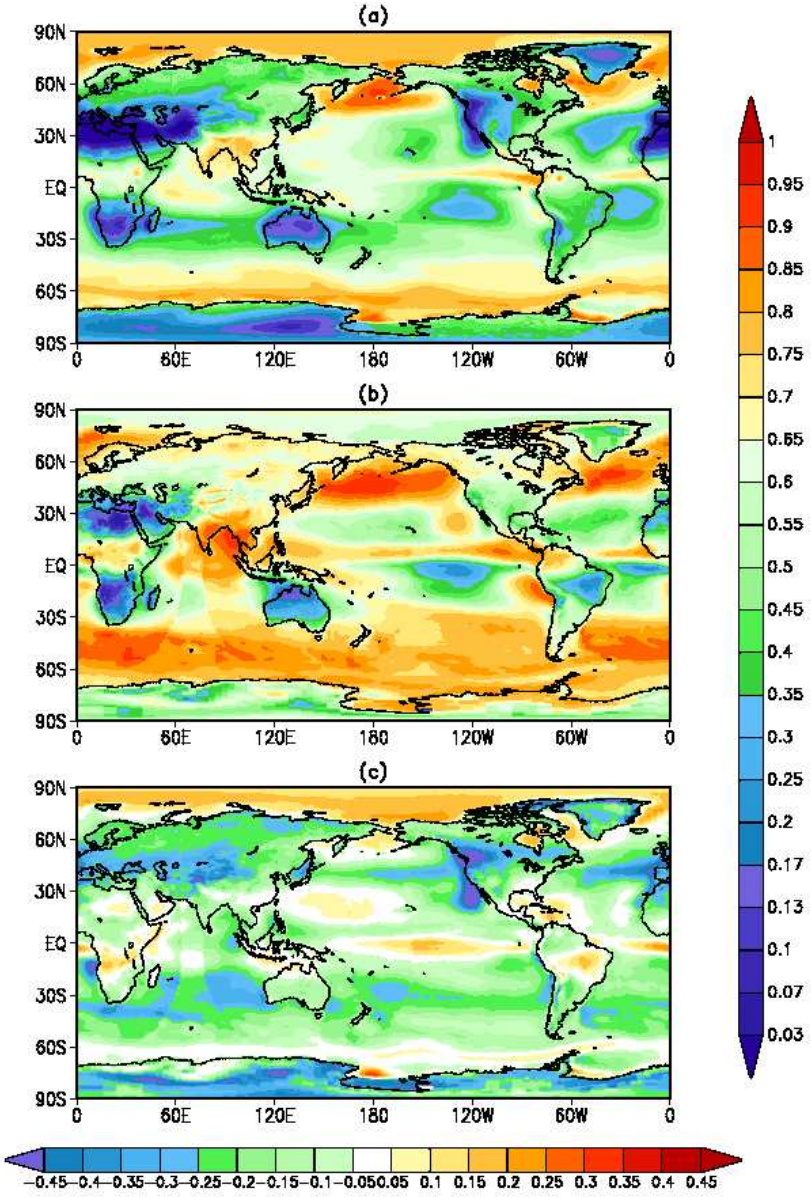

Figure 46: June-July-August total cloud fraction from a) GEOS-5 AGCM b) SRB and c) the difference, GEOS-5 - SRB.

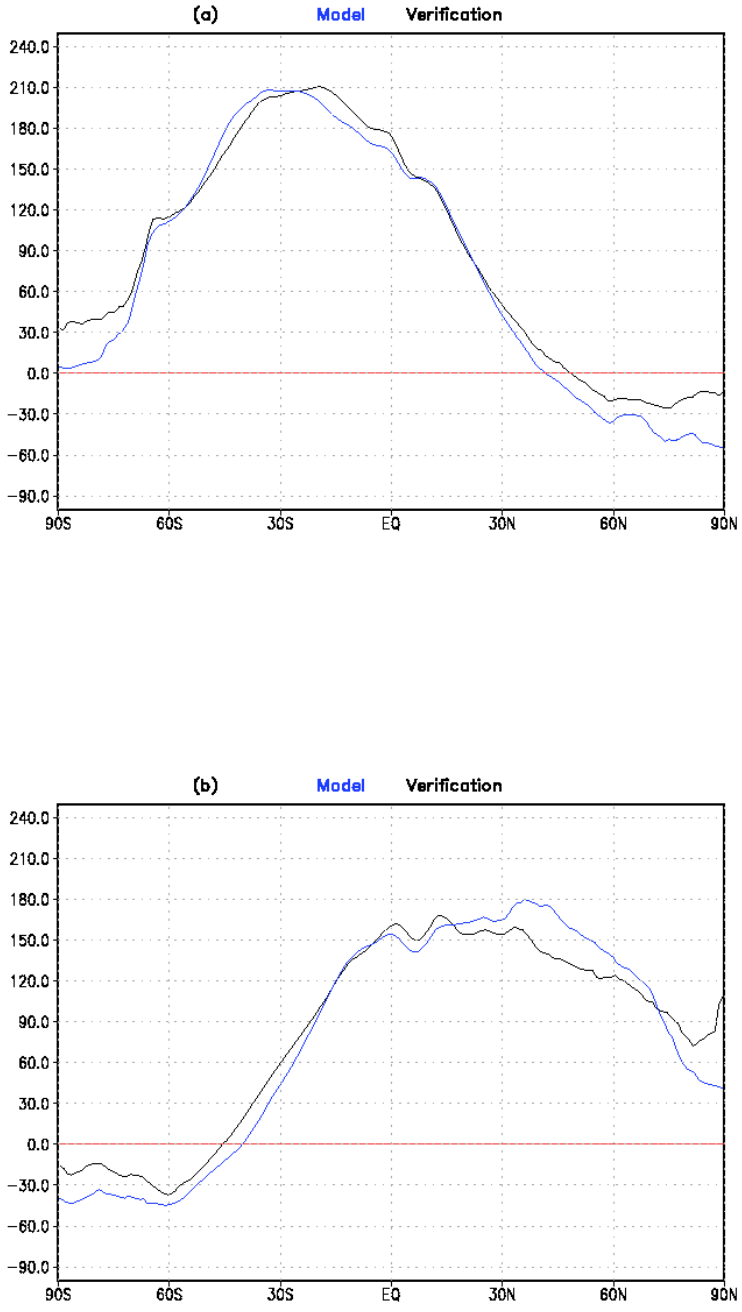

Figure 47: Zonal mean net radiation at the surface W m^{-2} from GEOS-5 AGCM (blue) and SRB (black) during a) December-January-February and b) June-July-August.

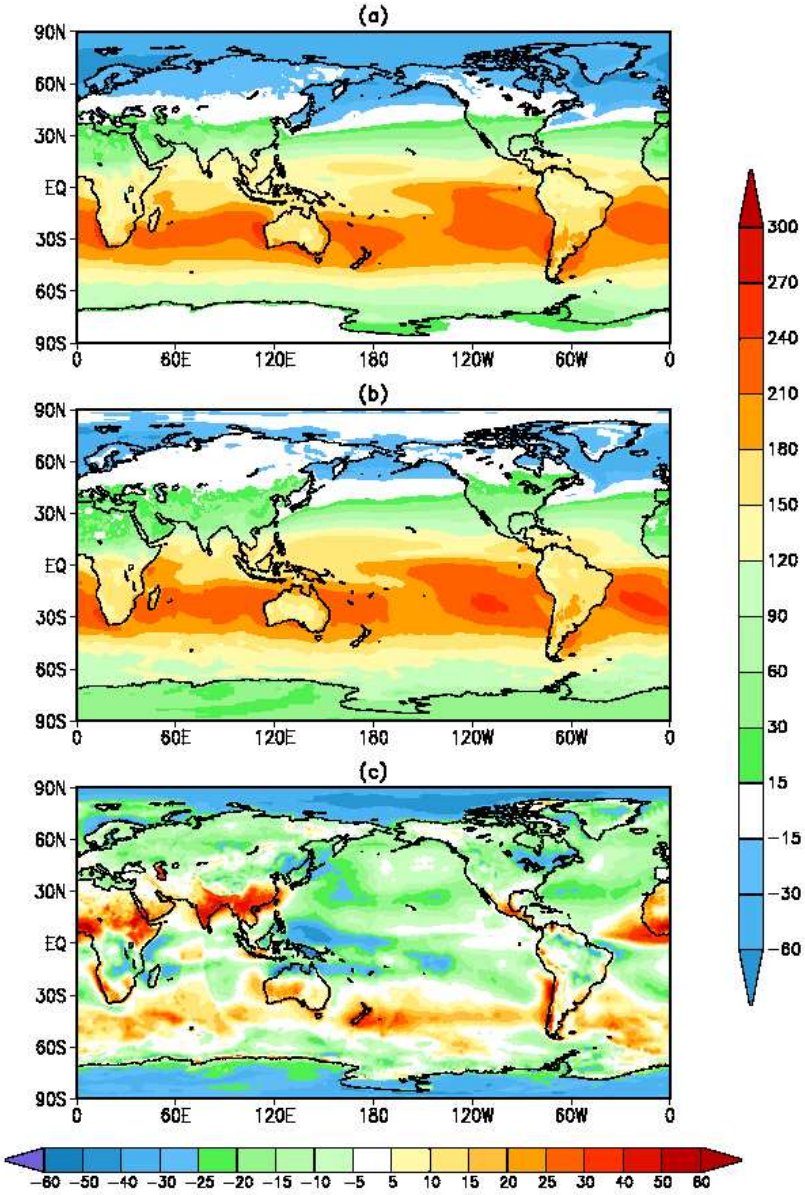

Figure 48: December-January-February net radiation at the surface in W m^{-2} from a) GEOS-5 AGCM b) SRB and c) the difference, GEOS-5 - SRB.

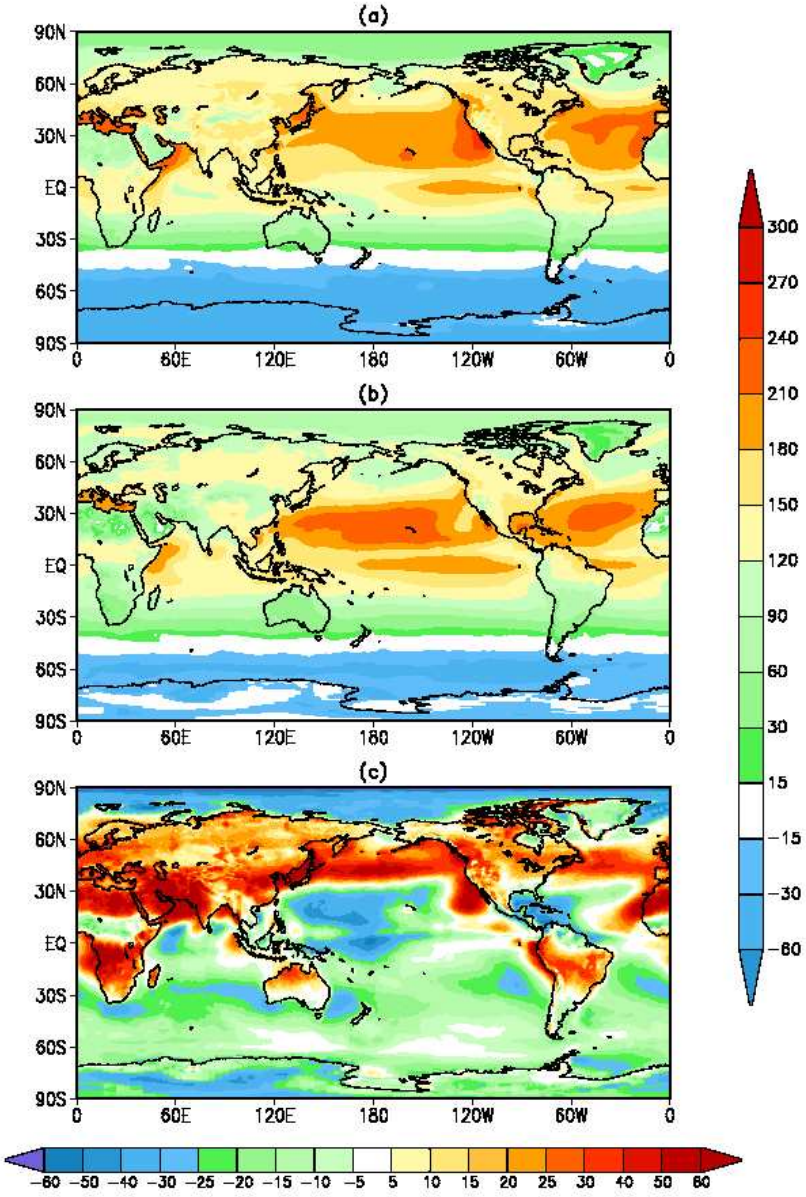

Figure 49: June-July-August net radiation at the surface in W m^{-2} from a) GEOS-5 AGCM b) SRB and c) the difference, GEOS-5 - SRB.

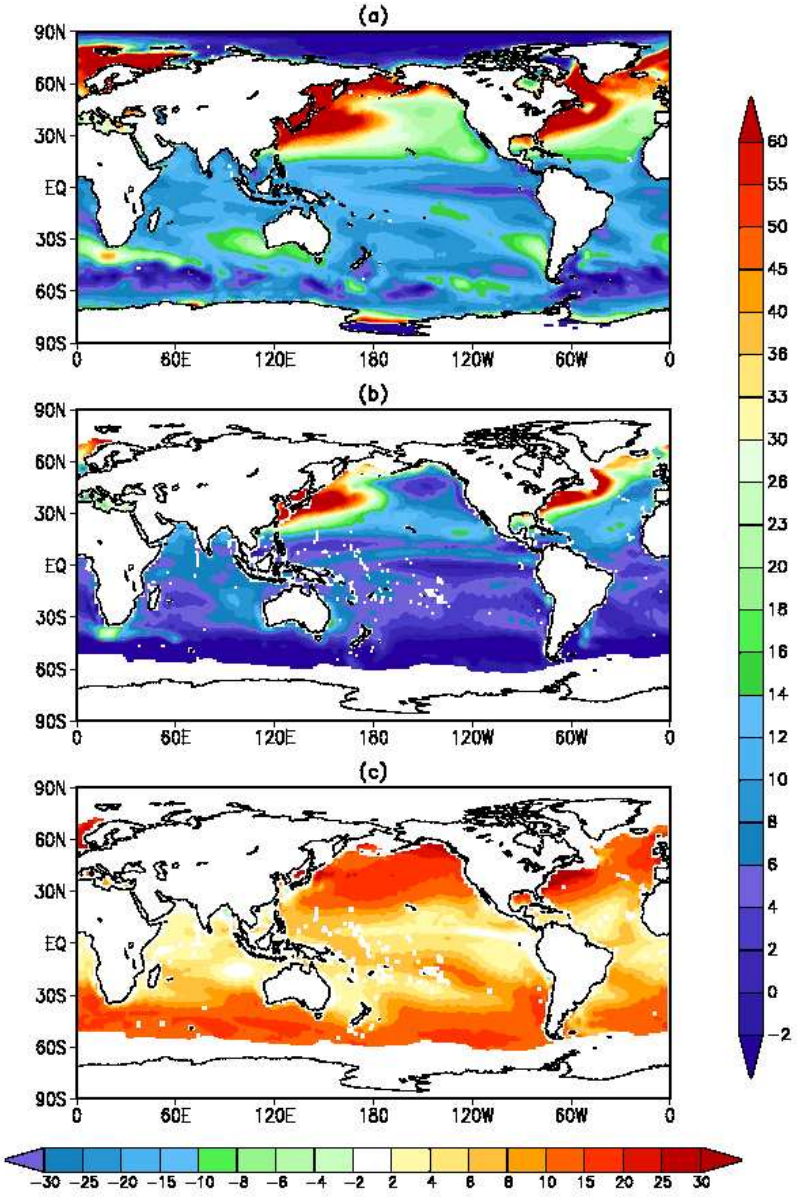

Figure 50: December-January-February Sensible Heat Flux W m^{-2} from a) GEOS-5 AGCM b) GSSTF and c) the difference, GEOS-5 - GSSTF.

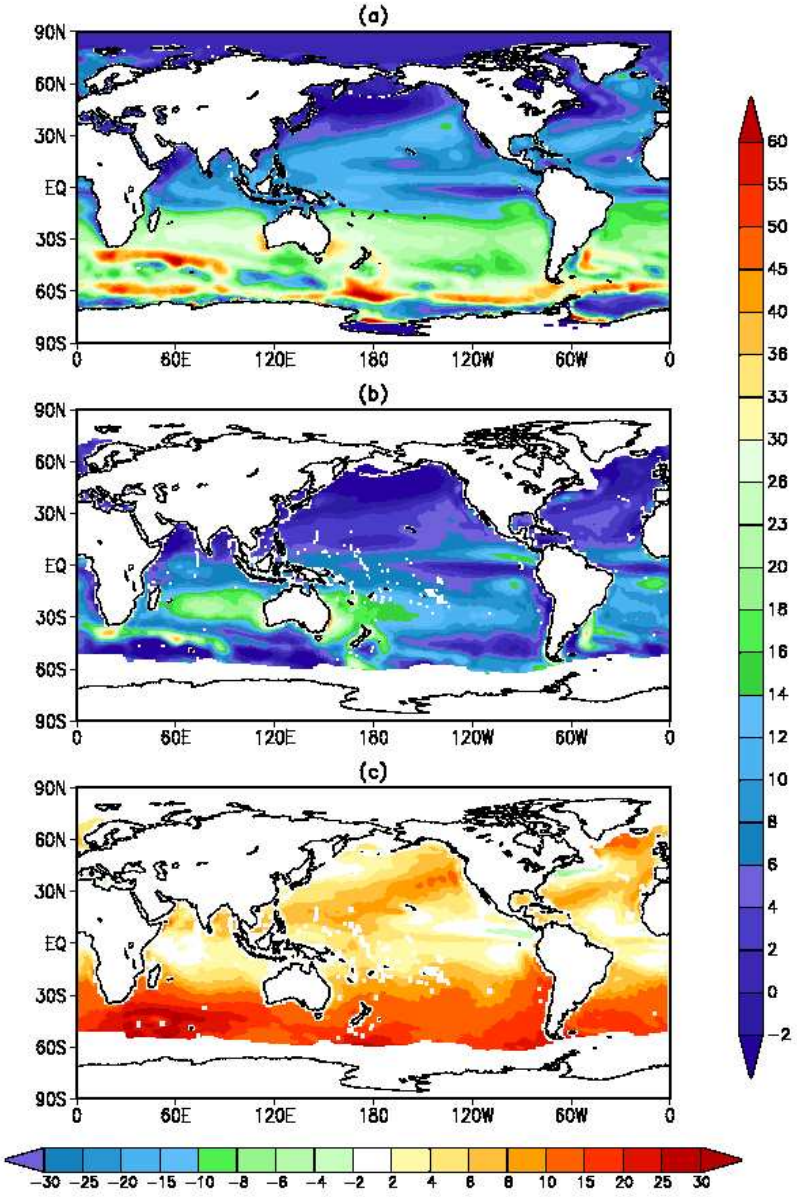

Figure 51: June-July-August Sensible Heat Flux in W m^{-2} from a) GEOS-5 AGCM b) GSSTF and c) the difference, GEOS-5 - GSSTF.

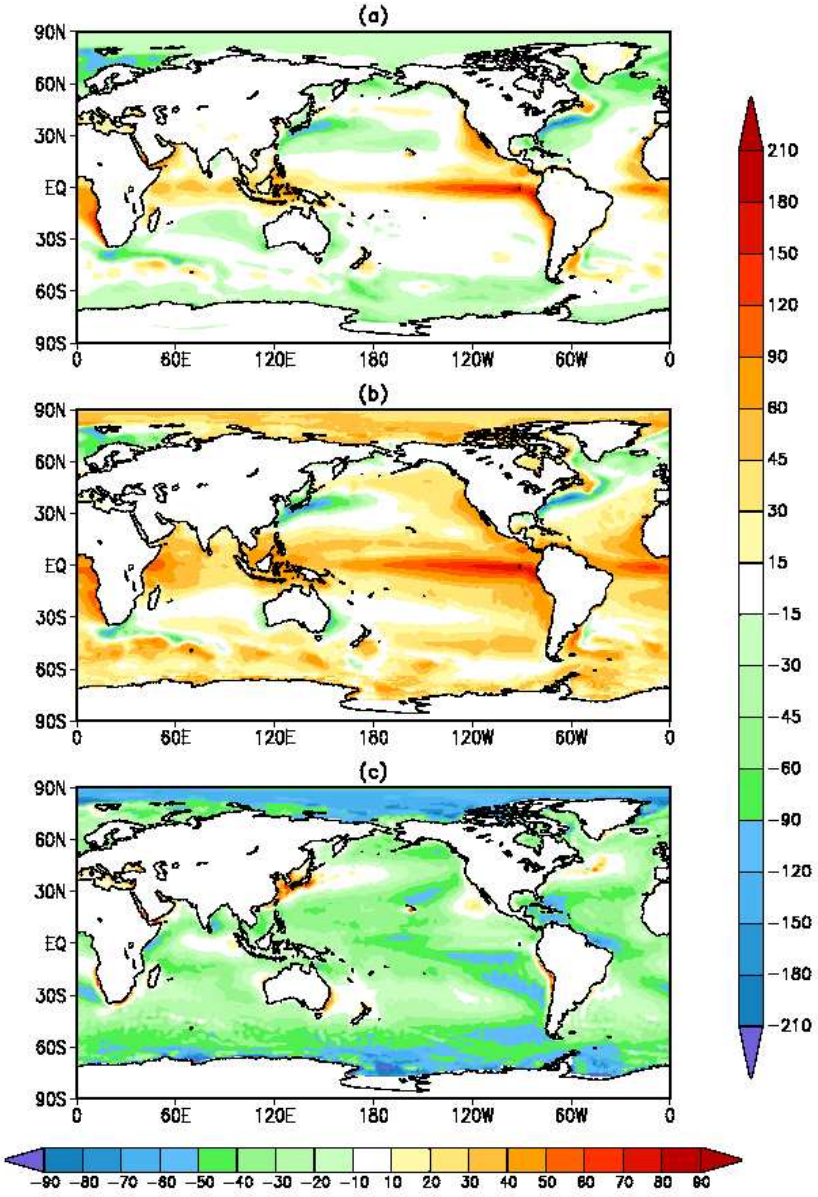

Figure 52: Annual mean (over oceans only) net surface heating in W m^{-2} from a) GEOS-5 AGCM b) WHOI and c) the difference, GEOS-5 - WHOI.

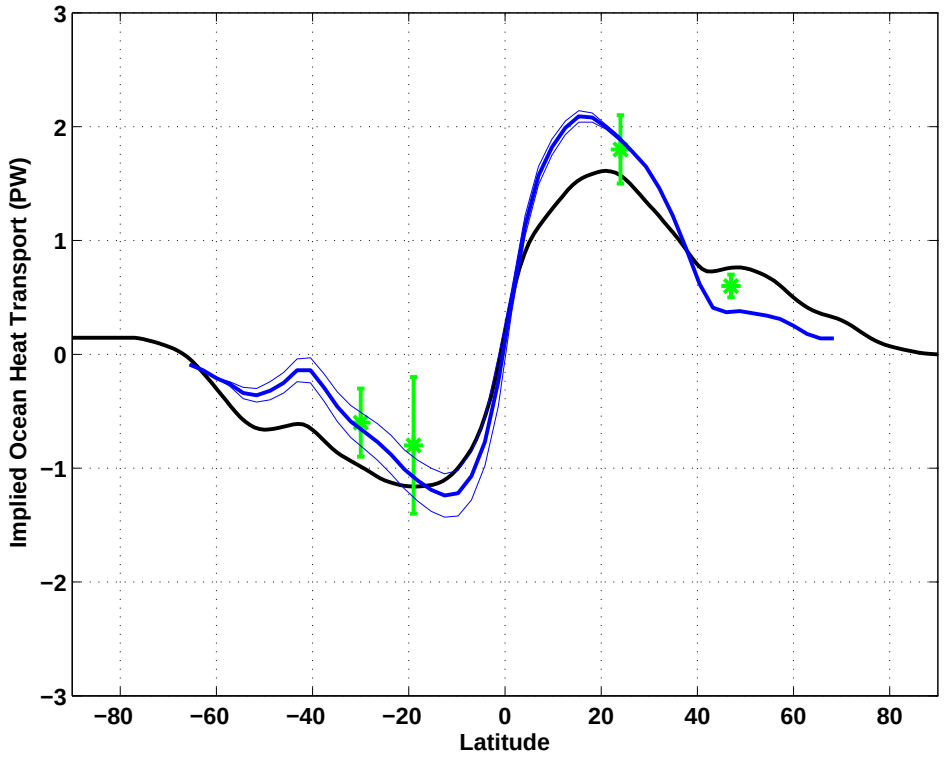

Figure 53: Implied Ocean Heat Transport in PW from GEOS-5 AGCM (black), from Ganachaud and Wunsch(2000) (green) and from Trenberth and Caron (2001) (blue).

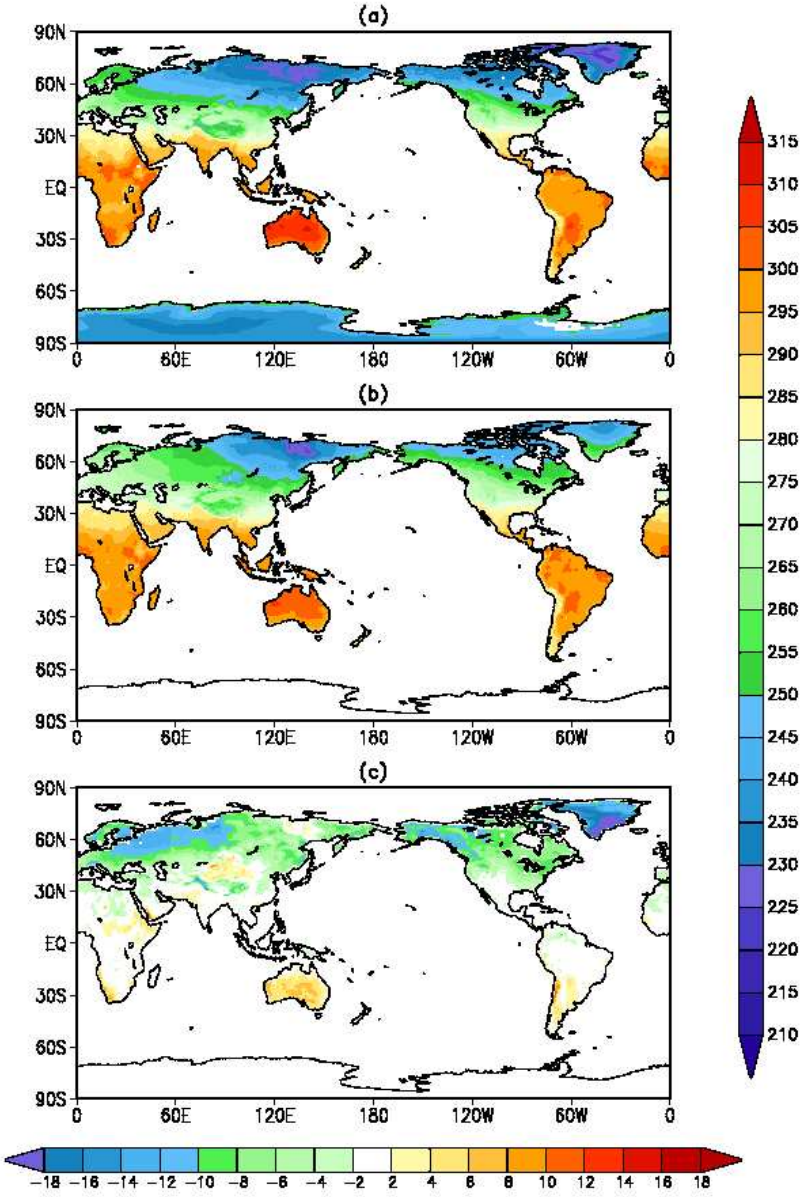

Figure 54: December-January-February Land Surface Temperature in K from a) GEOS-5 AGCM b) CRU TS and c) the difference, GEOS-5 - CRU TS.

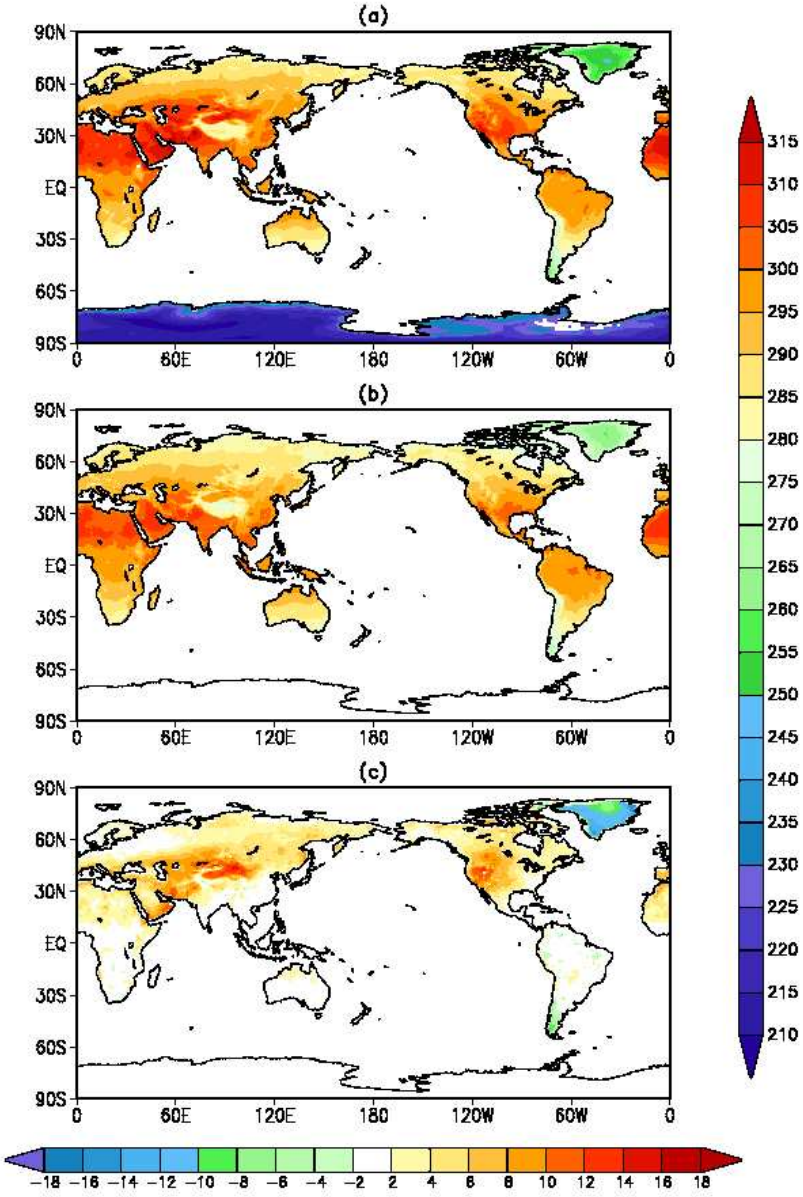

Figure 55: June-July-August Land Surface Temperature in K from a) GEOS-5 AGCM b) CRU TS and c) the difference, GEOS-5 - CRU TS.

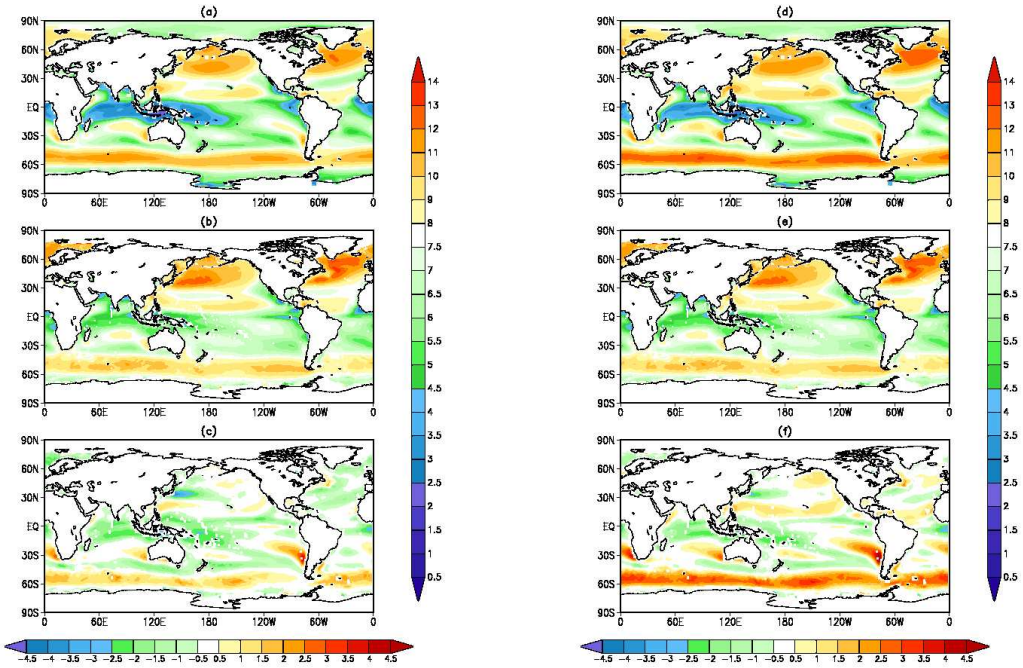

Figure 56: 30-year average December-January-February surface wind speed (m sec^{-1}) from: a) Fortuna control, b) GSSTF, c) Control-GSSTF, d) Experiment 1, e) GSSTF, f) Experiment 1-GSSTF

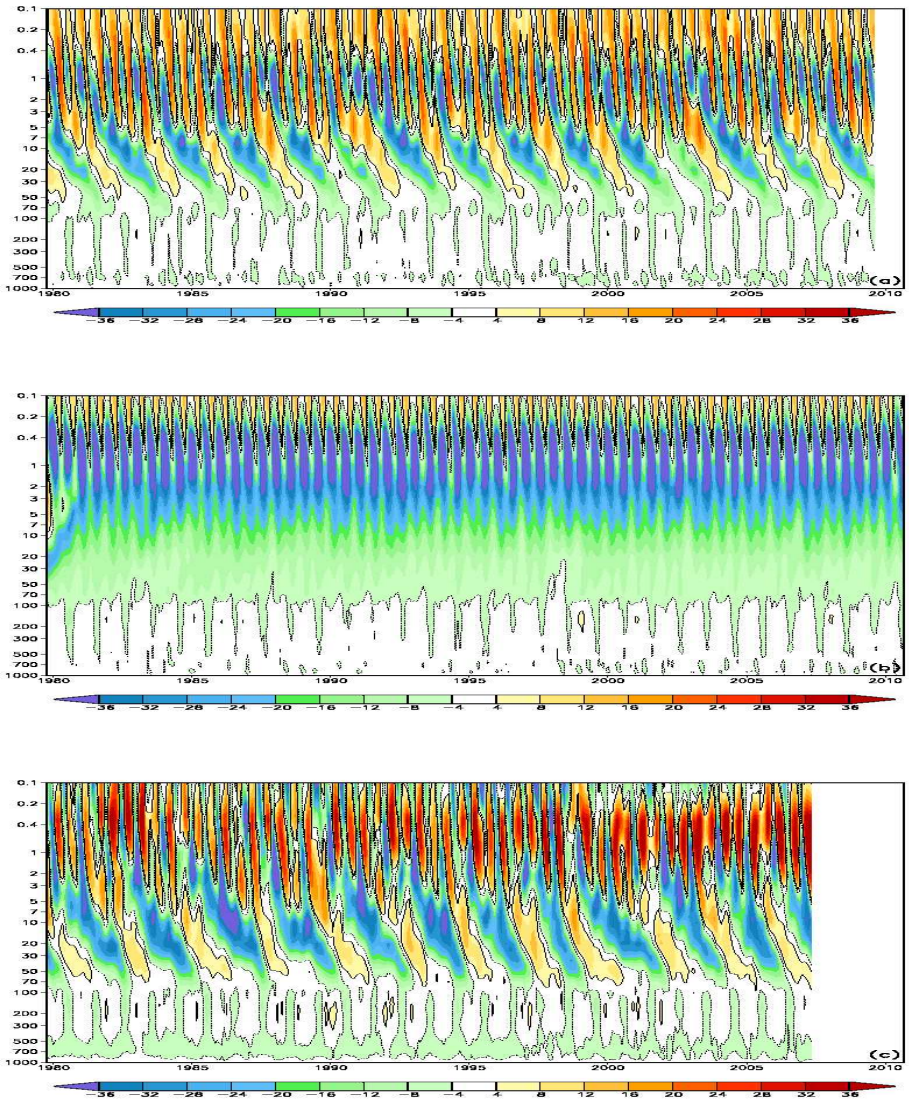

Figure 57: Spatial average of zonal wind in m s^{-1} from 10S to 10N latitude as a function of pressure level in mb and time from a) Fortuna control, b) Experiment 2 and c) MERRA reanalysis.

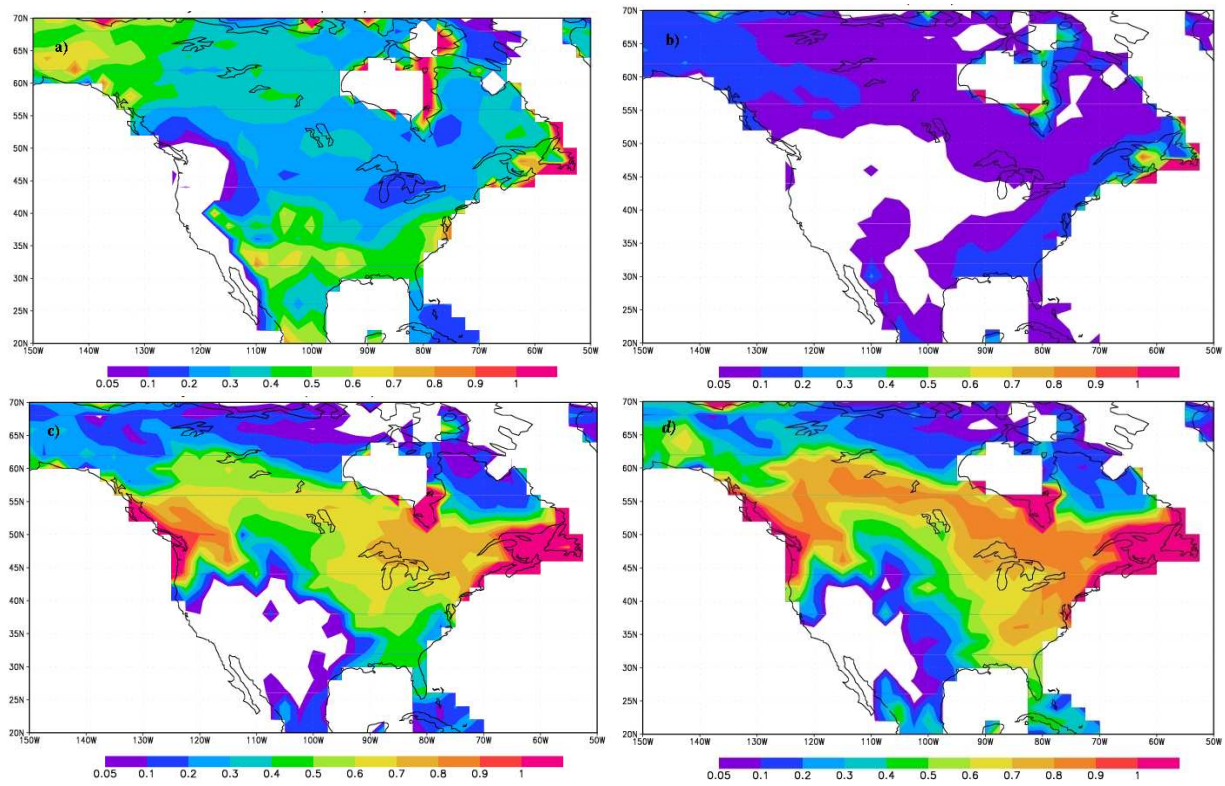

Figure 58: 30-year average June-July-August evaporation fractions. a) Fraction of evaporation from interception canopy in experiment 1 (Fortuna control), b) same as a) but from experiment 2, c) fraction of evaporation from transpiration in experiment 1, d) same as c) but from experiment 2.

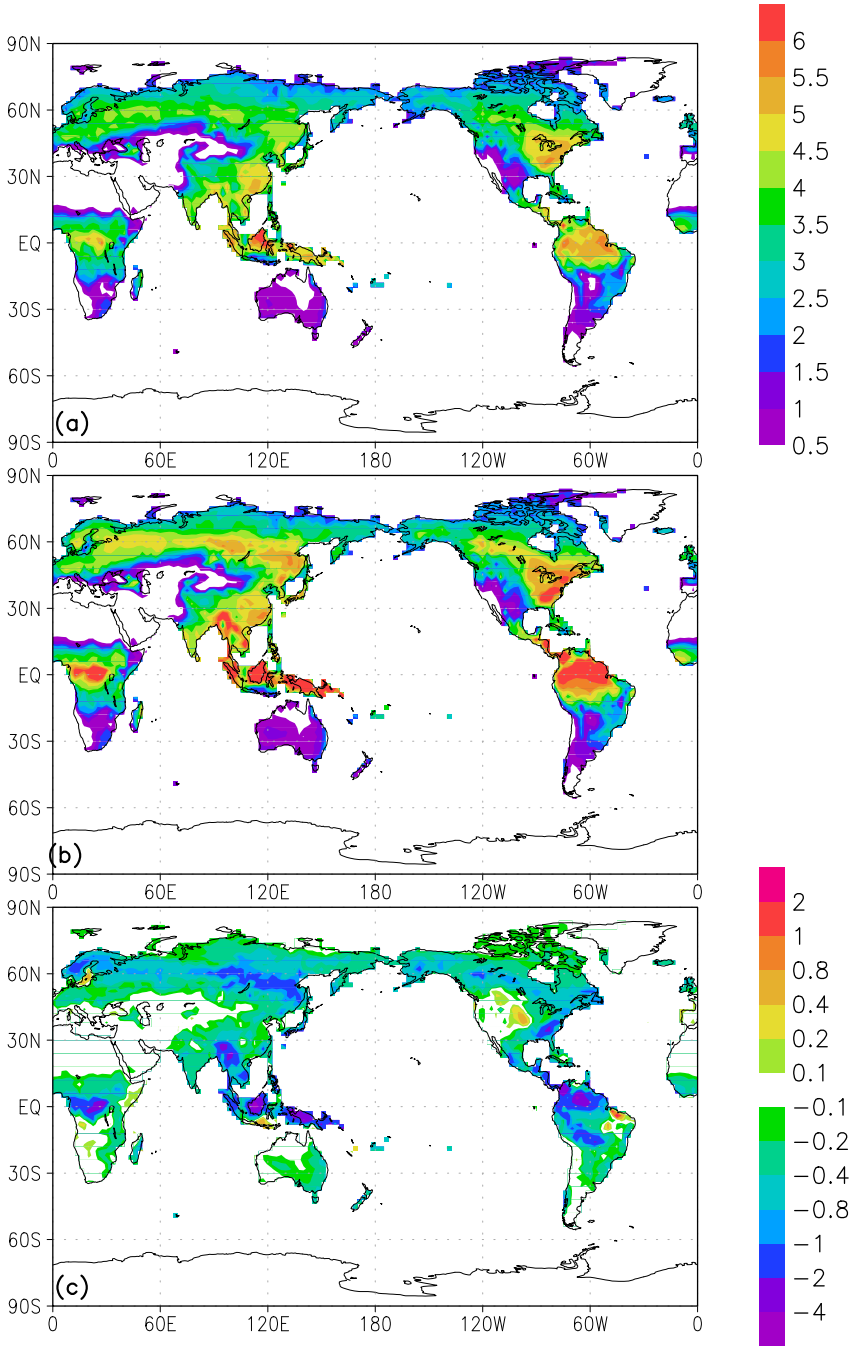

Figure 59: June-July-August averaged evaporation in mm day^{-1} over land surfaces from a) Experiment 1 (Fortuna), b) experiment 2 (MERRA AGCM) and c) the difference, experiment 1 minus experiment 2.

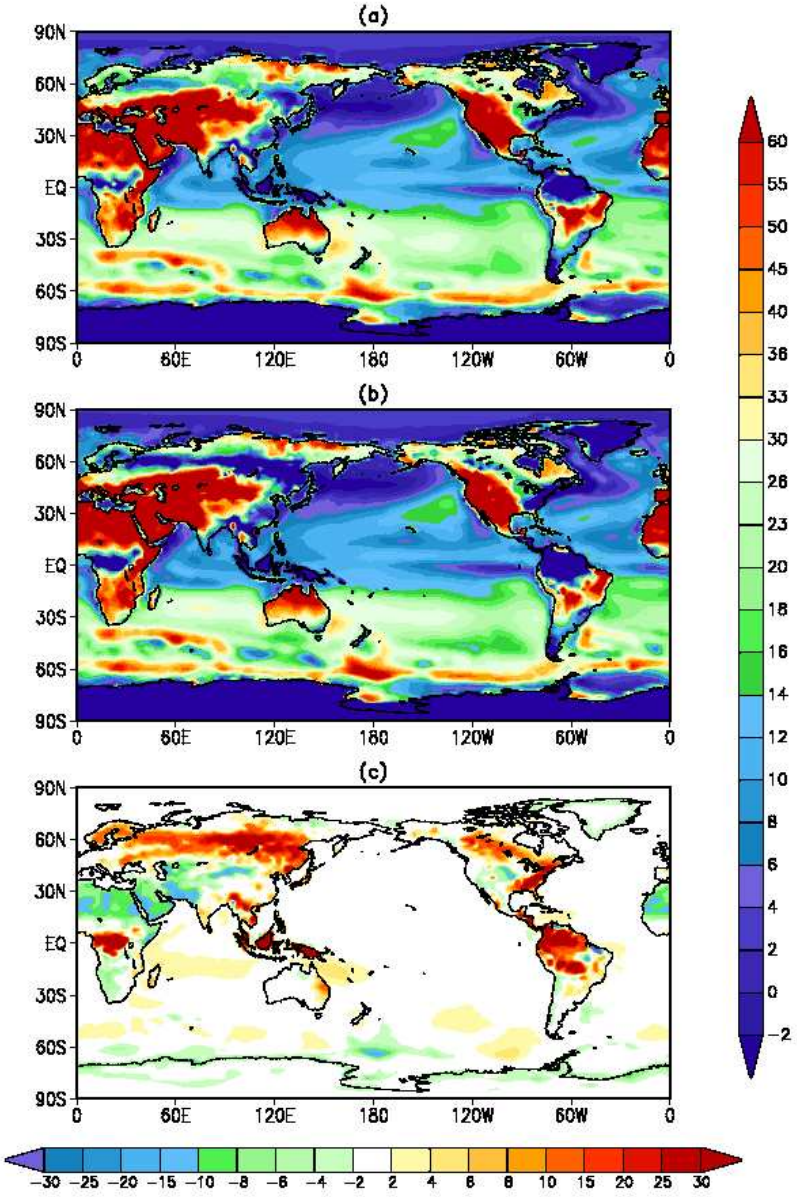

Figure 60: June-July-August averaged sensible heat flux in W m^{-2} from a) Experiment 3 (Louis scheme), b) experiment 2 (Helfand scheme) and c) the difference, experiment 3 minus experiment 2.

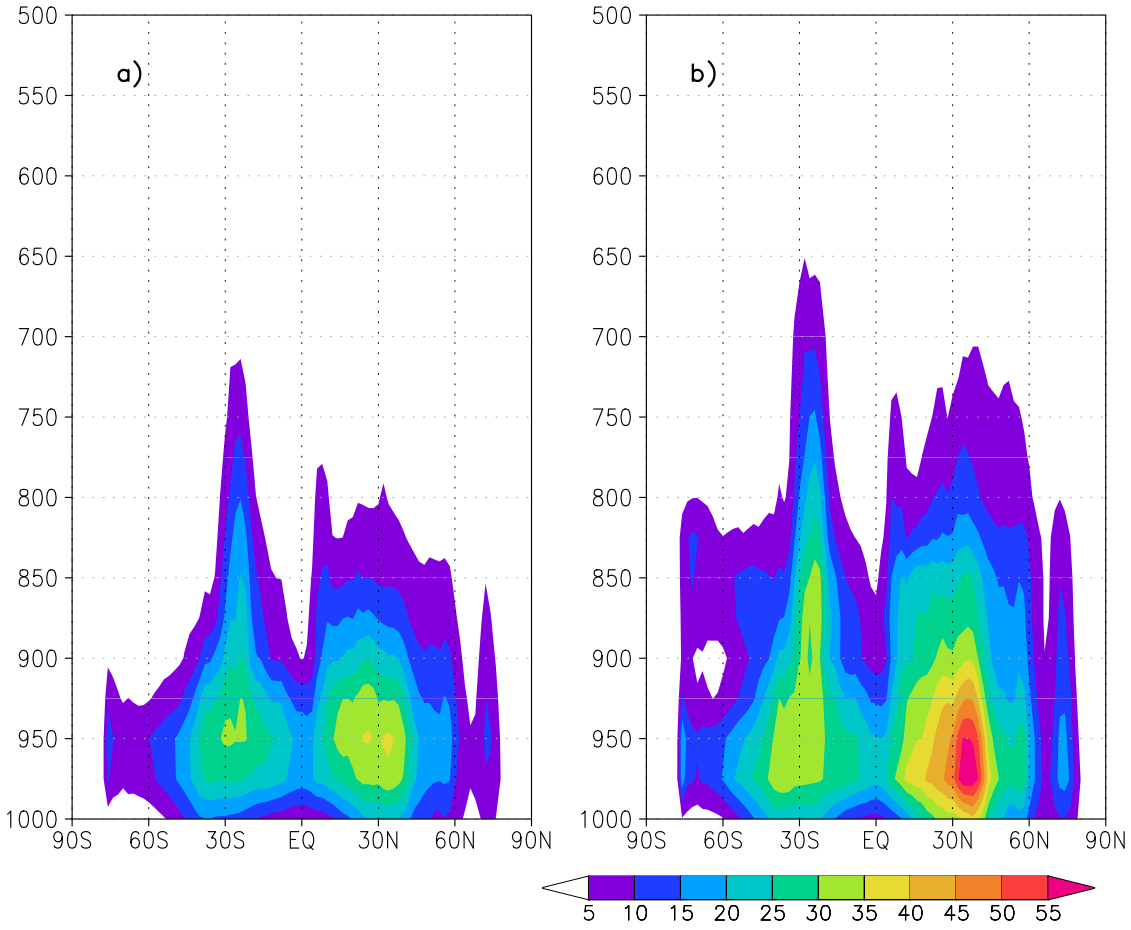

Figure 61: 30-year average June-July-August turbulent exchange coefficient for heat in m sec^{-2} from a) experiment 3 (Fortuna control), and b) from experiment 4.

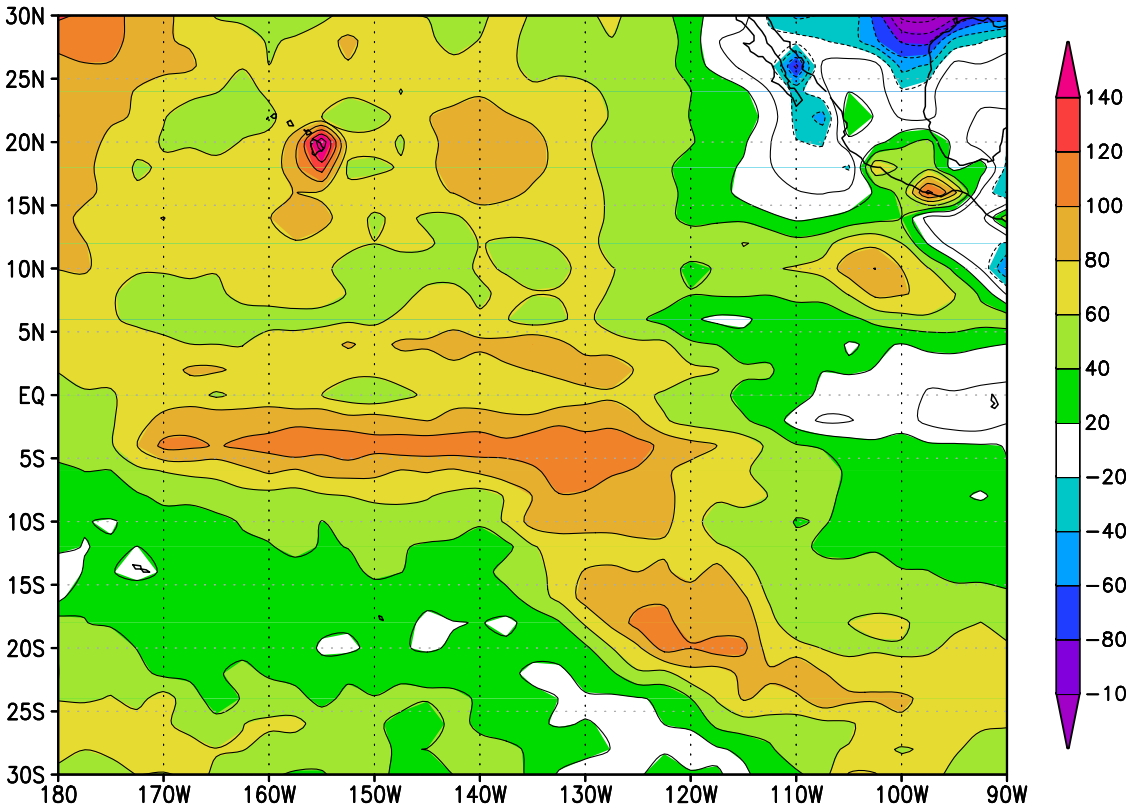

Figure 62: December-January-February averaged planetary boundary layer height difference in m, experiment 3 minus experiment 4.

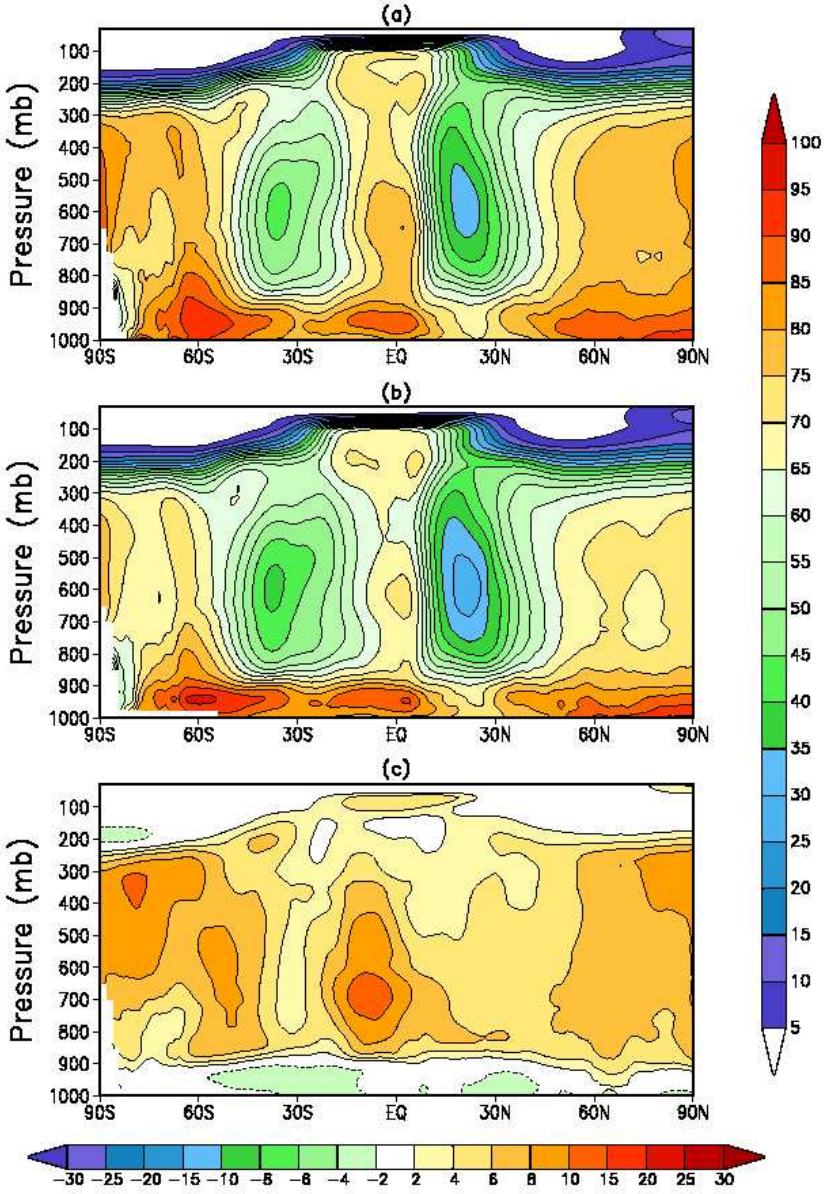

Figure 63: December-January-February averaged relative humidity in percent from a) Experiment 5 (MERRA AGCM), b) experiment 4 (Fortuna) and c) the difference, experiment 5 minus experiment 4.

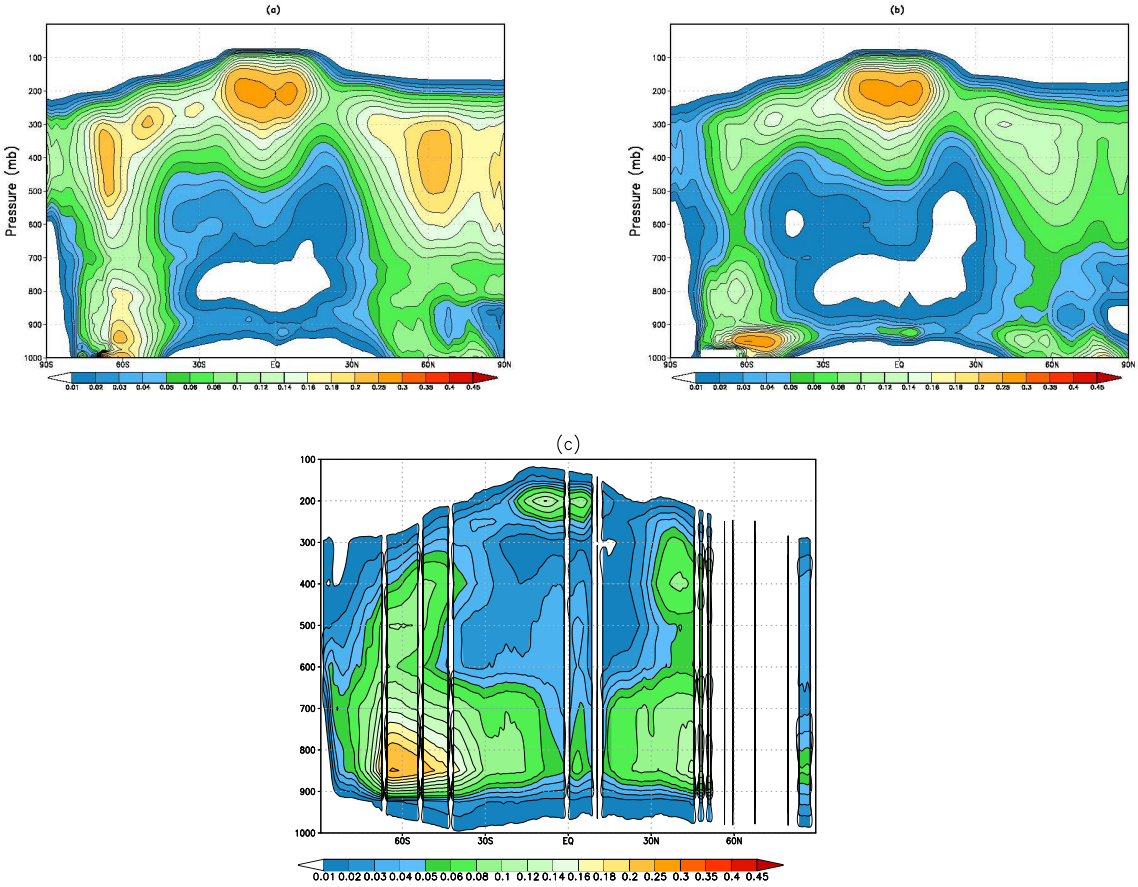

Figure 64: December-January-February averaged cloud fraction from a) Experiment 5 (MERRA AGCM), b) experiment 4 (Fortuna) and c) AIRS retreivals

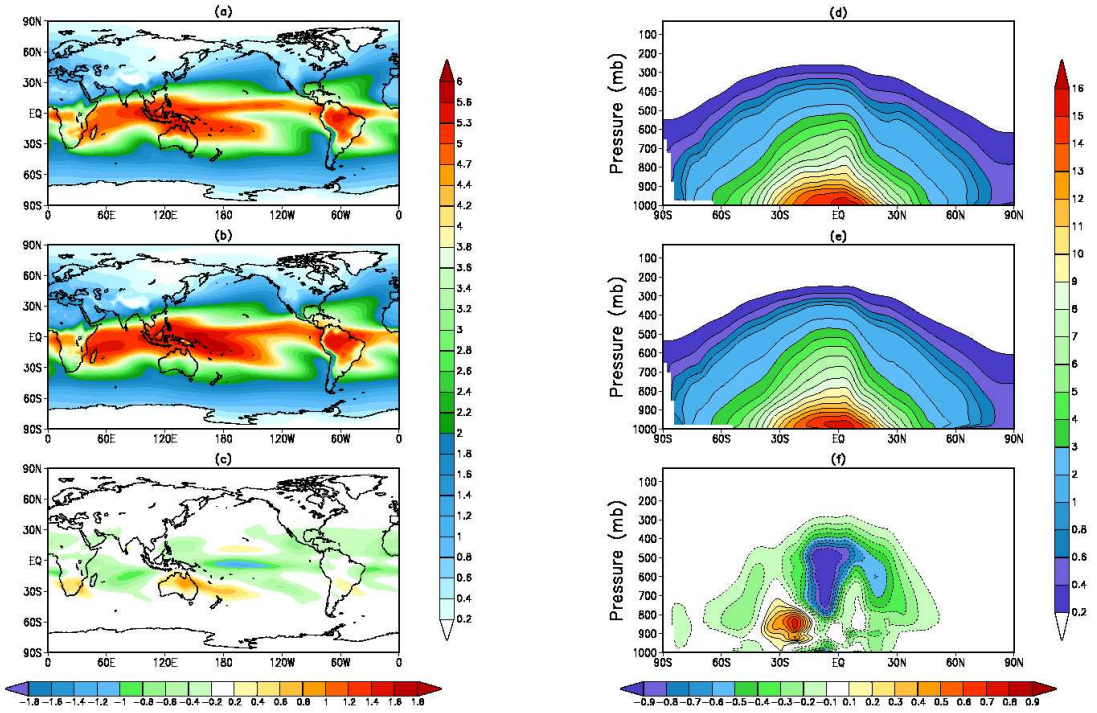

Figure 65: a) December-January-February total precipitable water in mm from experiment 6 (MERRA AGCM), b) same as a) but from experiment 5, c) same as a) but the difference, experiment 6 minus experiment 5, d) December-January-February specific humidity in g kg^{-1} from experiment 6 (MERRA AGCM), e) same as d) but from experiment 5, f) same as d) but the difference, experiment 6 minus experiment 5.

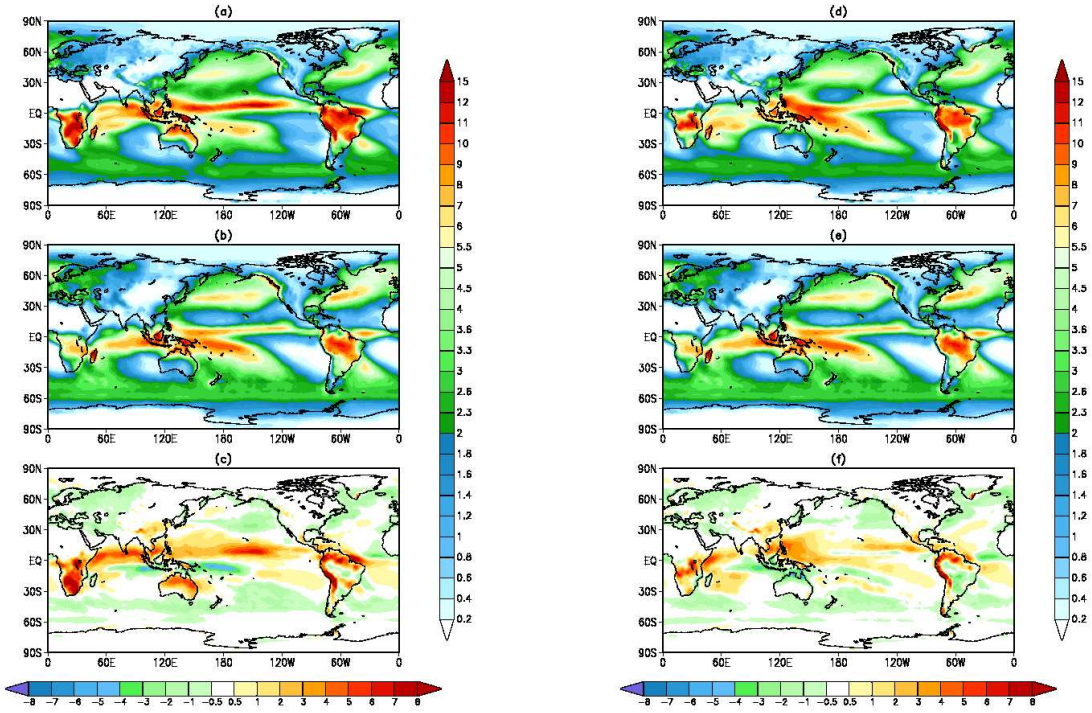

Figure 66: December-January-February total precipitation in mm day^{-1} from a) experiment 6 (MERRA AGCM), b) GPCP, c) the difference, experiment 6 minus GPCP, d) experiment 5 (Fortuna), e) GPCP, and f) the difference, experiment 5 minus GPCP.

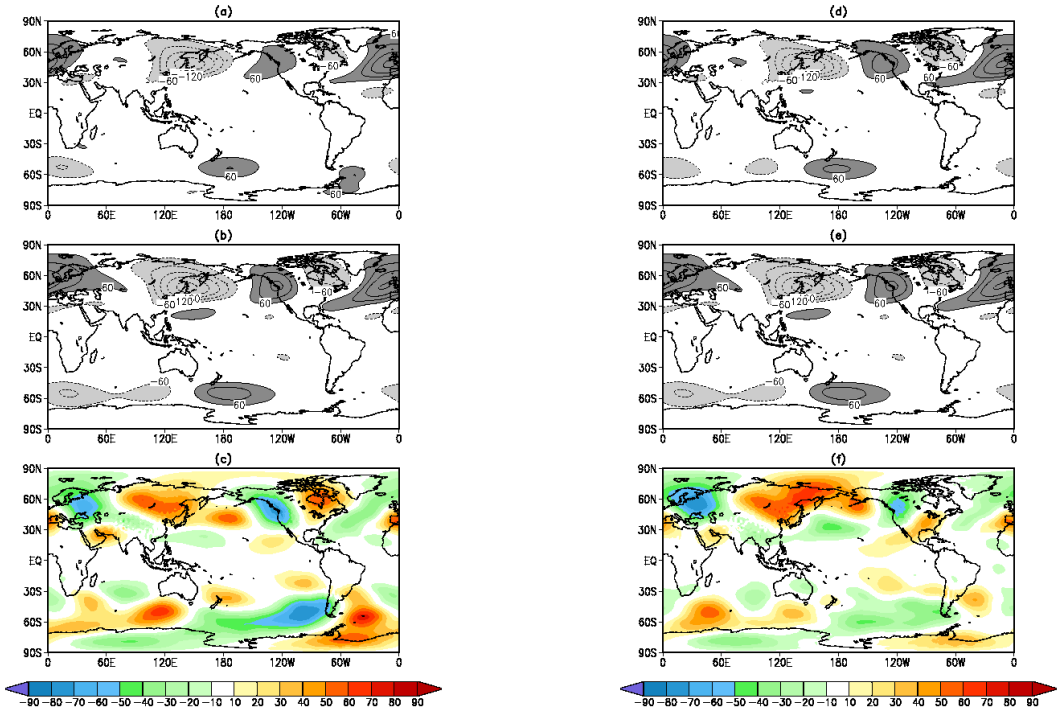

Figure 67: December-January-February 300 mb Eddy Height Climatology in m from a) experiment 6 (MERRA AGCM), b) MERRA, c) the difference, experiment 6 minus MERRA, d) experiment 5 (Fortuna), e) MERRA, and f) the difference, experiment 5 minus MERRA.

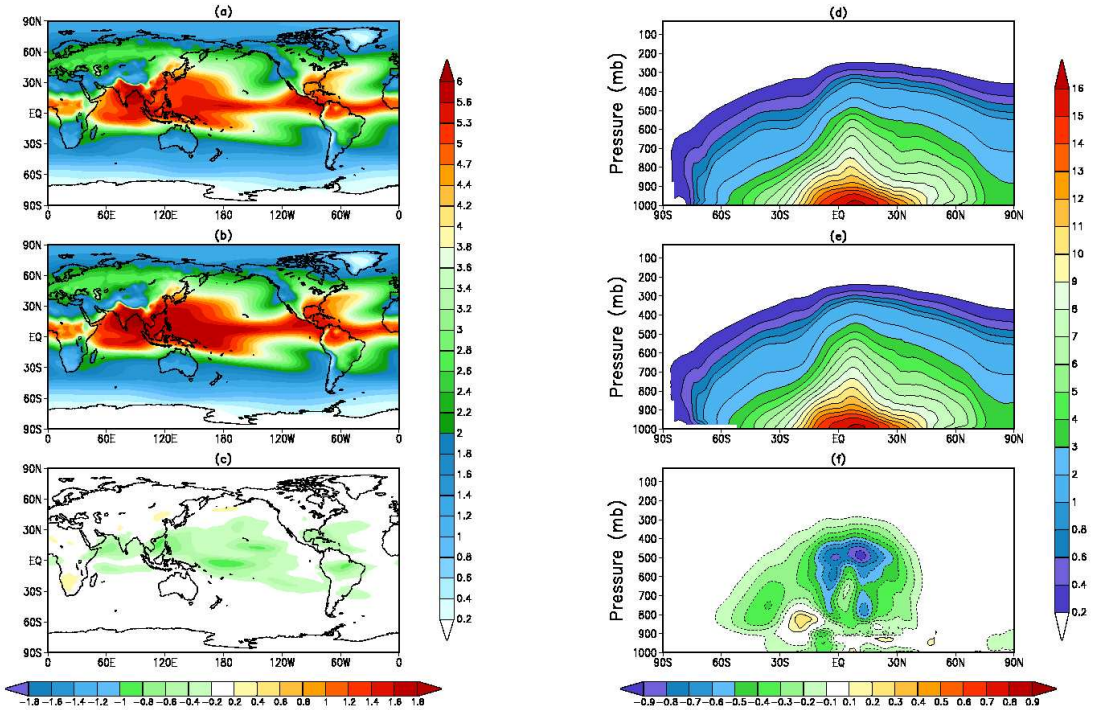

Figure 68: a) June-July-August total precipitable water in mm from experiment 6 (MERRA AGCM), b) same as a) but from experiment 5, c) same as a) but the difference, experiment 6 minus experiment 5, d) June-July-August specific humidity in g kg^{-1} from experiment 6 (MERRA AGCM), e) same as d) but from experiment 5, f) same as d) but the difference, experiment 6 minus experiment 5.

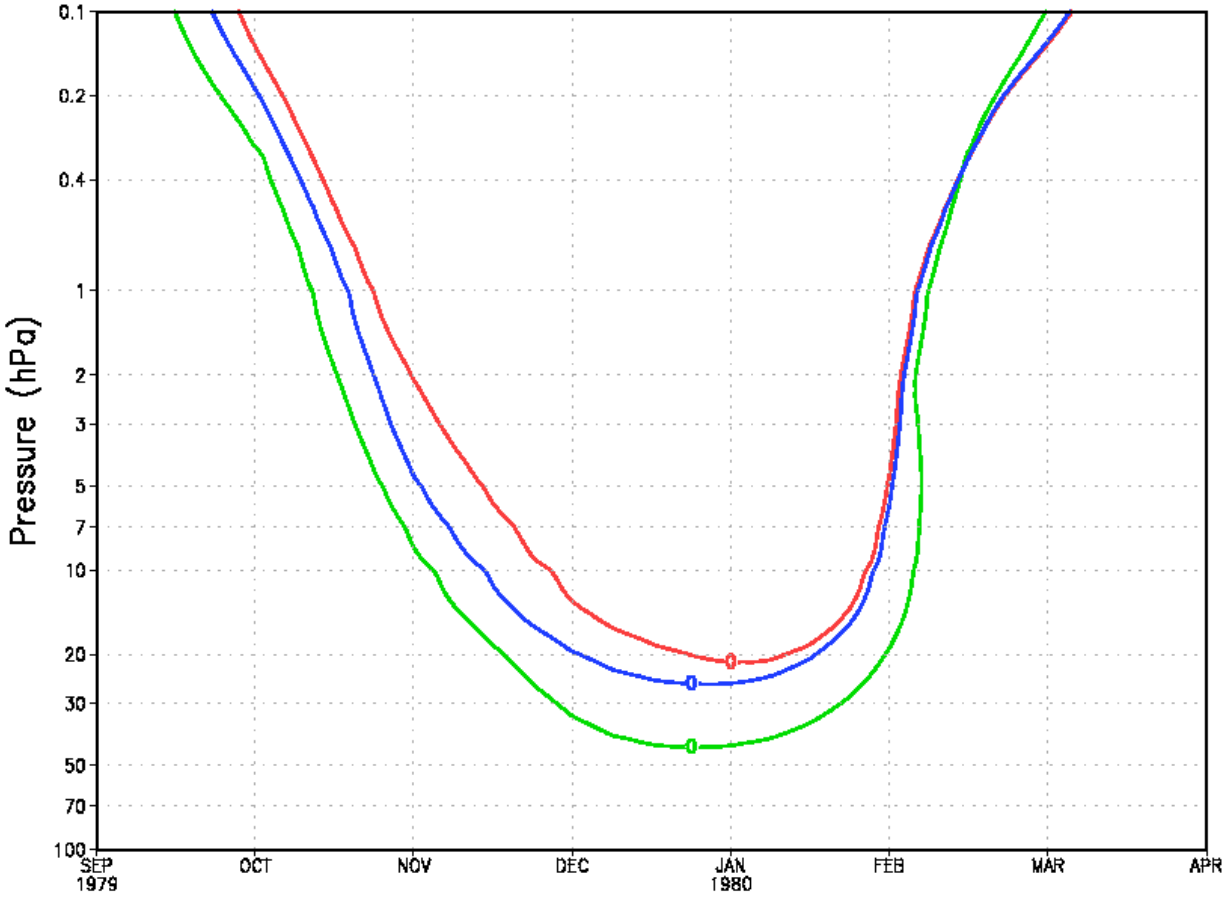

Figure 69: 30-year averaged annual cycle of zonal mean zonal wind, averaged from 70S to 50S latitude in m sec^{-2} from Experiment 7 in red (MERRA AGCM), experiment 6 in blue (Fortuna) and MERRA in green

References

Alexander, M. J., and H. Teitelbaum, 2007: Observation and analysis of a large amplitude mountain wave event over the Antarctic peninsula. *J. Geophys. Res.*, **112**, D21103, doi:10.1029/2006JD008368.

Alexander, M. J., S. D. Eckermann, D. Broutmann, and J. Ma, 2009: Momentum flux estimates for South Georgia Island mountain waves in the stratosphere observed via satellite. *Geophys. Res. Lett.*, **36**, L12816, doi:10.1029/2009GL038587.

Bacmeister, J. T., M. J. Suarez, and F. R. Robertson, 2006: Rain reevaporation, boundary layerconvection interactions, and Pacific rainfall patterns in a AGCM. *J.Atmos. Sci.*, **63**, 33833403.

Blackadar, A.K., 1962: The vertical distribution of wind and turbulent exchange in neutral atmosphere. *J. Geophys. Res.*, **67**, 3095-3102.

Charlock, T. P. and V. Ramanathan, 1985: The Albedo Field and Cloud Radiative Forcing Produced by a General Circulation Model with Internally Generated Optics. *J. Atmos. Sci.*, **42**, 1408-1429.

Chou, M.-D., 1992: A solar radiation model for use in climate studies. *J. Atmos. Sci.*, **49**, 762-772.

Chou, M.-D., 1990: Parameterizations for the absorption of solar radiation by O_2 and CO_2 with applications to climate studies. *J. Climate*, **3**, 209-217.

Chou, M. -D., and M.J.Suarez, 1994: An efficient thermal infrared radiation parameterization for use in general circulation models, NASA Tech. Memorandum 104606-Vol 3, NASA, Goddard Space Flight Center, Greenbelt, MD.

da Silva, A. M., C. C. Young and S. Levitus, 1995: Atlas of Marine Surface Data 1994, Volume 1: Algorithms and Procedures. NOAA Atlas NESDIS 7, *in press.*

Dee, DP, and co-authors, 2011: The ERA-Interim reanalysis: configuration and performance of the data assimilation system. *Q. J. R. Meteorol. Soc.* **137**, 553597.

Defries, R. S., and J. R. G. Townshend, 1994: NDVI-derived Land Cover Classification at Global Scales. *Int'l J. Rem. Sens.* **15**, 3567-3586. Special Issue on Global Data Sets.

Dorman, C. E., and R. H. Bourke, 1978: A Temperature Correction for Tucker's Ocean Rainfall Estimates. *Q. Journ. Roy. Meteor. Soc.*, **104**, 765-773.

Ganachaud, A., and C. Wunsch, 2000: Improved estimates of global ocean circulation, heat transport and mixing from hydrological data. *Nature* **408** 453457.

Helfand, H. M., M. and S. D. Schubert, 1995: Climatology of the Simulated Great Plains Low-Level Jet and Its contribution to the Continental Moisture Budget of the United States. *J. Climate*, **8**, 784-806.

Huffman, G., Adler, R.F., Rudolf, B., Schneider, U. and Keehn, P.R. 1995. Global precipitation

estimates based on a technique for combining satellite-based estimates, rain gauge analysis, and NWP model precipitation information. *J. Climate*, **8**, 1284-1295.

Garcia, R. R., and B. A. Boville, 1994: Downward control of the mean meridional circulation and temperature distribution of the polar winter stratosphere. J. Atmos. Sci., **51**, 22382245.

Garfinkel, C.I., A. Molod, L. D. Oman and I.-S. Song, 2011: Improvement of the GEOS-5 AGCM upon Updating the Air-Sea Roughness Parameterization. *Geophys. Res. Lett.*, **38**, L18702, doi:10.1029/2011GL048802.

Kondo, J., 1975: Air-sea bulk transfer coefficients in diabatic conditions. *Boundary Layer Meteor.*, **9**, 91-112.

Koster, R. D., M. J. Suarez, A. Ducharne, M. Stieglitz, and P. Kumar, 2000: A catchment-based approach to modeling land surface processes in a GCM, Part 1, Model structure. *J. Geophys. Res.*, **105**, 24 80924 822.

Large, W. G., and S. Pond, 1982: Sensible and Latent Heat Flux Measurements Over the Ocean. *J. Phys. Oceanogr.*, **12**, 464-482.

Large, W. G., and S. Pond, 1981: Open ocean momentum flux measurements in moderate to strong winds. *J. Phys. Oceanogr.*, **11**, 324-336.

Lindzen, R. S., 1981: Turbulence and stress owing to gravity wave and tidal breakdown. *J. Geophys. Res.*, **86**, 9707–9714.

Lock, A. P., A. R. Brown, M. R. Bush, G. M. Martin, and R. N. B. Smith, 2000: A new boundary layer mixing scheme. Part I: Scheme description and single-column model tests. *Mon. Wea. Rev.*, **138**, 31873199.

Louis, J. E, 1979: A Parametric Model of Vertical Eddy Fluxes in the Atmosphere, *Bound. Lay. Meteorol.*, **17**, 187-202

Louis, J. and J. Geleyn, 1982: A short history of the PBL parameterization at ECMWF. Proc. ECMWF Workshop on Planetary Boundary Layer Parameterization, Reading, United Kingdom, ECMWF, 5980.

McFarlane, N. A., 1987: The effect of orographically excited gravity-wave drag on the circulation of the lower stratosphere and troposphere. *J. Atmos. Sci.*, **44**, 1775–1800.

Mitchell, T. D., and Jones, P. D. 2005: An Improved Method of Constructing a Database of Monthly Climate Observations and Associated High-Resolution Grids. *Intl. J. Climatology*, **25**, 693–712.

Molod, A, 2012: Constraints on the Total Water PDF in GCMs from AIRS and a High Resolution Model. J. Climate, Sub Judice

Molod, A., M. Suarez and G. Partyka, 2012: The Impact on GEOS-5 Tropical Cyclone Simulations of Limiting Ocean Roughness. *In Preparation*

Moorthi, S., and M. J. Suarez, 1992: Relaxed Arakawa Schubert: A parameterization of moist

convection for general circulation models. *Mon. Wea. Rev.*, **120**, 978-1002.

Neale, R. and co-authors. Description of the NCAR Community Atmosphere Model (CAM 5.0). NCAR TECHNICAL NOTE, 2010. URL http://www.cesm.ucar.edu/models/cesm1.0/cam/docs/description/cam5_desc.pdf.

Pinker, R. T. and I. Laszlo, 1992: Modelling Surface Solar Irradiance for Satellite Applications on a Global Scale. *Journ. App. Meteor.*, **31**, 331-347.

Rienecker, M. M., and Coauthors, 2008: The GEOS-5 Data Assimilation SystemDocumentation of versions 5.0.1 and 5.1.0, and 5.2.0. NASA Tech. Rep. Series on Global Modeling and Data Assimilation, NASA/TM-2008-104606, Vol. 27, 92 pp.

Rienecker, M.M., and co-authors, 2011: MERRA: NASAs Modern-Era Retrospective Analysis for Research and Applications. *J. Climate*, **24**, 3624-3648.

Reynolds, R. W., N. A. Rayner, T. M. Smith, D. C. Stokes, and W. Wang, 2002: An improved in situ and satellite SST analysis for climate. em J. Climate, **15**, 16091625.

Richter, J. H., F. Sassi, and R. R. Garcia, 2010: Toward a physically based gravity wave source parameterization in a general circulation model. *J. Atmos. Sci.*, **67**, 136–156.

Shie, C.-L., L. S. Chiu, R. Adler, E. Nelkin, I-I. Lin, P. Xie, F.-C. Wang, R. Chokngamwong, W. Olson, and D. A. Chu, 2009: A Note on reviving the Goddard satellite-based surface turbulent fluxes (GSSTF) dataset. *Adv. Atmos. Sci.*, **26(6)**, 1071–1080.

Solomon, S.; D. Qin, M. Manning, Z. Chen, M. Marquis, K.B. Averyt, M. Tignor and H.L. Miller, ed., 2007: Climate Change 2007: The Physical Science Basis, Contribution of Working Group I to the Fourth Assessment Report of the Intergovernmental Panel on Climate Change, Cambridge University Press, ISBN 978-0-521-88009-1 (pb: 978-0-521-70596-7).

Stieglitz, M., A. Ducharne, R. D. Koster, M. J. Suarez, 2001: The Impact of Detailed Snow Physics on the Simulation of Snowcover and Subsurface Thermodynamics at Continental Scales. *J. Hydromet.*, **2**, 228-242

Trenberth, K.E. and J. Caron, 2001: Estimates of Meridional Atmosphere and Ocean Heat Transports. *J. Climate*, **14**, 3433-3443.

Tucker, G. G., 1961: Precipitation Over the North Atlantic Ocean. *Q. Journ. Roy. Meteor. Soc.*, **87**, 147-158.

Wielicki, B. A., B. R. Barkstrom, E. F. Harrison, R. B. Lee III, G. L. Smith, and J. E. Cooper, 1996: Clouds and the Earth's Radiant Energy System (CERES): An Earth Observing System Experiment. *Bull. Amer. Meteor. Soc.*, **77**, 853–868.

Yu, L., Jin, X., and Weller, R., 2008: Multidecade Global Flux Datasets from the Objectively Analyzed Air-sea Fluxes (OAFlux) Project: Latent and Sensible Heat Fluxes, Ocean Evaporation, and Related Surface Meteorological Variables, OAFlux Project Technical Report (OA-2008-01), Woods Hole Oceanographic Institution, Wood Hole, MA.

Previous Volumes in This Series

Volume 1 *September 1994*
Documentation of the Goddard Earth Observing System (GEOS) General Circulation Model–Version 1
L.L. Takacs, A. Molod, and T. Wang

Volume 2 *October 1994*
Direct Solution of the Implicit Formulation of Fourth Order Horizontal Diffusion for Gridpoint Models on the Sphere
Y. Li, S. Moorthi, and J.R. Bates

Volume 3 *December 1994*
An Efficient Thermal Infrared Radiation Parameterization for use in General Circulation Models
M.-D. Chou and M.J. Suarez

Volume 4 *January 1995*
Documentation of the Goddard Earth Observing System (GEOS) Data Assimilation System–Version 1
James Pfaendtner, Stephen Bloom, David Lamich, Michael Seablom, Meta Sienkiewicz, James Stobie, and Arlindo da Silva

Volume 5 *April 1995*
Documentation of the Aries-GEOS dynamical core: Version 2
Max J. Suarez and Lawrence L. Takacs

Volume 6 *April 1995*
A Multiyear Assimilation with the GEOS-1 System: Overview and Results
Siegfried Schubert, Chung-Kyu Park, Chung-Yu Wu, Wayne Higgins, Yelena Kondratyeva, Andrea Molod, Lawrence Takacs, Michael Seablom, and Richard Rood

Volume 7 *September 1995*
Proceedings of the Workshop on the GEOS-1 Five-Year Assimilation
Siegfried D. Schubert and Richard B. Rood

Volume 8 *March 1996*
Documentation of the Tangent Linear Model and Its Adjoint of the Adiabatic Version of the NASA GEOS-1 C-Grid GCM: Version 5.2
Weiyu Yang and I. Michael Navon

Volume 9 *March 1996*
Energy and Water Balance Calculations in the Mosaic LSM
Randal D. Koster and Max J. Suarez

Volume 10 *April 1996*
Dynamical Aspects of Climate Simulations Using the GEOS General Circulation Model
Lawrence L. Takacs and Max J. Suarez

Volume 11 *May 1997*
Documentation of the Tangent Linear and its Adjoint Models of the Relaxed Arakawa-Schubert Moisture Parameterization Package of the NASA GEOS-1 GCM (Version 5.2)
Weiyu Yang, I. Michael Navon, and Ricardo Todling

Volume 12 *August 1997*
Comparison of Satellite Global Rainfall Algorithms
Alfred T.C. Chang and Long S. Chiu

Volume 13 *December 1997*
Interannual Variability and Potential Predictability in Reanalysis Products
Wie Ming and Siegfried D. Schubert

Volume 14 *August 1998*
A Comparison of GEOS Assimilated Data with FIFE Observations
Michael G. Bosilovich and Siegfried D. Schubert

Volume 15 *June 1999*
A Solar Radiation Parameterization for Atmospheric Studies
Ming-Dah Chou and Max J. Suarez

Volume 16 *November 1999*
Filtering Techniques on a Stretched Grid General Circulation Model
Lawrence Takacs, William Sawyer, Max J. Suarez, and Michael S. Fox-Rabinowitz

Volume 17 *July 2000*
Atlas of Seasonal Means Simulated by the NSIPP-1 Atmospheric GCM
Julio T. Bacmeister, Philip J. Pegion, Siegfried D. Schubert, and Max J. Suarez

Volume 18 *December 2000*
An Assessment of the Predictability of Northern Winter Seasonal Means with the NSIPP 1 AGCM
Philip J. Pegion, Siegfried D. Schubert, and Max J. Suarez

Volume 19 *July 2001*
A Thermal Infrared Radiation Parameterization for Atmospheric Studies
Ming-Dah Chou, Max J. Suarez, Xin-Zhong, and Michael M.-H. Yan

Volume 20 *August 2001*
The Climate of the FVCCM-3 Model
Yehui Chang, Siegfried D. Schubert, Shian-Jiann Lin, Sharon Nebuda, and Bo-Wen Shen

Volume 21 *September 2001*
Design and Implementation of a Parallel Multivariate Ensemble Kalman Filter for the Poseidon Ocean General Circulation Model
Christian L. Keppenne and Michele M. Rienecker

Volume 22 *August 2002*
Coupled Ocean-Atmosphere Radiative Model for Global Ocean Biogeochemical Models
Watson W. Gregg

Volume 23 *November 2002*
Prospects for Improved Forecasts of Weather and Short-term Climate Variability on Subseasonal (2-Week to 2-Month) Time Scales
Siegfried D. Schubert, Randall Dole, Huang van den Dool, Max J. Suarez, and Duane Waliser

Volume 24 *July 2003*
Temperature Data Assimilation with Salinity Corrections: Validation for the NSIPP Ocean Data Assimilation System in the Tropical Pacific Ocean, 1993–1998
Alberto Troccoli, Michele M. Rienecker, and Christian L. Keppenne,

Volume 25 *December 2003*
Modeling, Simulation, and Forecasting of Subseasonal Variability
Duane Waliser, Siegfried D. Schubert, Arun Kumar, Klaus Weickmann, and Randall Dole

Volume 26 *April 2005*
Documentation and Validation of the Goddard Earth Observing System (GEOS) Data Assimilation System – Version 4
Senior Authors: S. Bloom, A. da Silva and D. Dee
Contributing Authors: M. Bosilovich, J-D. Chern, S. Pawson, S. Schubert, M. Sienkiewicz, I. Stajner, W-W. Tan, and M-L. Wu and Gregory C. Johnson

Volume 27 *December 2008*
The GEOS-5 Data Assimilation System—Documentation of Versions 5.0.1, 5.1.0, and 5.2.0
Editor: M.J. Suarez
Contributing Authors: M.M. Rienecker, M.J. Suarez, R. Todling, J. Bacmeister, L. Takacs, H.-C. Liu, W. Gu, M. Sienkiewicz, R.D. Koster, R. Gelaro, I. Stajner, and J.E. Nielsen

REPORT DOCUMENTATION PAGE

Form Approved
OMB No. 0704-0188

1. REPORT DATE *(DD-MM-YYYY)*	2. REPORT TYPE	3. DATES COVERED *(From - To)*
30-04-2012	Technical Memorandum	

4. TITLE AND SUBTITLE

Technical Report Series on Global Modeling and Data Assimilation, Volume 28, The GEOS-5 Atmospheric General Circulation Model: Mean Climate and Development from MERRA to Fortuna

5a. CONTRACT NUMBER

5b. GRANT NUMBER

5c. PROGRAM ELEMENT NUMBER

6. AUTHOR(S)

Max J. Suarez, Editor

Andrea Molod, Lawrence Takacs, Max Suarez, Julio Bacmeister, In-Sun Song, Andrew Eichmann

5d. PROJECT NUMBER

5e. TASK NUMBER

5f. WORK UNIT NUMBER

7. PERFORMING ORGANIZATION NAME(S) AND ADDRESS(ES)

NASA, Goddard Space Flight Center
Greenbelt, MD 20771

8. PERFORMING ORGANIZATION REPORT NUMBER

9. SPONSORING/MONITORING AGENCY NAME(S) AND ADDRESS(ES)

National Aeronautics and Space Administration
Washington, DC 20546-0001

10. SPONSORING/MONITOR'S ACRONYM(S)

NASA/GSFC

11. SPONSORING/MONITORING REPORT NUMBER

TM–2012-104606/Vol28

12. DISTRIBUTION/AVAILABILITY STATEMENT

Unclassified-Unlimited, Subject Category: 47
Report available from the NASA Center for Aerospace Information, 7115 Standard Drive, Hanover, MD 21076. (443)757-5802

13. SUPPLEMENTARY NOTES

14. ABSTRACT

This report is a documentation of the Fortuna version of the GEOS-5 Atmospheric General Circulation Model (AGCM). The GEOS-5 AGCM is currently in use in the NASA Goddard Modeling and Assimilation Office (GMAO) for simulations at a wide range of resolutions, in atmosphere only, coupled ocean-atmosphere, and data assimilation modes. The focus here is on the development subsequent to the version that was used as part of NASA's Modern-Era Retrospective Analysis for Research and Applications (MERRA). We present here the results of a series of 30-year atmosphere-only simulations at different resolutions, with focus on the behavior of the 1-degree resolution simulation. The details of the changes in parameterizations subsequent to the MERRA model version are outlined, and results of a series of 30-year, atmosphere-only climate simulations at 2-degree resolution are shown to demonstrate changes in simulated climate associated with specific changes in parameterizations. The GEOS-5 AGCM presented here is the model used for the GMAO's atmosphere-only and coupled CMIP-5 simulations.

15. SUBJECT TERMS

Meteorology, Climatology, Modeling

16. SECURITY CLASSIFICATION OF:			17. LIMITATION OF ABSTRACT	18. NUMBER OF PAGES	19b. NAME OF RESPONSIBLE PERSON
a. REPORT	b. ABSTRACT	c. THIS PAGE			Max Suarez
Unclassified	Unclassified	Unclassified	Unclassified	117	19b. TELEPHONE NUMBER *(Include area code)* (301) 614-5292